

THE UNIVERSITY OF CALGARY

Application of Radiative Hydrodynamics to the Problem of
Mass Loss from Red Giant Stars

by

Guojin Zhang

A THESIS

SUBMITTED TO THE FACULTY OF GRADUATE STUDIES
IN PARTIAL FULFILLMENT OF THE REQUIREMENTS FOR THE
DEGREE OF MASTER OF SCIENCE

DEPARTMENT OF PHYSICS AND ASTRONOMY

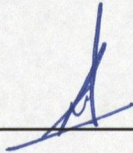
CALGARY, ALBERTA

APRIL, 1996

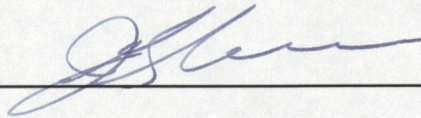
© Guojin Zhang 1996

THE UNIVERSITY OF CALGARY
FACULTY OF GRADUATE STUDIES

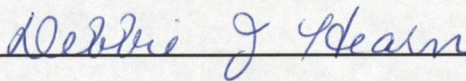
The undersigned certify that they have read, and recommend to the Faculty of Graduate Studies for acceptance, a thesis entitled "Application of Radiative Hydrodynamics to the Problem of Mass Loss from Red Giant Stars" submitted by Guojin Zhang in partial fulfillment of the requirements for the degree of Master of Science.



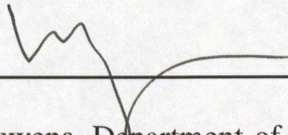
Supervisor, Dr. S. Kwok, Department of Physics and Astronomy



Dr. J. Gleeson, Department of Physics and Astronomy



Dr. D. Hearn, Department of Physics and Astronomy



Dr. L. Bauwens, Department of Mechanical Engineering

April 17, 86

Date

ABSTRACT

This thesis is concerned with stellar wind outflows of the Asymptotic Giant Branch (AGB) stars. The model that the radiation pressure acting on the dust grains drives the material outward is investigated in details. The hydrodynamics equations of motion for the outflow coupled with the equation of detailed radiative transfer are solved by treating the circumstellar envelope, which consists of gas and dust, as a two-component fluid. The results about the effects of parameters such as the mass loss rate, the dust grain size, and the dust to gas ratio are presented in this thesis as well as the lower limits on the mass loss rates. Our model shows that any changes on these parameters will change the terminal outflow velocities and the spectral energy distributions. Based on this model, the fitting of LRS spectra from IRAS for three stars: AFGL3068 (carbon-rich), α Ceti (oxygen-rich with $10\mu\text{m}$ emission feature) and OH25.6+0.6 (oxygen-rich with $10\mu\text{m}$ absorption feature) are obtained.

Acknowledgements

I would like to thank those who helped me over the past two and half years, without their guidance, many of the results described in this thesis would never have been obtained.

First and foremost I am indebted to my supervisor, Dr. Sun Kwok for his support which took many forms: introducing me to the topics of this thesis, giving me practical advice on how to proceed when problem occurred, giving constructive criticism and suggestion, providing a tremendous computing facility as well as providing the access to the infrared and IRAS databases, pushing me going further....., I also thank to him for his financial support that I received during part of the period in which the work was done.

I would also like to thank Dr. Rychard Szczerba who brought me the code which was used in the calculations of this thesis. Thanks also go to him for his helpful discussion, suggestion, and patient of keeping introducing the new things to me, which are including the code and super mongo plotting software.

Many deep Thanks also go to Dr. Kevin Volk who have helped me and given me useful suggestion and advice not only during the period of completing this thesis but also in whole past two and half years. Without his help a lot of things would not be done.

I am extremely fortunate to have Dr. Cheng-Yue Zhang who was always willingly and enthusiastically providing me constructive advice on my thesis and providing me support on the computing facility. Here a very special thanks goes to him.

Also, I have to thank Prof. Peishen Chen who gave me all kinds of advice on all kinds

of aspects when he visited here from China between Jan. and May in 1995. Although it was short time to be with him, the benefit goes forever for me.

I also want to thank Dr. J. Gleeson and Dr. D. Hearn who gave me good advice at the beginning of the work on this thesis.

Finally I would like to thank the Department of Physics and Astronomy for the opportunity to instruct undergraduate physics Labs. Not only did I find the teaching a most enjoyable experience, but also the financial support it provided was definitely appreciated.

Table of Contents

Title Page	i
Approval Page	ii
Abstract	iii
Acknowledgements	iv
Table of Contents	vi
List of Tables	ix
List of Figures	x
List of Symbols, Abbreviations, Nomenclatures	xiii
Chapter 1 - Introduction	1
1.1 - Evolution of Asymptotic Giant Branch Stars	1
1.2 - The Mechanism for Driving Materials Outward	8
1.3 - Application of Hydrodynamics and Radiative Transfer	10
Chapter 2 - The Model	15
2.1 - Hydrodynamics	16
2.1.1 - Equation of Motion for Gas Component	17
2.1.2 - Equation of Continuity for Gas	18
2.1.3 - Equation of Motion for Dust Component	19
2.1.4 - Equation of Continuity for Dust Grains	19
2.2 - Equation of Energy Conservation for Radiation Field	20

2.3 - Special Cases, Initial Distributions and Boundary Conditions	20
2.3.1 - Initial Distributions and Boundary Conditions for the Velocity of Gas and Dust	20
2.3.2 - Temperature Distributions for Dust and Gas	22
2.3.3 - Density Distributions for Gas and Dust	23
2.4 - Algorithms	24
2.4.1 - Frequency Dependent Radiative Transfer Problem	24
2.4.2 - Henyey Method -- Numerical Method for Hydrodynamics	30
2.4.3 - A Simple Way to Find J and H	35
2.4.4 - Structure of the Program	38
Chapter 3 - Exploring Effects of Parameters	41
3.1 - Dust Condensation Temperature	41
3.2 - Dust Optical Properties -- Mie Theory	44
3.3 - Dust Grain Sizes	46
3.4 - Mass Loss Rates	53
3.5 - Dust to Gas Ratios	61
Chapter 4 - Model Results	68
4.1 - Stellar Parameters of Model Calculations	68
4.2 - Sample Calculations of AGB Stars	71
4.3 - Fitting of Spectral Energy Distributions	93
4.3.1 - IRAS Data	93
4.3.2 - Color Corrections	94

4.3.3 - Model Results for AFGL3068	97
4.3.4 - Model Results for o Ceti	98
4.3.5 - Model Results for OH25.6+0.6	99
Chapter 5 - Summary and Conclusions	108
Bibliography	111

List of Tables

Table 3.1 - The Minimum Mass Loss Rates	61
Table 3.2 - Stellar Parameters from Lambert et al.(1986)	63
Table 4.1 - Oxygen Star Mass-Loss Rates and Terminal Velocities from Observations	71
Table 4.2 - Carbon Star Mass-Loss Rates and Terminal Velocities from Observations	73
Table 4.3a - The Parameters for Carbon - rich Star ($M_*=2.5M_\odot$)	78
Table 4.3b - The Parameters for Carbon - rich Star ($M_*=1.5M_\odot$)	78
Table 4.3c - The Parameters for Oxygen - rich Star ($M_*=1.5M_\odot$)	78
Table 4.3d - The Parameters for Oxygen - rich Star ($M_*=3.0M_\odot$)	79
Table 4.3e - The Parameters for Oxygen - rich Star ($M_*=5.0M_\odot$)	79
Table 4.4 - Colour Correction Factors K	96
Table 4.5 - The Color Temperature and The Correction Factors for Sample Stars	97
Table 4.6 - Model and Derived Parameters	98

List of Figures

Figure 1.1 - The structure of an AGB star	4
Figure 1.2 - The mechanism for driving materials outward	9
Figure 2.1 - The (r,p) plane and the grid inside the envelope of AGB star	29
Figure 3.1 - Terminal gas, dust and drift velocities vs grain size	48
Figure 3.2 - Terminal gas outflow velocity as function of grain size for different mass loss rate	49
Figure 3.3 - The distribution of radiation acceleration on dust as function of radius for different dust size	51
Figure 3.4 - The distribution of coupling acceleration on gas as function of radius for different dust size	52
Figure 3.5 - The optical depth at 10 μ m as function of mass loss rate	54
Figure 3.6a - The emergent spectra for carbon-rich stars at different mass loss rate	55
Figure 3.6b - The emergent spectra for oxygen-rich stars at different mass loss rate	56
Figure 3.7 - Terminal gas, dust and drift velocities as the function of mass loss rate	58
Figure 3.8a - The distribution of radiation acceleration for different mass loss rate	59
Figure 3.8b - The distribution of coupling acceleration for different mass loss rate	60
Figure 3.9 - The terminal gas, dust and drift velocities vs dust-to-gas ratio	65
Figure 3.10a - The emergent spectra for carbon-rich stars at different dust-to-gas ratio	66

Figure 3.10b - The emergent spectra for oxygen-rich stars at different dust-to-gas ratio	67
Figure 4.1 - The terminal gas outflow velocity vs mass loss rate	77
Figure 4.2a - The velocity profiles for carbon-rich star (with $M_*=2.5M_\odot$)	80
Figure 4.2b - The velocity profiles for carbon-rich star (with $M_*=1.5M_\odot$)	81
Figure 4.2c - The velocity profiles for oxygen-rich star (with $M_0=1.5M_\odot$)	82
Figure 4.2d - The velocity profiles for carbon-rich star (with $M_0=3.0M_\odot$)	83
Figure 4.2c - The velocity profiles for oxygen-rich star (with $M_0=5.0M_\odot$)	84
Figure 4.3a - The model spectra at different radius for carbon-rich star (with $M_*=2.5M_\odot$)	85
Figure 4.3b - The model spectra at different radius for oxygen-rich star (with $M_0=3.0M_\odot$)	86
Figure 4.3c - The model spectra at different radius for oxygen-rich star (with $M_0=5.0M_\odot$)	87
Figure 4.4a - The emergent spectrum distributions for carbon stars (with $M_*=2.5M_\odot$)	88
Figure 4.4b - The emergent spectrum distributions for carbon stars (with $M_*=1.5M_\odot$)	89
Figure 4.4c - The emergent spectrum distributions for oxygen stars (with $M_0=1.5M_\odot$)	90
Figure 4.4d - The emergent spectrum distributions for oxygen stars (with $M_0=3.0M_\odot$)	91
Figure 4.4e - The emergent spectrum distributions for oxygen stars (with $M_0=5.0M_\odot$)	92
Figure 4.5a - The spectrum fitting for AFGL3068	100
Figure 4.5b - The spectrum distributions at different radii for AFGL3068 with the spectrum fitting at the outer radius	101

Figure 4.6a - The spectrum fitting for o Ceti	102
Figure 4.6b - The spectrum distributions at different radii for o Ceti with the spectrum fitting at the outer radius	103
Figure 4.7a - The spectrum fitting for OH25.6+0.6	104
Figure 4.7b - The spectrum distributions at different radii for OH25.6+0.6 with the spectrum fitting at the outer radius	105
Figure 4.8 - The density and velocity profiles for three sample stars	107

List of Symbols, Abbreviations, Nomenclature

β	collision parameter
λ	wavelength of electromagnetic wave
μ	mean molecular weight
μm	micrometer (10^{-6} meter)
ν	frequency of electromagnetic wave
π	3.1415926
ρ	the gas mass density
σ	the Stephan Boltzmann constant
ρ_d	the dust mass density
σ_{abs}	the absorption extinction coefficient
σ_{ext}	the extinction coefficient
σ_{sca}	the scattering extinction coefficient
σ_H	the flux mean extinction coefficient
τ	optical depth
τ_{10}	the optical depth at $10\mu\text{m}$
Φ	dust to gas ratio
Φ_0	the rest dust to gas ratio
a	the radius of dust grain
c	the speed of light
f	the fraction of grain material condensed

k	the Boltzman constant
m	the refractive index of the particle relative to the medium
m_d	the mass of dust grain
m_r	total mass inside the radius r
m_H	atomic mass of hydrogen
n	the optical constant (c/v)
n_d	the number density of dust grain
p	impact parameter
pc	par second
r	radius
r_*	radius of star
r_0	first radius of the envelope
t	time
u	the gas outflow velocity
v	the speed of light in the medium
v_{avg}	thermal mean velocity of gas
v_{drift}	the drift velocity between gas and dust
v_e	the terminal outflow velocity of gas
w	the dust outflow velocity
A	the molecular weight of dust grain
AFCRL	the same catalogue as AFGL (see below)
AFGL	Air Force Geophysical Laboratory

AGB	asymptotic giant branch
CRL	the same Catalogue as AFGL
CSE	Circumstellar Envelope
D	the distance
ESO	European Southern Observatory
F	the integrated flux in units of ergs/cm ²
F_{λ}	radiation flux in units of ergs/(cm ² s)
F_{ν}	radiation flux in units of ergs/(cm ² Hzs)
G	gravitational constant
H	integrated Eddington flux
HR	Hertzsprung--Russell
I, I(ν), I_{ν}	intensity of radiation field
IRAS	Infrared Astronomical Satellite
IRC	2 μ m sky survey Infrared Catalogue
J(ν)	mean intensity of radiation field
K	optical constant ($\omega(\epsilon\mu)^{1/2}$)
K(ν)	second moment of the radiation field
L_{\odot}	solar luminosity
L_{*}	stellar luminosity
LRS	Low Resolution Spectrum
LRSC	Low Resolution Spectrometer Catalogue
M_{\odot}	solar mass

M_*	stellar mass
M_0	initial stellar mass
M_{bol}	absolute bolometric magnitude
M_c	the core mass of AGB star
\dot{M}	the mass loss rate
NASA	National Aeronautic and Space Agency
P	gas pressure
PPN	proto-planetary nebula
Q	artificial viscous pressure
$Q(\nu)$	frequency dependent extinction efficiency
Q_{abs}	the absorption extinction efficiency
Q_{ext}	the extinction efficiency
Q_{sca}	the scattering extinction efficiency
Q_{F}	the flux mean extinction efficiency
$S_{\nu}(r)$	source function
T	temperature
T_c	colour temperature
T_{cond}	condensation temperature
T_d	dust temperature
T_{eff}	effective temperature
T_g	the gas temperature
V	the visual magnitude

Chapter 1 Introduction

1.1 Evolution of Asymptotic Giant Branch Stars

After all the hydrogen in the central region of a star is burnt into helium, the star moves away from the main sequence to Red Giant Branch (RGB) with the degenerate helium core surrounded by half-degenerate helium materials and hydrogen envelope. As the temperature rises in the central region (because of the contraction), the helium nuclei in the center are striking each other harder, and more frequently, at this situation, we would expect that, sooner or later, the degenerate helium nuclei would ignite to produce carbon and start to provide energy. The energy released from the central core burning is so high that it can ignite the partially degenerate helium in the surrounding shell. After all the helium is totally consumed throughout the entire central region of the star, the star moves away from RGB to Asymptotic Giant Branch with C-O core in the center surrounded by a helium burning shell and hydrogen envelope.

It is convenient to group Asymptotic Giant Branch (AGB) stars into two classes: those which have not yet begun to thermally pulse we designate as early-AGB (E-AGB) stars, while those that are in the thermally pulsing phase we designate as thermally pulsing AGB (TP-AGB) stars. While in the E-AGB phase, the hydrogen burning shell is extinct, and helium burning in a narrowing zone provides most of the energy reaching the stellar surface.

With an unimportant exception (Iben & Renzini 1983), L_* (the stellar luminosity) and T_{eff} (the effective temperature) are monotonic increasing functions of time during the E-

AGB phase. The relationship between T_{eff} and L_* is too sensitive to mass and composition to permit the construction of a simple analytic approximation that is valid for all masses and compositions. It must further be emphasized that the relationships between T_{eff} and L_* found in any model calculation for a given mass are at best acceptably reliable only with regard to the slope (in the H-R diagram).

Because of the temperature increase toward the end of the E-AGB phase for helium burning, hydrogen is reignited in a thin shell and the star begins to thermally pulse.

As in the case of helium-core flash, the dominant energy source for a thermal pulse is the triple alpha reaction. However, since the burning occurs in a region in which electrons are not degenerate (between the hydrogen-helium discontinuity and the electron degenerate C-O core), the energy that is liberated goes directly into raising the local pressure and initiating an expansion. Once the expansion has progressed far enough, cooling sets in and helium burning begins to die down. The expansion initiated by helium burning takes matter at and beyond the hydrogen-helium discontinuity out to such low temperatures and densities that hydrogen burning is effectively shut off. Ultimately, when the helium-burning luminosity L_{He} drops below the surface luminosity L , the matter that has been propelled outward falls back inward and heats until hydrogen is reignited. The helium-burning rate continues to drop and the hydrogen-burning rate continues to increase until a steady state is reached in which the hydrogen-burning luminosity L_{H} nearly equals L and $L_{\text{He}} \ll L_{\text{H}}$. Then ensues a long period during which quiescent hydrogen burning in a shell eats its way outward in mass until, after a critical mass has been processed, another thermal pulse is initiated.

As stated above, a TP-AGB star is in the phase of evolution containing two nuclear burning shells. The structure of a TP-AGB star can be described as follows: a very tiny, very compact hydrogen-exhausted core is surrounded by a very diluted, fully convective envelope containing still unprocessed materials as demonstrated in Figure 1.1. The hydrogen-burning shell is the interface between the core and the envelope and its radial extent is only about 10^{-4} of that of the stellar surface (Schonberner, Blocker & Marten 1994). For a major fraction of the AGB evolution, hydrogen burning provides nearly all the luminosity that is radiated away from the stellar surface and this luminosity increases with the mass of the core within the burning shell.

The early numerical calculations of AGB (here and hereafter AGB means TP-AGB) models have showed that such a structure with two burning shells is thermally unstable (Schwarzschild et al. 1965, Weigert 1966). The reasons are that the nearest terrestrial comparison for helium flash would be a bomb explosion and the energy output is unstable as stated above. This thermal instability of the helium-burning shell leads to the so-called thermal pulse or helium-shell flashes. Direct evidence for the occurrence of thermal pulses is provided by the observed rapid period changes in some Mira variables (Wood & Zarro 1981). From pulse to pulse, the core mass increases, and so does the luminosity. The luminosity increase along the AGB leads to stronger winds-larger mass loss rates as is known from infrared and radio observations as below.

The advent of infrared technology opened up a new era in the study of AGB mass loss. The 2.2 μm sky survey (IRC survey) by Neugebauer and Leighton (1969) discovered a new class of objects - those which possess infrared emission in excess of the expected

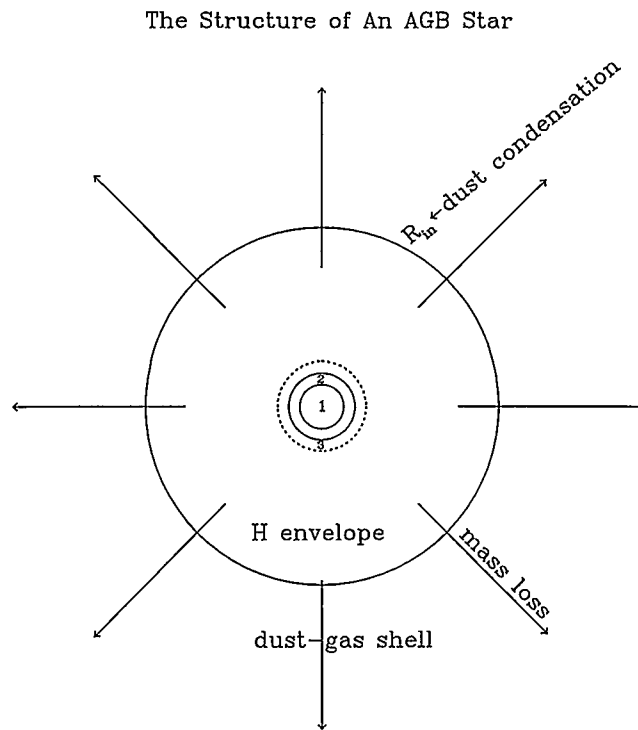


FIGURE 1.1 The structure of an AGB star. Inside the diagram "1" represents C-O core, "2" represents the helium burning shell and "3" represents the hydrogen burning shell.

photospheric continuum. The energy distribution of NML Cygni, for example, has a colour temperature of $\sim 600\text{K}$ which obviously cannot be due to photospheric emission from a star. It was soon realized that these stars are surrounded by thick layers of dust which absorb the visible light emitted by the star and re-emit it in the infrared.

Later, Woolf and Ney (1969) discovered a well-defined emission feature at the wavelength of $10\ \mu\text{m}$ in a number of cool stars and attributed it to silicate grains. Further broad-band photometry revealed that this feature is common to most giants with spectral types later than M3. Chemical equilibrium calculations by Gilman (1969) supported this identification by showing that silicate grains should be the first solid particles to condense in oxygen-rich stars. For carbon-rich stars, the first condensation should be carbon and silicon carbide. Subsequently, further spectrophotometry at longer wavelengths was reported by Hackwell (1972), and the presence of a narrower emission band centered near $11.3\ \mu\text{m}$ in the spectra of carbon stars was identified with circumstellar SiC grains (Gilra 1972). After studying the infrared spectrophotometry of stellar objects over the wavelength range from 2 to $14\ \mu\text{m}$ Merrill and Stein (1976) concluded that the broad $9.7\ \mu\text{m}$ emission feature is unique to oxygen-rich stars and the narrow $11.3\ \mu\text{m}$ emission feature is unique to carbon-rich stars, and the circumstellar dust envelopes of these sources are generally more optically thick than those found in normal comparison stars.

The Air Force Geophysical Laboratory (AFGL) rocket survey of the sky at 4 , 11 , $20\ \mu\text{m}$ has resulted in a catalog of approximately 3000 objects (Walker & Price 1975). Many of these sources are discovered with large far infrared excess but no optical counterparts.

While many infrared stars were discovered by the IRC and AFGL sky survey, a

comprehensive picture of the distribution and properties of late AGB stars emerged only after the launch of the Infrared Astronomical Satellite (IRAS). The classification of many previously unknown infrared sources detected by IRAS is made possible by the observations of circumstellar dust features by the Low Resolution Spectrometer (LRS) on IRAS. The observed strength of silicate feature varies from emission to absorption suggests an increasing optical depth of the circumstellar envelope, and this has been interpreted as increasing rates of mass loss as the star ascends the asymptotic giant branch (Volk & Kwok 1987, Kwok 1990). This is supported by the fact that the objects with deepest silicate absorption features are often also heavily obscured in the optical range. There is no doubt that the infrared excess observed in late type stars is a clear manifestation of mass loss.

The double-peaked profile with a steep gradient on the outside edges of 18 cm OH maser emission associated with late-type stars and the CO molecule emission on both oxygen and carbon rich stars also show the mass loss on AGB stars (Kwok 1976, Elitzur et al. 1976). Since agreement between the theoretical and observational line profiles firmly establishes that the stellar velocity is at the mid-point of the two peaks and the terminal expansion velocity of the circumstellar envelope (CSE) is given by half of the velocity separation (Kwok 1976, 1987), observations of the OH profiles therefore allow us to determine the terminal velocity of the stellar wind very accurately. We also can obtain the stellar wind velocity by fitting the observation profiles of CO emission lines (Knapp & Morris 1985, Wannier & Sahai 1986).

Although much effort has been devoted to understanding the mass loss rate of the AGB

star, we are still far from a position where we are able to predict mass loss rates for any given AGB star parameters. Evolutionary calculations then have to resort to empirical or semi-empirical descriptions for a whole range of initial masses. Bryan, Volk and Kwok (1990) obtained a semi-empirical formula for mass loss rate, and use it to get the initial-final mass relationships which are close to the observations of Weidemann and Koester (1983) (The initial-final mass relation is the relation between the mass at the beginning of an AGB star and the mass at the ending of a star as a white dwarf). Vassiliadis & Wood (1993) constructed a mass loss formula by combining empirical relationships between mass loss rates and pulsational periods. Blöcker(1993, 1995a, 1995b) utilized the hydrodynamic calculations of pulsating Mira atmospheres performed by Bowen (1988) to construct a semi-empirical mass loss formula.

As materials are blown away, the stellar surface temperature will increase, one can expect that the dust formation will come to end somehow for the high temperature will destroy the dust material, which would then reduce the mass loss rate by orders of magnitudes. Thus this will quickly terminate the AGB evolution. As the inner rim of the dusty shell moves away, the shell dilutes, cools off and the star evolves towards the planetary nebulae phase.

As the conclusion of an AGB star, the thermal pulse and mass loss are the two essential features of an AGB star: the thermal pulse and the mass loss. The importance of the mass loss is demonstrated by the fact that the progeny of AGB stars, the planetary nebula nuclei (PNNs) and white dwarfs, have mass distributions peaked closely around $0.6 M_{\odot}$ (Weidemann & Koester 1983; Kwok 1985, Weidemann 1990, Zhang & Kwok 1993)

while the main-sequence masses of these objects must have been $\geq 1 M_{\odot}$ (Pottash 1984, Jura 1990). For the detailed information about the evolution of AGB stars and the effects of mass loss rate, please read the review papers written by Iben and Renzini (1983), Kwok (1987) and Schönberner et al. (1994).

1.2 The Mechanism for Driving Materials Outward

Infrared observations have indicated silicate materials in the envelopes of oxygen-rich stars and graphite and silicon carbide in the envelopes of cool carbon-rich stars. Gilman (1969) has shown that graphite carbide could arise from cool carbon stars, and iron and silicate particles may arise from cool oxygen-rich stars. It is commonly assumed that the most likely mechanism for the observed mass loss in late-type stars is radiation pressure acting on small grains which in turn are coupled to the gas. However, Weymann (1962a) has questioned whether the grains would be sufficiently coupled to the gas to permit the above mechanism to work.

In considering grain-gas coupling it is helpful to distinguish between two types of coupling: momentum coupling and position coupling. Momentum coupling requires only that the momentum absorbed by grains from the radiation field be approximately equal to the momentum which the grains give to the gas through collisions while position coupling requires that the grains be moving in some sense slowly through the gas, e.g., that the drift velocity (relative velocity) between grains and gas be small compared to the gas velocity. One type of coupling does not necessarily imply the other, and for the mechanism of radiation pressure to grain to gas, it is momentum coupling that is

The Mechanism for Driving Materials Outward by

Radiation Pressure

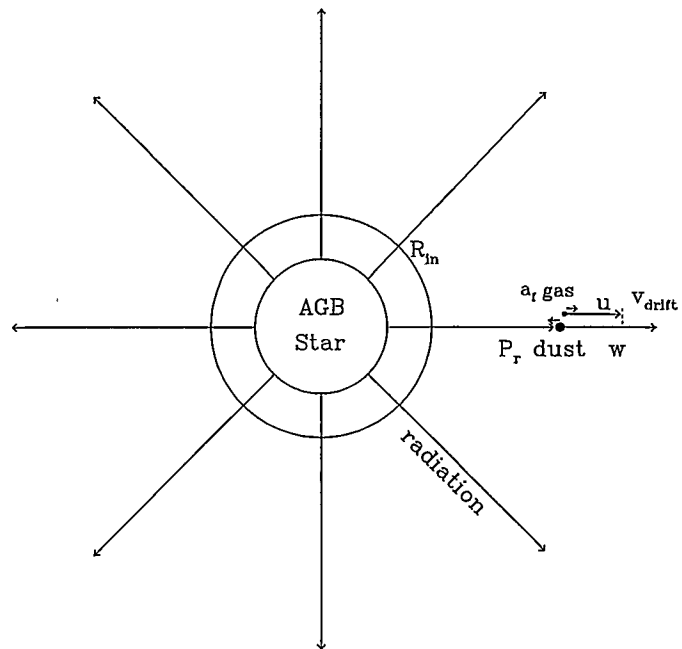


FIGURE 1.2 The mechanism for driving materials outward in late-type stars. Where w is the dust velocity, u is the gas velocity and v_{drift} is the relative velocity between dust and gas.

important (Gilman 1972).

In Weymann's argument gas can gain momentum only through direct collisions with the grain. It was pointed out by Gilman (1972) that the majority of the gas molecules gain momentum through collisions with other gas molecules. As a result, the momentum of the dust grain is diffused throughout the gas.

Now we have the idea about the mechanism for the mass loss in late-type stars: dust grains condense in a cool outflow materials, the radiation pressure from the central star acting on the newly formed grains pushes dust grains outward and collisions between gas and dust move the gas materials outward as demonstrated in Figure 1.2. This idea has been only theoretically studied by analytical approximations (Gehrz & Woolf 1971, Gilman 1972) until the numerical solutions to the equation of motion were obtained by Kwok (1975). Recent investigations of the radiation driven winds are given by Netzer & Elitzur (1993) and Habing et al. (1994).

1.3 Application of Hydrodynamics and Radiative Transfer to Stellar Envelopes

The hydrodynamic evolution of the envelope of a star is very interesting for astrophysics. It is very important for the star formation from clouds and the evolution of a later type star. Since the obscuring matter in the envelope hides the core from an observer at all but the very far IR wavelengths, if one wants to interpret the radiation spectrum of the observations and understand the velocity and density distributions inside the envelope, one has to construct a hydrodynamic model coupled with the radiative transfer for the stellar wind. It is generally believed that radiation pressure acting on dust

grains is the driving force of stellar outflows from late-type giants and supergiants (Gilmann 1972, Salpeter 1974, Kwok 1975, Goldreich & Scoville 1976, Tielens 1983, Gail & Sedlmayr 1985, Netzer & Elitzur 1993 and Habing et al. 1994). As the gas cools below a certain temperature around 1000 K (Tielens 1983; Gail & Sedlmayr 1986, Cohen & Tielens 1989; Schutte & Tielens 1989) heavy elements condense, radiation pressure acts on the dust grains, and momentum is transferred from the dust grains to the gas molecules by collisions.

As the dust forms inside the envelope, it will absorb the UV photons from the star and re-emit them at infrared wavelengths. The dust extinction coefficient is strongly dependent on the frequency and the spectral energy distribution inside the envelope. So the spectrum determines the radiation pressure which determines the outflow velocity of the dust and thus also the dust density; on the other hand the dust density determines the spectral distribution. All these parameters are position dependent, so is the dust opacity. Another reason for dependence on the position for dust opacity is that the outflow is a two fluid system. As mentioned in the works of Kwok (1975) and Netzer & Elitzur (1993) it consists of dust and gas, and the dust moves supersonically within the gas, reaching its terminal velocity faster than does the gas. Thus the dust to gas ratio is reduced relative to its rest value by the ratio of the two outflow velocities which are not constant through the envelope. This non-constant velocity is also manifested by the observational evidence that the outflow is accelerated gradually in certain supergiants (Chapman & Cohen 1986; Bowers & Johnston 1990). Thus if one wants to understand what is the process inside the envelope of an AGB star, one has to solve the hydrodynamics coupled with detailed

radiative transfer problem.

Several authors have developed the method to solve the radiative transfer problem in the past. Leung (1975) developed a numerical method to solve the problem of the radiation transfer in dense interstellar dust clouds in spherical or planar geometry. The basic idea of this model is to solve the radiative transfer problem as a two-point boundary value problem by evaluating a set of moment of the radiation field and energy balance equation of dust emission and absorption in the iterative manner to determine the source function by assuming a uniform dust mass density distribution. The intensity distribution and the total energy flux are then calculated from the derived source function. Rowan-Robinson (1980) has developed a model which integrates the equation of radiative transfer in a spherically symmetric dust cloud illuminated by a central star to obtain the emergent spectrum distribution assuming a certain density distribution by ignoring the dynamic effects. In this model the intensity was split up into three components: 1) the intensity from the central illuminating source which was assumed not to suffer the extinction; 2) the radiation from dust grains; 3) the scattered light. Therefore the radiative transfer equation was split into three simple integrating equations.

The numerical solution for the stellar wind was unavailable until Kwok (1975) constructed a quantitative dynamic model to seek numerical solutions to the equation of motion by including the effects of (a) radiation pressure on grains; (b) gravitational attraction by the star; (c) growth of grains; (d) momentum transfer from the grain to the gas; (e) sputtering of the grains to investigate the process of radiation on the dust to explain the mass loss observed in cool giants for optically thin case in a spherical

geometry. In his model the momentum coupling term between gas and dust grains was derived for the first time ever. Tielens (1983) has developed a model for a stellar wind driven by radiation pressure on dust grains in the circumstellar envelopes of Mira variables by ignoring the effects of the radiative transfer. In this model the outflow was treated as a two-component fluid, consisting of gas and dust particles, and the temperature structure was determined by three competitive process: the viscous heating by gas-grain collisions, the H_2O rotational cooling and the cooling due to expansion. Gail and Sedlmayr (1985) constructed a dynamic model for dust condensation in the stellar wind around cool supergiants for carbon-rich stars. In their model, the coupled system of equation for dust grain formation and growth was solved numerically by assuming that the supersonic wind is driving by dust condensation and ignoring the difference between the gas and dust velocities and the radiative transfer effects even under the optically thick case.

As stated above, a complete solution of the dynamics outflows must involve a solution of the radiative transfer problem in the dusty envelopes. The most recent work on the dynamics of stellar outflows are by Netzer & Elitzur (1993) and Habing et al. (1994). Netzer and Elitzur have constructed a model with dynamic equations for both dust and gas coupled with approximate radiative transfer solutions by ignoring the effect of gas pressure. In their model, the radiation field was separated into two components: one corresponds to photons emanating from the central star that were assumed not to be absorbed nor scattered by dust and the other corresponds to the diffuse radiation, consisting of photons emitted or scattered by dust grains. Habing et al. have solved three

simplified models by assuming the radius-independent efficiency of dust grain.

As mentioned above, the stellar outflows are a two fluid system. In this work the dust and gas are treated separately in the hydrodynamic equations and the relation between the dust and gas is produced by an interaction term. We try to solve the problem within the full solution of the hydrodynamics and detailed radiative transfer coupled together including all the forces exerted on the dust and the gas. The goal here is to understand the distribution of velocities and densities of gas and dust in the stellar outflow and to fit the infrared LRS spectra from IRAS for optically thick AGB stars.

Several papers have been published for fitting infrared spectra. Rowan-Robinson & Harris (1982, 1983) solved the radiation transfer problem by assuming a given mass density distribution inside the shell to model the observational spectra of late type stars (from M0 to M5 or later). Volk & Kwok (1987, 1988) obtained the evolution of the infrared spectra of AGB stars using time-dependent radiative transfer models based on a simple mass-loss formula by assuming the constant velocity distribution (or inverse square density distribution $\rho \propto r^{-2}$). The radiative transfer model used to produce the model spectra was adopted from the program DUSTCD developed by Leung (1975) for the modeling of dust in molecular clouds and star-formation regions.

In our model we use the hydrodynamics solution for density and velocity distributions instead of assuming certain distribution and solve the detailed radiative transfer problem instead of approximate solutions. Chapter 2 describes the radiative hydrodynamics model; chapter 3 discusses the effects of parameters; chapter 4 presents the model results; chapter 5 gives the summary and conclusions.

Chapter 2 The Model

The problem of the evolution of envelopes of AGB stars is complicated in that on one hand radiation pressure determines the outflow velocity of the dust and thus also the dust density; on the other hand the dust density determines, via radiative transfer effects, the spectrum of the photons and thus the effective radiation pressure. To solve this problem we have to find the equations of hydrodynamics, which describe the motion of gas and dust, and the equation of the radiative transfer, and solve these equations simultaneously.

The program used here is based on one--dimensional radiation-hydrodynamic formulae which solve the time--dependent equations of hydrodynamics and radiative transfer in spherical geometry for a two component fluid consisting of gas and dust. The code was originally written and applied to investigate the dynamical evolution of protostellar clouds by Yorke (1977, 1980a, 1980b). We develop it to investigate the dynamical evolution of the envelopes of late type stars. In this chapter we are going to investigate the equations of motion for dust and gas components and the equation for radiative transfer inside the envelope of an AGB star. We also give details about how to solve the radiative transfer numerically and the numerical method of solving the hydrodynamics equations coupled with the equation of energy conservation of the radiation field.

The general idea for the numerical method is iterative. First of all we have to find the initial and boundary conditions for each parameter and use them to solve the detailed non-gray radiative transfer problem to obtain the approximate radiation field, and use the obtained radiation field to solve the hydrodynamic equations coupled with the equation

of energy conservation of the radiation field to update the parameters. Once the new parameters are obtained we can use them to find the more accurate radiation field and then to obtain the more accurate parameters by repeating the above steps until we obtain consistent solutions for the envelope. We use our radiative hydrodynamics model to obtain steady state solutions for non-gray case.

2.1 Hydrodynamics

It is usually assumed that dust formation is an abrupt process that occurs as a phase transition when the temperature decreases below a certain value (eg. Goldreich & Scoville 1976). However there are considerable uncertainties. At small radii collisions among the dust grains can lead to coalescence or breakup. In addition, not all the species condense at the same temperature and grains can keep growing after their initial formation (Kwok 1975). Even though in a steady outflow one might expect grain growth to stop at large radii for kinetic reasons (eg. the drop in gas density), it is quite likely that clumps are present and hence the continued accretion is feasible. Unfortunately, no adequate modelling has yet been performed to describe clumps and their effects in a quantitative manner. In our model calculations we keep the same dust grain size and number after dust grains are formed in inner radius.

On the other hand, all of these uncertainties are dwarfed by another effect, that the dust flows out faster than does the gas, resulting in a two component fluid. Thus the dust to gas ratio and hence the dust opacity is reduced by a factor u/w , where u and w are the outflow velocities of gas and dust, respectively. To account for this difference in

velocities, the gas and dust must be treated separately in the hydrodynamic equations.

2.1.1 Equation of Motion for Gas Component

The forces acting on the gas in a circumstellar envelope are: the gravitational pull of the star, the outward force due to the interaction between dust and gas, and the gas pressure gradient. The coupling between dust and gas can be estimated by adopting the following simplified picture: a perfect sphere is moving at velocity v_d (the relative velocity between dust and gas, $v_d = w - u$) in a field of gas particles with Maxwellian velocities of temperature T . After taking the average of encounters from all possible directions the rate of momentum transfer takes the form (Kwok 1975) of $\pi a^2 \rho v_d v_T$ in the limit of $v_d \ll v_T$, where $v_T = 3/4(3kT/\mu m_H)^{1/2}$. In the case of $v_d \gg v_T$, the coupling can be approximated by $\pi a^2 \rho v_d^2$. We use the following expression to connect these two regions: $\pi a^2 \rho v_d (v_d^2 + v_T^2)^{1/2}$ and define the collision parameter as

$$\beta = \langle \pi a^2 \rangle \left[\frac{8kT_g}{\pi \mu m_H} + (u-w)^2 \right]^{1/2}, \quad (1)$$

where a is the radius of dust grain, $k = 1.3805 \times 10^{-16}$ ergs/K is the Boltzmann constant, μ is the mean molecular weight of the gas in AMU (eg. if the molecular gas composition of $H_2:He:C:N:O$ is assumed to be $1:0.1:3 \times 10^{-4}:1 \times 10^{-4}:6 \times 10^{-4}$, then $\mu = 2.2848$), m_H is the atomic hydrogen mass, T_g is the gas temperature.

So the motion equation for gas is

$$\frac{\partial u}{\partial t} + u \frac{\partial u}{\partial r} + \frac{GM_*}{r^2} - n_d (w-u) \beta + \frac{1}{\rho} \frac{\partial (P + Q)}{\partial r} = 0 , \quad (2)$$

where $G = 6.67 \times 10^{-8} \text{ dyne} \cdot \text{cm}^2 / \text{g}^2$ is the gravitational constant, M_* is the stellar mass, ρ is the mass density of gas, and n_d is the dust number density; P is the gas pressure given by

$$P = \frac{k \rho T_g}{\mu m_H} ; \quad (3)$$

Q is the "artificial" viscous pressure come from the internal friction of the gas given by

$$Q = \begin{cases} l^2 \rho \left(\frac{\partial u}{\partial r} \right)^2 & \frac{\partial u}{\partial r} < 0 \\ 0 & \frac{\partial u}{\partial r} \geq 0 \end{cases} , \quad (4)$$

here l is the viscous coefficient.

2.1.2 Equation of Continuity for Gas

The equation of continuity for gas is

$$\frac{\partial \rho}{\partial t} + u \frac{\partial \rho}{\partial r} + \rho \frac{\partial u}{\partial r} + \frac{2u\rho}{r} = 0 . \quad (5)$$

After performing some transformations, equation (5) can be changed into the following form

$$\frac{\partial l g \rho}{\partial t} + \frac{3 l g e}{\rho} \frac{\partial (\rho u r^2)}{\partial (r^3)} = 0 , \quad (5')$$

where $e = 2.7182818$ and lg is the abbreviation for \log_{10} .

2.1.3 Equation of Motion for Dust Component

The forces acting on the dust grains are: the radiation pressure, the gravitational pull by the central star, and the drag force by the gas due to friction. Thus the equation of motion for the dust component is

$$\frac{\partial w}{\partial t} + w \frac{\partial w}{\partial r} - \frac{Q_F \pi a^2 L_*}{4 \pi r^2 c m_d} + \frac{GM_*}{r^2} + \frac{\rho}{m_d} (w-u) \beta = 0 \quad , \quad (6)$$

where c is the speed of light, L_* is the luminosity of the star, m_d is the mass of the dust particles; Q_F is the flux-mean extinction efficiency defined as:

$$Q_F = \frac{\int_0^\infty Q(\nu) F(\nu) d\nu}{\int_0^\infty F(\nu) d\nu} \quad , \quad (7)$$

where $Q(\nu)$ is the frequency dependent extinction efficiency and $F(\nu)$ is the flux of the radiation field.

2.1.4 Equation of Continuity for Dust Grains

The equation of continuity for dust grains is

$$\frac{\partial n_d}{\partial t} + w \frac{\partial n_d}{\partial r} + n_d \frac{\partial w}{\partial r} + \frac{2wn_d}{r} = 0 \quad . \quad (8)$$

After some transformations equation (8) becomes

$$\frac{\partial \ln n_d}{\partial t} + \frac{3 \ln e}{n_d} \frac{\partial (n_d w r^2)}{\partial (r^3)} = 0 \quad . \quad (8')$$

2.2 Equation of Energy Conservation for the Radiation Field

The thermal structure of the stellar outflow is assumed to be dominated by the radiation field. The condition of radiative equilibrium at any time and any radius is given by

$$\frac{1}{r^2} \frac{\partial}{\partial r} (4\pi r^2 H) = 0 \quad , \quad (9)$$

where H is Eddington flux (first moment of the radiation field) integrated over frequency for the radiation field. The frequency integrated radiative energy flux F is related to H such that

$$4\pi H = F = \int_0^\infty dv \int_0^{\omega_0} I(v) \cos\theta d\omega \quad . \quad (10)$$

To get the radiative energy flux F one has to solve the radiative transfer problem inside the envelope.

2.3 Special Cases, Initial and Boundary Conditions

2.3.1 Initial Distributions and Boundary Conditions for the Velocities of Gas and Dust

For steady outflow and ignoring artificial viscosity Q, Equation (1) can be simplified to

$$u \frac{\partial u}{\partial r} + \frac{GM_r}{r^2} - n_d (w-u) \beta + \frac{1}{\rho} \frac{\partial P}{\partial r} = 0 \quad . \quad (11)$$

Furthermore, if the difference between w and u can be ignored, it means that the coupling between dust and gas is perfect, so almost all the dust momentum is transferred to the

gas, then the coupling term in equation (11) can be changed to $\Phi Q_F \pi a^2 L_* / (4\pi r^2 c m_d)$ according to Gail & Seldmayr (1985) for perfect coupling condition. Equation (11) can be changed to the form

$$u \frac{\partial u}{\partial r} + \frac{GM_r}{r^2} + \frac{1}{\rho} \frac{\partial P}{\partial r} - \Phi \frac{Q_F \pi a^2 L_*}{4\pi r^2 c m_d} = 0 \quad . \quad (12)$$

where $\Phi = \Phi_0 u/w$ is the dust to gas ratio and Φ_0 is the rest dust to gas ratio.

After performing the integration over r , one can get the initial velocity distribution of gas in the form (we ignore the gravitational deceleration here for it is much smaller than the radiation acceleration (Kwok 1975))

$$u^2(r) = u^2(r_0) + \frac{\chi_F L_*}{2\pi r_0 c} \left(1 - \frac{r_0}{r}\right) - \frac{2k}{\mu m_H} y[r, T_g(r), \rho(r)] \quad , \quad (13)$$

with the function $y[r, T_g(r), \rho(r)]$

$$y[r, T_g(r), \rho(r)] = T_g(r) - T_g(r_0) + \bar{T}_g \ln \frac{\rho(r)}{\rho(r_0)} \quad ,$$

where \bar{T}_g is the mean gas temperature over the range of r , χ_F is the flux mean opacity of dust,

$$\chi_F = \Phi \frac{Q_F \pi a^2}{m_d} = \Phi \frac{\pi a^2 \int_0^\infty Q(\nu) F(\nu) d\nu}{m_d \int_0^\infty F(\nu) d\nu} \quad , \quad (14)$$

and $u(r_0)$ is the gas velocity at the inner boundary of the shell which can be assumed to be any small value. Since it is much smaller than the terminal velocity (the gas velocity at the outer radius), the implication of its exact value for the solution is negligible. This

is true for both the gray (the optical properties are independent of the frequency) and non-gray cases (Netzer & Elitzur 1993).

For steady outflow, the first term of equation (6) $\partial w/\partial t$ is zero, and if the second term of equation (6) $\partial w/\partial r$ can be ignored (i.e. dust does not pass through a shock) then equation (6) can be simplified to

$$\frac{GM_r}{r^2} - \frac{\pi a^2 Q_F L_*}{m_d 4\pi r^2 c} + \frac{\rho \pi a^2}{m_d} v_{drift} (v_{avg}^2 + v_{drift}^2)^{\frac{1}{2}} = 0 \quad , \quad (15)$$

where v_{avg} is the thermal mean velocity of the gas, $v_{avg} = (8kT_g/\pi\mu m_H)^{1/2}$, and $v_{drift} = w - u$, is the velocity difference between gas and dust. Solving the above equation for drift velocity one has

$$v_{drift} = \sqrt{\frac{1}{2} \left\{ \left[\left(\frac{Q_F L_*}{2\pi r^2 c \rho} - \frac{m_d}{\pi a^2 \rho} \frac{2GM_r}{r^2} \right)^2 + v_{avg}^4 \right]^{\frac{1}{2}} - v_{avg}^2 \right\}} \quad . \quad (16)$$

From equations (13) and (16), the dust velocity distribution can be obtained as $w = u + v_{drift}$

2.3.2 Temperature Distributions for Dust and Gas

The inner radius of the envelope is determined by the assumption that this is where the dust forms. The temperature at this point is assumed to be the dust condensation temperature. The dust temperature inside the dust shell can be determined by solving the radiative equilibrium equation for dust

$$\int_0^\infty \sigma_{abs}(\nu) J(\nu) d\nu = \int_0^\infty \sigma_{abs}(\nu) B(\nu, T) d\nu \quad , \quad (17)$$

where $\sigma_{\text{abs}}(\nu)$ is the absorption cross section of the dust, $B(\nu, T)$ is the blackbody radiation field of the dust at temperature T , and $J(\nu)$ is the mean intensity of the radiation field. To the first approximation, when dust absorption can be ignored the mean intensity of the radiation field is simply given by the diluted radiation field of the central star, this is

$$J(\nu) = \frac{\int_0^{\omega_0} I_\nu(T_{\text{eff}}) d\omega}{4\pi} = \frac{1}{2} I_\nu(T_{\text{eff}}) \left[1 - \sqrt{1 - \left(\frac{r_*}{r}\right)^2} \right], \quad (18)$$

where T_{eff} is the stellar effective temperature; r_* is the radius of the star.

Let $\int_0^\infty I_\nu(T_{\text{eff}}) \sigma_{\text{abs}}(\nu) d\nu / \int_0^\infty \sigma_{\text{abs}}(\nu) B(\nu, T_{\text{cond}}) d\nu = r_c$; and solving equations (17) and (18) for the first radius of the envelope r_0 , we get

$$r_0 = \frac{r_*}{\sqrt{1 - (1 - 2/r_c)^2}}. \quad (19)$$

In the next iteration, we can use the result of detailed radiative transfer solution for $J(\nu)$ to solve equations (17) and (18) to get more accurate r_0 and dust temperature inside the shell.

Little is known about the behaviour of the gas temperature inside the envelope of an AGB star, $T_g = T_d$ is assumed throughout the envelope, although it needs some modification in the future. Fortunately, we just use the dust emission as the source function in our calculation, so the gas temperature is not very important here (see below).

2.3.3 Density Distribution for Gas and Dust

If only the steady and spherical outflow is considered, the density distribution for gas and dust can be obtained by using the continuity equation of mass:

$$4\pi r^2 \rho v = \psi \dot{M} \quad , \quad (20)$$

where \dot{M} is the mass loss rate; v is the velocity of gas or dust; ψ is the fraction, $\psi = 1$ for gas (then $v = u$) and $\psi = \Phi$ the dust to gas ratio for dust (then $v = w$). From equations (13), (16) and (20), we can get the initial density distribution for gas and dust. Once the temperature, velocity, and density distributions are obtained, one is ready to solve the radiative transfer to get the initial intensity and flux distribution inside the shell.

2.4 Algorithms

A steady and spherical outflow is assumed inside the envelope of an AGB star, so the model calculations are based on a one-dimensional radiation hydrodynamic code solving the time dependent equations of hydrodynamics and radiative transfer in spherical geometry for a two component fluid system consisting of gas and dust.

In this model, we use the initial conditions to get the distribution of parameters such as u , w , ρ , n_d , T_g and T_d with radius, then solve the radiative transfer problem to obtain the intensity and flux of the radiation field, and use these intensities and fluxes to solve equation (17) to get T_g , T_d , and the hydrodynamic equations (1), (5'), (6) and (8') coupling with the energy equation (9) to get the new u , w , ρ , n_d . Once we have these new parameters, we solve the radiative transfer problem again to get the new intensities and fluxes and so on until we get a consistent solution.

2.4.1 Frequency Dependent Radiative Transfer Problem

The time dependent non-relativistic equation for radiation transport in spherical

geometry including isotropic scattering can be written as

$$\frac{1}{c} \frac{\partial I_\nu}{\partial t} + \mu \frac{\partial I_\nu}{\partial r} + \frac{1 - \mu^2}{r} \frac{\partial I_\nu}{\partial \mu} = -\sigma_\nu^a(r) I_\nu + j_\nu(r) - \sigma_\nu^s(r) I_\nu \quad (21)$$

where $I_\nu = I_\nu(r, \mu, t)$ is the intensity of radiation of frequency ν , at time t and radius r in the direction $\mu = \cos\theta$, and θ is the angle between the outward normal and photon propagation directions, $j_\nu(r)$ is the isotropic emissivity, and $\sigma_\nu^a(r)$ and $\sigma_\nu^s(r)$ are the frequency dependent absorption and scattering coefficients at radius r (the relation between $Q(\nu)$ and $\sigma_\nu^a(r)$ and $\sigma_\nu^s(r)$ is $Q(\nu)\pi a^2 = \sigma_\nu^a(r) + \sigma_\nu^s(r)$).

By a simple change of variables (Hummer & Rybicki 1971) $(r, \mu) \rightarrow (r, p)$, where the impact parameter $p = r(1 - \mu^2)^{1/2}$, the specific intensity is divided into two components

$$I_\nu(r, \mu, t) \rightarrow \begin{cases} I_\nu^+(r, p, t) & \mu \geq 0 \\ I_\nu^-(r, p, t) & \mu < 0 \end{cases}, \quad (22)$$

and equation (21) can be written as two equations:

$$\frac{1}{c} \frac{\partial I_\nu^+}{\partial t} + \mu \frac{\partial I_\nu^+}{\partial r} = -(\sigma_\nu^a + \sigma_\nu^s) (I_\nu^+ - S_\nu), \quad (23)$$

$$\frac{1}{c} \frac{\partial I_\nu^-}{\partial t} - \mu \frac{\partial I_\nu^-}{\partial r} = -(\sigma_\nu^a + \sigma_\nu^s) (I_\nu^- - S_\nu), \quad (24)$$

where the variables I_ν^+ , I_ν^- and $\mu = (1 - p^2/r^2)^{1/2}$ in equations (23) and (24) are functions of the independent variables r , p and t . Because p can not distinguish the cases $\mu \geq 0$ and $\mu < 0$, the intensity $I_\nu(r, \mu, t)$ has to be separated into I_ν^+ for positive μ and I_ν^- for negative μ , and S_ν is the source function defined as

$$S_\nu = \frac{1}{\sigma_\nu^a + \sigma_\nu^s} (\sigma_\nu^a B_\nu + \sigma_\nu^s J(\nu)) , \quad (25)$$

where σ_ν^a and σ_ν^s are the dust absorption and scattering coefficients respectively, B_ν is the blackbody radiation of dust, $J(\nu)$ is defined by:

$$J(\nu) = \frac{1}{2} \int_0^1 (I_\nu^+ + I_\nu^-) d\mu . \quad (26)$$

For the first iteration $J(\nu)$ can be obtained from the equation (18).

For the steady outflows, equations (23) and (24) can be written as:

$$\mu \frac{\partial I_\nu^+}{\partial r} = -(\sigma_\nu^a + \sigma_\nu^s) (I_\nu^+ - S_\nu) , \quad (27)$$

$$\mu \frac{\partial I_\nu^-}{\partial r} = (\sigma_\nu^a + \sigma_\nu^s) (I_\nu^- - S_\nu) . \quad (28)$$

Once we obtain I_ν^+ and I_ν^- , we can get the first moment $H(\nu)$ and the second moment $K(\nu)$ of the radiation field:

$$H(\nu) = \frac{1}{2} \int_0^1 (I_\nu^+ - I_\nu^-) \mu d\mu , \quad (29)$$

$$K(\nu) = \frac{1}{2} \int_0^1 (I_\nu^+ + I_\nu^-) \mu^2 d\mu . \quad (30)$$

As shown in Figure 2.1, the computational space between the first and the last radii of the shell is divided into N grid points with index j , which are logarithmically spaced (i.e. r_{j+1}/r_j is constant). As far as the impact parameter p is concerned, for $r_1 \leq p \leq r_N$, we assume that p coincides with r , while for $p < r_1$, we introduce $NJ - N$ additional impact

parameters with equal spacing (NJ is the total number of impact parameters used in the calculations).

If the source function $S_v(r)$ and the extinction coefficient $\sigma_v^{\text{ext}}(r) = \sigma_v^a(r) + \sigma_v^s(r)$ are assumed to be constant between r_{j-1} and r_j , and we define $d\tau_v = (\sigma_v^a + \sigma_v^s)dr$, after multiplying both sides of equation (27) by $e^{\tau_v/\mu}$ or by $e^{-\tau_v/\mu}$ in the case of equation (28), we can carry out the integration between r_{j-1} to r_j at impact parameter p_k , and get the solution as:

$$I_v^+ e^{\tau_v/\mu} \Big|_{\tau_v(x_j)}^{\tau_v(x_{j-1})} = \frac{1}{\mu} S_v(\tau_v) \mu e^{\tau_v/\mu} \Big|_{\tau_v(x_j)}^{\tau_v(x_{j-1})} , \quad (31)$$

$$I_v^- e^{-\tau_v/\mu} \Big|_{\tau_v(x_j)}^{\tau_v(x_{j-1})} = \frac{1}{\mu} S_v(\tau_v) \mu e^{-\tau_v/\mu} \Big|_{\tau_v(x_j)}^{\tau_v(x_{j-1})} . \quad (32)$$

If we define $\tau_v(r_j) - \tau_v(r_{j-1}) = \Delta\tau_v$, then

$$I_v^+(r_{j-1}) = I_v^+(r_j) e^{-\Delta\tau_v/\mu} + S_v(1 - e^{-\Delta\tau_v/\mu}) , \quad (33)$$

$$I_v^-(r_{j-1}) = I_v^-(r_j) e^{\Delta\tau_v/\mu} + S_v(1 - e^{\Delta\tau_v/\mu}) . \quad (34)$$

Rearranging the terms of equations (33) and (34) gives

$$I_v^+(r_{j-1}) = [I_v^+(r_j) - S_v] e^{-\Delta\tau_v/\mu} + S_v , \quad (35)$$

$$I_v^-(r_{j-1}) = [I_v^-(r_j) - S_v] e^{\Delta\tau_v/\mu} + S_v . \quad (36)$$

Actually, the dust temperature and density are not constant with radius, so the $S_v(r)$ and $\sigma_v^{\text{ext}}(r)$ can not be constant between r_{j-1} and r_j , thus the definition of $\Delta\tau_v$ should be modified by introducing geometrical or arithmetical averaging:

$$\Delta\tau_{v,1} = \sigma_v^{ext}(r_j)(r_j - r_{j-1}) , \quad \Delta\tau_{v,2} = \sigma_v^{ext}(r_{j-1})(r_j - r_{j-1}) , \quad (37)$$

$$\Delta\tau_v = \sqrt{\Delta\tau_{v,1} \times \Delta\tau_{v,2}} \quad \text{or} \quad \frac{1}{2}(\Delta\tau_{v,1} + \Delta\tau_{v,2}) . \quad (38)$$

Also equations (35) and (36) can be solved twice

$$I_{v,1}^+(r_{j-1}) = [I_v^+(r_j) - S_v(r_{j-1})] e^{-\Delta\tau_v/\mu} + S_v(r_{j-1}) \quad (39)$$

$$I_{v,2}^+(r_{j-1}) = [I_v^+(r_j) - S_v(r_j)] e^{-\Delta\tau_v/\mu} + S_v(r_j) \quad (40)$$

$$I_{v,1}^-(r_{j-1}) = [I_v^-(r_j) - S_v(r_{j-1})] e^{\Delta\tau_v/\mu} + S_v(r_{j-1}) \quad (41)$$

$$I_{v,2}^-(r_{j-1}) = [I_v^-(r_j) - S_v(r_j)] e^{\Delta\tau_v/\mu} + S_v(r_j) \quad (42)$$

to get mean $I_v^+(r_{j-1})$ and $I_v^-(r_{j-1})$ values from the formulae below:

$$I_v^+(r_{j-1}) = \sqrt{I_{v,1}^+(r_{j-1}) \times I_{v,2}^+(r_{j-1})} \quad \text{or} \quad \frac{1}{2} [I_{v,1}^+(r_{j-1}) + I_{v,2}^+(r_{j-1})]$$

$$I_v^-(r_{j-1}) = \sqrt{I_{v,1}^-(r_{j-1}) \times I_{v,2}^-(r_{j-1})} \quad \text{or} \quad \frac{1}{2} [I_{v,1}^-(r_{j-1}) + I_{v,2}^-(r_{j-1})]$$

At each impact parameter p_k and at different radii, the parameter μ in the equations is defined as

$$\bar{\mu} = \frac{x_{j-1} + x_j}{r_{j-1} + r_j} , \quad (43)$$

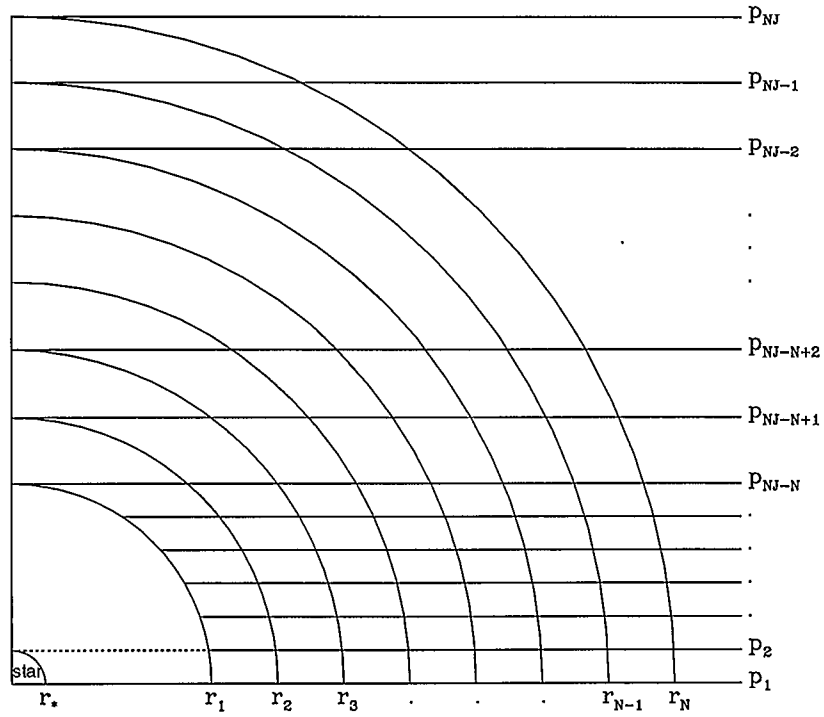


FIGURE 2.1 The (r, p) plane and the grid inside the envelope of AGB star.

$$\begin{aligned}
 x_{j-1} &= \sqrt{r_{j-1}^2 - p_k^2} \\
 x_j &= \sqrt{r_j^2 - p_k^2} .
 \end{aligned}
 \tag{44}$$

In principle, if the specific intensity at the outer radius is known, using the equations (37), (38) and (43) and the recursive equations (39) through (42), the specific intensity at any radius at each impact parameter p_k can be obtained. At the outer radius of the envelope L_v is assumed to be the 3 K background blackbody radiation B_v . Thus at each radius r_j , the zeroth moment $J(v)$, the Eddington flux $H(v)$, and the second moment $K(v)$ of the radiation field can be calculated from the equations (26), (29) and (30) by using the Gaussian numerical integration method. If at any radius, we have already got radiative flux $H(v)$, we can calculate the flux mean extinction efficiency Q_F :

$$Q_F = \frac{\int_0^\infty Q(v) F(v) dv}{\int_0^\infty F(v) dv} = \frac{\int_0^\infty Q(v) H(v) dv}{\int_0^\infty H(v) dv} ,
 \tag{45}$$

which is necessary for the calculation of radiation pressure on dust grains.

Since we have all the parameters of the radiation field, we are ready to solve the hydrodynamic equations (1), (5'), (6) and (8') coupled with the equation (9) which describes the conservation of energy for the radiation field. The following section describes the numerical method for solving the hydrodynamics.

2.4.2 Henyey Method--Numerical Method for Hydrodynamics

The Henyey method (Henyey et al. 1964) is very practical, especially for solving boundary-value problems where the conditions are given at both ends of the interval. A

trial solution for the whole interval is gradually improved upon in consecutive iterations until the required degree of accuracy is reached. In each iteration, corrections to all variables at all points are evaluated in such a way that the effect of each of them on the whole solution including the boundaries is taken into account. The following is an introduction about the principles of the Henyey method.

Let us write the five differential equations (2), (5'), (6), (8') and (9) briefly as:

$$\frac{dy_i}{dm} = f_i(y_1, y_2, y_3, y_4, y_5) \quad , \quad i = 1, 2, 3, 4, 5, \quad (46)$$

where we have used the abbreviations as $y_1 = u$, $y_2 = \lg\rho$, $y_3 = \lg n_d$, $y_4 = w$, $y_5 = 4\pi r^2 H$; m can be any variables (here it is the radius). The next step is discretization, i.e. we proceed from the differential equations (46) to corresponding difference equations for a finite variable interval $[m^j, m^{j+1}]$; here the upper index j denotes the grids along variable m . The functions f_i on the right-hand sides of equations (46) have to be taken for some average arguments which we call $y_i^{j+1/2}$, a combination of y_i^j and y_i^{j+1} ; for example the arithmetic or geometric mean. If the $\Delta m = m^{j+1} - m^j$ is small enough, we can take the differential as:

$$\frac{\partial y_i}{\partial m} = \frac{y_i^j - y_i^{j+1}}{m^j - m^{j+1}},$$

then the equations (46) can be rearranged as:

$$\frac{y_i^j - y_i^{j+1}}{m^j - m^{j+1}} - f_i(y_1^{j+\frac{1}{2}}, y_2^{j+\frac{1}{2}}, y_3^{j+\frac{1}{2}}, y_4^{j+\frac{1}{2}}, y_5^{j+\frac{1}{2}}) = 0. \quad (47)$$

If we define the left-hand sides of (47) as

$$G(i)^j = \frac{y_i^j - y_i^{j+1}}{m^j - m^{j+1}} - f_i(y_1^{j+\frac{1}{2}}, y_2^{j+\frac{1}{2}}, y_3^{j+\frac{1}{2}}, y_4^{j+\frac{1}{2}}, y_5^{j+\frac{1}{2}}) , \quad (48)$$

then equations (47) can be replaced by

$$G(i)^j = 0 . \quad (49)$$

Suppose that we are looking for the solution for values of y_i^j , and we have a first approximation set of values to this solution $y_{i,1}^j$. Since $y_{i,1}^j$ are only approximate, they might not fulfil equations (49), but instead we will have $G(i)_1^j \neq 0$.

Let us now look for small corrections δy_i^j such that the second approximations:

$$y_{i,2}^j = y_{i,1}^j + \delta y_i^j \quad (50)$$

will fulfill equations (49). These δy_i^j will produce the changes $\delta G(i)^j$ as $G(i)_2^j = G(i)_1^j + \delta G(i)^j$, and equations (49) will be changed to:

$$G(i)_2^j = 0 \quad (51)$$

or

$$\delta G(i)^j = -G(i)_1^j . \quad (52)$$

For small enough corrections δy_i^j , we may expand the $\delta G(i)^j$ in terms of increasing powers of the corrections δy_i^j , and keep only the linear terms in the expansion. For example:

$$\begin{aligned} \delta G(i)^j = & \frac{\partial G(i)^j}{\partial y_1^j} \delta y_1^j + \dots + \frac{\partial G(i)^j}{\partial y_5^j} \delta y_5^j + \\ & \frac{\partial G(i)^j}{\partial y_1^{j+1}} \delta y_1^{j+1} + \dots + \frac{\partial G(i)^j}{\partial y_5^{j+1}} \delta y_5^{j+1} . \end{aligned} \quad (53)$$

We can rewrite equations (52) into matrix form as

$$(H) \times \begin{pmatrix} \delta y_1^j \\ \cdot \\ \cdot \\ \delta y_5^j \\ \delta y_1^{j+1} \\ \cdot \\ \cdot \\ \delta y_5^{j+1} \end{pmatrix} = - \begin{pmatrix} G(1)_1^j \\ G(2)_1^j \\ G(3)_1^j \\ G(4)_1^j \\ G(5)_1^j \end{pmatrix}, \quad (54)$$

where the coefficient matrix H is called Henyey Matrix; its elements are the derivatives on the right-hand sides of equations (53) as below

$$(H) = \begin{pmatrix} \frac{\partial G(1)^j}{\partial y_1^j} & \dots & \frac{\partial G(1)^j}{\partial y_5^j} & \frac{\partial G(1)^j}{\partial y_1^{j+1}} & \dots & \frac{\partial G(1)^j}{\partial y_5^{j+1}} \\ \frac{\partial G(2)^j}{\partial y_1^j} & \dots & \frac{\partial G(2)^j}{\partial y_5^j} & \frac{\partial G(2)^j}{\partial y_1^{j+1}} & \dots & \frac{\partial G(2)^j}{\partial y_5^{j+1}} \\ \frac{\partial G(3)^j}{\partial y_1^j} & \dots & \frac{\partial G(3)^j}{\partial y_5^j} & \frac{\partial G(3)^j}{\partial y_1^{j+1}} & \dots & \frac{\partial G(3)^j}{\partial y_5^{j+1}} \\ \frac{\partial G(4)^j}{\partial y_1^j} & \dots & \frac{\partial G(4)^j}{\partial y_5^j} & \frac{\partial G(4)^j}{\partial y_1^{j+1}} & \dots & \frac{\partial G(4)^j}{\partial y_5^{j+1}} \\ \frac{\partial G(5)^j}{\partial y_1^j} & \dots & \frac{\partial G(5)^j}{\partial y_5^j} & \frac{\partial G(5)^j}{\partial y_1^{j+1}} & \dots & \frac{\partial G(5)^j}{\partial y_5^{j+1}} \end{pmatrix}. \quad (55)$$

In our model calculation, the G(i) expressions are the left-hand sides of equations (2), (5'), (6), (8') and (9)

$$G(1) = \frac{\partial u}{\partial t} + u \frac{\partial u}{\partial r} + \frac{1}{\rho} \frac{\partial (P+Q)}{\partial r} + \frac{GM_*}{r^2} + n_d(u-w) \beta ,$$

$$G(2) = \frac{\partial l g \rho}{\partial t} + \frac{3 l g e}{\rho} \frac{\partial (\rho u r^2)}{\partial r^3} ,$$

$$G(3) = \frac{\partial w}{\partial t} + w \frac{\partial w}{\partial r} - \frac{Q_F \pi a^2 L_*}{4 \pi r^2 c m_d} + \frac{GM_*}{r^2} + \frac{\rho}{m_d} (w - u) \beta ,$$

$$G(4) = \frac{\partial l g n_d}{\partial t} + \frac{3 l g e}{\rho} \frac{\partial (n_d w r^2)}{\partial r^3} ;$$

$$G(5) = \frac{\partial (4 \pi r^2 H)}{\partial r^3} .$$

If we know (or assume) the boundary conditions, we take $\delta y_i^1 = 0$ at boundary. Solving matrix equation (54) we are able to get δy_i^2 and then δy_i^3 and so on to get δy_i^j . Then we use equations (50) to get $y_{i,2}^j$ at any variable point m^j . If these $y_{i,2}^j$ do not fulfil the equations (49) yet or do not meet the required accuracy we need to do a second iteration to calculate the new corrections by the same procedure to obtain the third approximation:

$$y_{i,3}^j = y_{i,2}^j + \delta y_i^j , \quad (56)$$

and so on. In these consecutive iterations of this type, the approximate solution can be improved until either the absolute values of all corrections δy_i^j or the absolute values of the right-hand sides in equations (52), drop below a chosen limit. Then we have approached the solution with the required accuracy. If we adopt $m = r$, we are going to have all the values of parameters for all the points from inner radius to outer radius at time t . Using these parameters, we can solve the detailed radiative transfer problem to get

the new radiation field. In a time sequence, one can now apply this radiation field and parameters at time t to the time $t + \Delta t$ and repeat the above process to get all the parameters and radiation field at any radius and at any time. Here we define the time step Δt by requiring that the difference of values of J , H , K are less than 1% in two consecutive times.

2.4.3 A Simple Way to Find J and H

If at each time step, one has to solve the detailed radiative transfer problem, it will be really time consuming. Therefore a simplified solution of the radiative transfer problem has been proposed by Yorke (1980) instead of detailed radiative transfer. Thus we need not solve the detailed radiative transfer problem at each time step (in our calculations, we solve the detailed radiative transfer problem each ten time steps).

If we multiply both sides of equation (21) by μ , we get

$$\frac{1}{c} \mu \frac{\partial I_\nu}{\partial t} + \mu^2 \frac{\partial I_\nu}{\partial r} + \frac{1 - \mu^2}{r} \mu \frac{\partial I_\nu}{\partial \mu} = -\sigma_\nu^{ext} \mu I_\nu + \mu j_\nu . \quad (57)$$

Integrating the above equation over μ and using the definition for $K(\nu) = 1/2 \int_{-1}^1 I_\nu \mu^2 d\mu$,

$H(\nu) = 1/2 \int_{-1}^1 I_\nu \mu d\mu$, $J(\nu) = 1/2 \int_{-1}^1 I_\nu d\mu$, equation (57) becomes:

$$\frac{1}{c} \frac{\partial H_\nu}{\partial t} + \frac{\partial K_\nu}{\partial r} + \frac{3K_\nu - J_\nu}{r} = -\sigma_\nu^{ext} H_\nu . \quad (58)$$

For steady outflows $\partial/\partial t = 0$, so equation (58) can be written as

$$\frac{\partial K_{\nu}}{\partial r} + \frac{3K_{\nu} - J_{\nu}}{r} = -\sigma_{\nu}^{ext} H_{\nu} . \quad (59)$$

By integrating equation (59) over frequency ν , we obtain the frequency independent moment equation as:

$$\frac{\partial K}{\partial r} + \frac{3K - J}{r} + \sigma_H H = 0 , \quad (60)$$

where $\sigma_H = \int_0^{\infty} \sigma_{\nu}^{ext} H_{\nu} d\nu / \int_0^{\infty} H_{\nu} d\nu$ is the flux-mean extinction coefficient. By definition of Eddington factor $f = K/J$, the following equation is obtained

$$\frac{\partial (fJ)}{\partial r} + \frac{3f - 1}{r} J + \sigma_H H = 0 . \quad (61)$$

With the definition of an integrating factor:

$$g(r) = e^{\int r \left(3 - \frac{1}{f(r)} \right) / r' dr'} , \quad (62)$$

equation (61) is simplified to

$$\frac{\partial}{\partial r} [g(r) fJ] + g(r) \sigma_H H = 0 . \quad (63)$$

Assuming a linear functionality of $f(r)$ between r_{j-1} and r_j , equation (63) can be integrated as

$$J(r_{j-1}) = \frac{1}{g_j^{(1)}} J(r_j) - \frac{r_{j-1}^{\alpha-3}}{f_{j-1}^{\alpha+1}} \int_{r_j}^{r_{j-1}} h(r) r^3 \left(\frac{f(r)}{r} \right)^{\alpha} dr , \quad (64)$$

where

$$\alpha = \frac{r_j - r_{j-1}}{r_j f_{j-1} - r_{j-1} f_j} , \quad f_j \equiv f(r_j) ,$$

$$h(r) = \int_0^\infty \sigma_v^{ext} H(v, r) dv = \sigma_H(r) H(r) ,$$

$$g_j^{(1)} = \left(\frac{r_j}{r_{j-1}} \right)^{\alpha-3} \left(\frac{f_{j-1}}{f_j} \right)^{\alpha+1} .$$

If we know $J(r_N)$ (from the outer boundary condition), and for each radius $H(r_j)$ and $f(r_j)$ which are calculated from a previous time step, we know $h(r_j)$ via the above definition of $h(r)$; then assuming a linear behaviour of $h(r)$ between r_{j-1} and r_j , we can find $J(r_j)$ recursively from equation (64).

From the above assumption that $f(r)$ is a linear function of r between r_{j-1} and r_j , we can perform the integration of $g(r)$ as:

$$g(r) = \left(\frac{r}{r_{j-1}} \right)^3 \left(\frac{r_{j-1}}{r} \right)^{\alpha} \left[\frac{r(f_j - f_{j-1}) + r_j f_{j-1} - r_{j-1} f_j}{r_j f_{j-1} - r_{j-1} f_j} \right]^\alpha , \quad (65)$$

so $g(r)$ at radii r_j and r_{j-1} are

$$g(r_{j-1}) = 1 , \quad g(r_j) = \frac{f_{j-1}}{f_j g_j^{(1)}} .$$

Through equation (63), we can get a new $H(r_j)$

$$H(r_j) = -\frac{1}{g \sigma_H} \frac{\partial}{\partial r} [g(r) f J] = \frac{1}{\Delta \tau} \left(\sqrt{g_j^{(1)}} J_{j-1} - \frac{1}{\sqrt{g_j^{(1)}}} J_j \right) (f_j f_{j-1})^{\frac{1}{2}} , \quad (66)$$

where

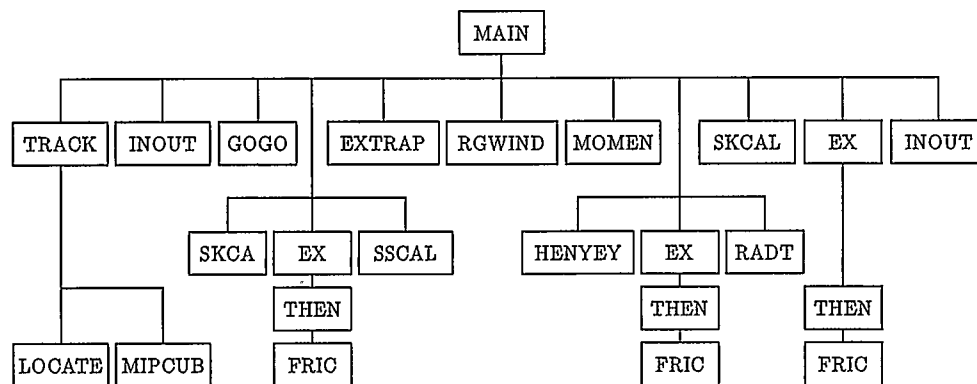
$$\bar{g} = \sqrt{g(r_j) g(r_{j-1})} = \sqrt{g(r_j)} \quad , \quad \Delta\tau = \sqrt{\sigma_H(r_j) \sigma_H(r_{j-1})} (r_j - r_{j-1}) .$$

We can apply these new $J(r)$ and $H(r)$ to equation (17) of dust radiative equilibrium and the hydrodynamic equations to calculate the new T_d , T_g , n_d , ρ , u and w .

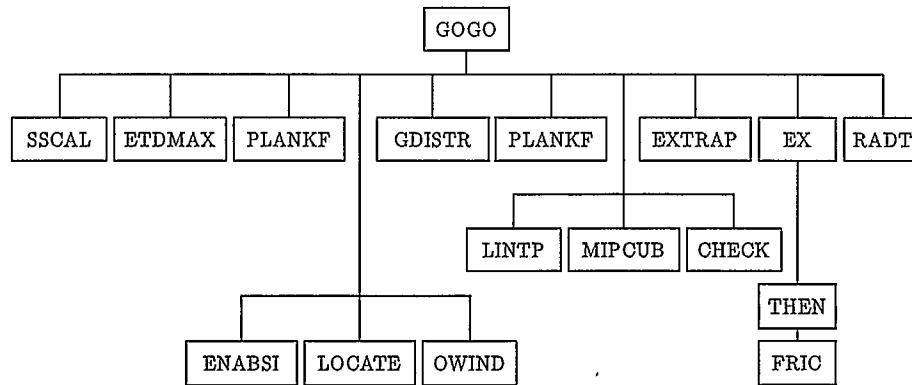
2.4.4 Structure for the Program

Here are the structures of the program, which includes four components: the structures of the main program, the initial and boundary conditions, the hydrodynamics, and the radiative transfer.

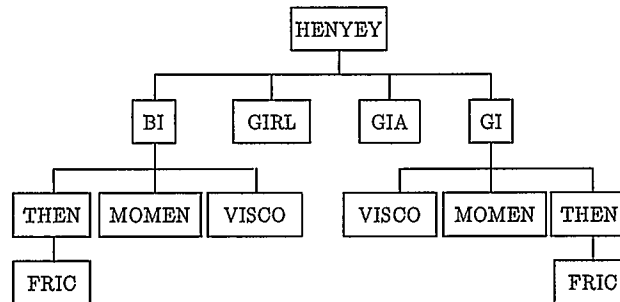
The structure for the main program:



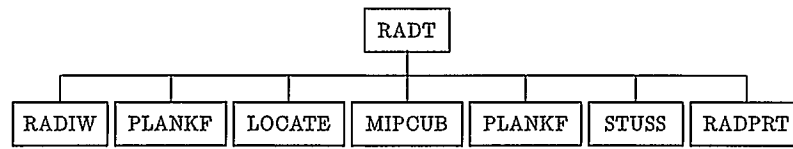
The structure for the initial and boundary conditions:



The structure for hydrodynamics:



The structure for radiative transfer:



Chapter 3. Exploring Effects of Parameters

The parameters such as dust condensation temperature T_{cond} , mass loss rate \dot{M} , dust size a , dust to gas ratio Φ , and dust optical properties are very important to our model calculations, any changes to these parameters affect the model results tremendously. However, there exist considerable uncertainties in these parameters. It is necessary to investigate them before doing any model calculations. In this chapter, we are going to investigate the dust condensation temperature, the range of dust to gas ratio, the effects of dust size, the dust optical properties and the effects of mass loss rate.

3.1 Dust Condensation Temperature

As mentioned in chapter 1, infrared observations (Merrill 1977) have shown that dust condenses in the outflows from late-type giants. O-rich giants are observed to form silicate materials, while C-rich ones form SiC and amorphous carbon and graphite. This newly formed dust plays an important role in driving the mass loss from giants (Kwok 1975, Tielens 1983, Netzser and Elitzur 1993, Habing et al. 1994). Indeed, the momentum that the grains acquire from the stellar radiation field and transfer to the gas inferred from IR observations is comparable to that required to drive the observed gaseous mass loss (Knapp 1986). Over the last decade considerable efforts have been devoted to understanding the formation of circumstellar dust and its influence on red giant envelopes (Salpeter 1977, Gail et al. 1987, Tielens 1989). Several independent observational clues strongly suggest that dust is only formed in a stationary layer above the stellar photosphere (Tielens 1989).

Since the shock tube experiments of Gilman (1969) and Friedemann (1969), many attempts have been made to understand the dust condensation temperature which ranges from 500 K to 2000 K for different kinds of dust grains. Gilman (1969) and Friedemann (1969) suggest that SiC would be an early condensate for both Si and C which have high abundances in evolved stellar atmospheres. Their shock tube experiments showed that silicon carbide particles (SiC) nucleate homogeneously and grow rapidly in a temperature range of 1300 K--2000 K. Later, when temperature drops to 1000 K, PAHs (Polycyclic Aromatic Hydrocarbons) begin to form homogeneously from the gas phase, where they can deposit onto the grain and form a sootlike turbostratic structure. Thermodynamic equilibrium calculations for a cooling gas with cosmic composition show that calcium-aluminum silicates are the first to condense out at about 1400 K, while the majority of silicon is expected to condense in the form of magnesium silicates at about 1050 K (Schutte et al. 1989). The small molecular clusters which act as nucleation centers for the dust grains probably cannot survive the high gas temperature and the shocks in the extended pulsating photosphere, dust particles can only start to form in a stationary layer. At this large distance from the star, the temperature will be less than the condensation temperature of silicate materials (Tielens 1983).

Rowan-Robinson & Harris (1982, 1983a, 1983b) suggest that the condensation temperature for dust in oxygen-rich M-type stars can range from 500 K to 1000 K, and for carbon-rich star the condensation occurs mostly at 1000 K by utilizing the method by fits of model calculations of radiative transfer in the dust shells to the observed spectra for 153 objects. Volk & Kwok (1987) are able to fit the strength of 10 μm silicate feature

for 467 objects. They obtain the maximum color temperature (the temperature of the blackbody of which the radiation is used to match the observed fluxes) in the sample of 1700 K with the exception of three stars and suggest that the dust condensation temperature is around 1700 K. Gauge, Gail & Sedlmayr (1990) modelled the nucleation of dust grain in stellar atmospheres using the classical nucleation theory, and suggest that the condensation temperature is about 1200 K to 1600 K for carbon-rich dust. From the chemical point of view for oxygen rich star, it is expected that the dust in circumstellar shells condenses in the expanding and cooling gas of stellar wind at a temperature below 1000 K (Beck et al. 1992).

From above, the estimate range of condensation temperature is from 500 K to 1700 K. In our calculations except for comparison to Netzer & Elitzur's results by using $T_{\text{cond}} = 850$ K (in section 3.3), we use $T_{\text{cond}} = 1000$ K, and assume that the dust formation as a sudden process and that the grains immediately have their final size. Actually the dust grain formation is probably an episodic event coupled to the stellar pulsation and influencing the dynamics. As grains travel through the gas, collisions between the grains and gas will cause some of the atoms to be absorbed onto the grain surface; as the result the grains will grow in size. On the other hand, when the drift velocity is very large with respect to the gas, the kinetic energy of the gas may exceed the surface potential energy of the grain, and atoms may be knocked out from the grain; the grain will be sputtered (Kwok 1975). We ignore all these details for we are interested in the effects at large distances and assume that averaging the events over a pulsation cycle will not seriously affect the outflow at large distance.

3.2 Dust Optical Properties--Mie Theory

The dust optical opacity is an essential ingredient that enters the equations as described in chapter 2. The dust optical properties depend on the chemical composition of particles, their size, shape, orientation, the surrounding medium, the number of particles, the polarization state and the frequency of incident radiation. When the dust consists of silicates in the case of oxygen-rich stars, the optical properties are dominated by the absorption (or emission) peaks at $\lambda = 9.7 \mu\text{m}$ and $\lambda = 18 \mu\text{m}$. In the case of carbon-rich stars, the optical opacity decreases monotonically as a function of wavelength over most of the infrared range. The relative abundance of heavy elements determines the amount of mass in grains, and the grain size determines their numbers.

If we assume that the dust grains are of spherical shape, from Mie theory (Bohren & Huflman 1983) the scattering and extinction cross sections are:

$$\sigma_{sca} = \frac{2\pi}{k^2} \sum_{n=1}^{\infty} (2n+1) (|a_n|^2 + |b_n|^2) \quad (67)$$

$$\sigma_{ext} = \frac{2\pi}{k^2} \sum_{n=1}^{\infty} (2n+1) \text{Re}(a_n + b_n) \quad (68)$$

where $\text{Re}(a_n + b_n)$ means the real part of $a_n + b_n$, $k = 2\pi/\lambda$,

$$a_n = \frac{m\psi_n(mx) \psi_n'(x) - \psi_n(x) \psi_n'(mx)}{m\psi_n(mx) \xi_n'(x) - \xi_n(x) \psi_n'(mx)} \quad (69a)$$

$$b_n = \frac{\psi_n(mx) \psi_n'(x) - m\psi_n(x) \psi_n'(mx)}{\psi_n(mx) \xi_n'(x) - m\xi_n(x) \psi_n'(mx)} \quad (69b)$$

$x = ka = 2\pi a/\lambda$, a is the radius of dust particle, $m = N_1/N$ is the refractive index of the particle relative to the medium, N_1 , N are the refractive indices of particle and medium respectively, $N = n + iK$, and n , K are optical constants: $n = c/v$ (v is the speed of light through the medium), $K = \omega(\epsilon\mu)^{1/2}$, here ϵ , μ are electric permittivity and magnetic permeability respectively; $\psi_n(x) = xj_n(x)$, $\xi_n(x) = xh_n^{(1)}(x) = x(j_n(x) + iy_n(x))$ with $j_n(x) = (\pi/2x)^{1/2}J_{n+1/2}(x)$ and $y_n(x) = (\pi/2x)^{1/2}Y_{n+1/2}(x)$, as $J_{n+1/2}(x)$ and $Y_{n+1/2}(x)$ are Bessel functions of the first and second kinds.

The efficiencies for extinction, scattering and absorption are defined as:

$$Q_{ext} = \frac{\sigma_{ext}}{\pi a^2}, \quad Q_{sca} = \frac{\sigma_{sca}}{\pi a^2}, \quad Q_{abs} = \frac{\sigma_{abs}}{\pi a^2}, \quad \text{and} \quad \sigma_{abs} = \sigma_{ext} - \sigma_{sca}.$$

If the dust particles are small compared with wavelength, we can expand the various functions in the scattering and extinction coefficients a_n and b_n in power series and retain only first few terms; the extinction, scattering and absorption efficiencies are going to be

$$Q_{ext} = 4x \operatorname{Im} \left\{ \frac{m^2 - 1}{m^2 + 2} \left[1 + \frac{x^2}{15} \left(\frac{m^2 - 1}{m^2 + 2} \right) \frac{m^4 + 27m^2 + 38}{2m^2 + 3} \right] \right\}, \quad (70)$$

$$Q_{sca} = \frac{8}{3} x^4 \left| \frac{m^2 - 1}{m^2 + 2} \right|^2, \quad (71)$$

$$Q_{abs} = 4x \operatorname{Im} \left\{ \frac{m^2 - 1}{m^2 + 2} \right\} \left[1 + 4 \frac{x^3}{3} \operatorname{Im} \left\{ \frac{m^2 - 1}{m^2 + 2} \right\} \right]. \quad (72)$$

If x is sufficiently small, $(4x^3/3)\operatorname{Im}\{(m^2 - 1)/(m^2 + 2)\} \rightarrow 0$, and then the absorption efficiency is approximately

$$Q_{abs} = 4xIm\left\{\frac{m^2 - 1}{m^2 + 2}\right\}. \quad (73)$$

Therefore, $Q_{abs} \propto x$, the absorption cross section $\sigma_{abs} = \pi a^2 Q_{abs}$ is proportional to the volume of the particle.

If $(m^2 - 1)/(m^2 + 2)$ is a weak function of wavelength over some interval, then for sufficiently small particles $Q_{abs} \propto 1/\lambda$, $Q_{sca} \propto 1/\lambda^4$. If extinction is dominated by absorption, the extinction spectrum will vary as $1/\lambda$; if the extinction is dominated by scattering, the extinction spectrum will vary as $1/\lambda^4$. In either case, and in the intermediate cases as well, shorter wavelengths are extinguished more than longer wavelengths.

The opacity is given by

$$\chi(\lambda) = \frac{1}{\rho_i} \int Q_\lambda(a) \pi a^2 n(a) da, \quad (74)$$

where the size distribution function $n(a)$ is the number density of dust particles per unit grain radius, ρ_i is internal density of dust particle.

When the dust size is very large, the extinction efficiency approaches 2 (Draine & Lee 1984).

3.3 Dust Grain Sizes

There exists considerable uncertainty regarding the sizes of grains in the expanding shells. Papoular & Pegourie (1983) find that these grains might be larger than interstellar grains (0.3 μm) and Snow et al. (1987) suggest that they are not smaller than 0.05 μm and could be as large as 0.3 μm . Netzer & Elitzur (1993) suggest that optical properties

of dust are independent of the grain size for small dust grains and that the larger grains (0.3-1.0 μm) seem impossible. Our results enable us to find the effects of the dust size by utilizing the compilation by Loar & Draine (1993) for optical properties of astronomical silicates and graphite.

Figure 3.1 displays the terminal velocity distributions of the gas and dust along with their difference, the drift velocity, as a function of grain size for oxygen-rich and carbon-rich stars. The parameters used here are $M_* = 3.0 M_\odot$, $L_* = 5 \times 10^4 L_\odot$, $T_{\text{eff}} = 2500 \text{ K}$, $\Phi_0 = 5 \times 10^{-3}$, $\dot{M} = 10^{-5} M_\odot/\text{yr}$ for oxygen-rich stars and $M_* = 3.0 M_\odot$, $L_* = 5.6 \times 10^4 L_\odot$, $T_{\text{eff}} = 2000 \text{ K}$, $\Phi_0 = 1.5 \times 10^{-3}$, $\dot{M} = 10^{-5} M_\odot/\text{yr}$ for carbon-rich stars (the condensation temperature $T_{\text{cond}} = 850 \text{ K}$). Comparing to the typical terminal velocity for gas from observations (10-20 km/s, generally $\leq 30 \text{ km/s}$), the dust size can be anything less than 0.15 μm as shown in Figure 3.1.

Figure 3.1 shows us that when dust size $a \leq 0.05 \mu\text{m}$, the gas velocity decreases a little, the dust velocity increases a little. As the dust size increases from 0.05 μm to 0.3 μm for graphite, and to 0.4 μm for silicate, the gas velocity increases. When the dust size increases further more, the gas velocity drops again. For the dust, when dust size increases from 0.05 μm to 0.4 μm for graphite, and to 0.6 μm for silicate, the dust velocity increases a lot; as the dust size increases further, the dust velocity drops.

The dependence on grain size for gas and dust velocities can be understood when we check the extinction efficiencies in equations (71) and (72) and the forces acting on the dust and gas described on section 2.1 to 2.4. The acceleration of the dust grains are:

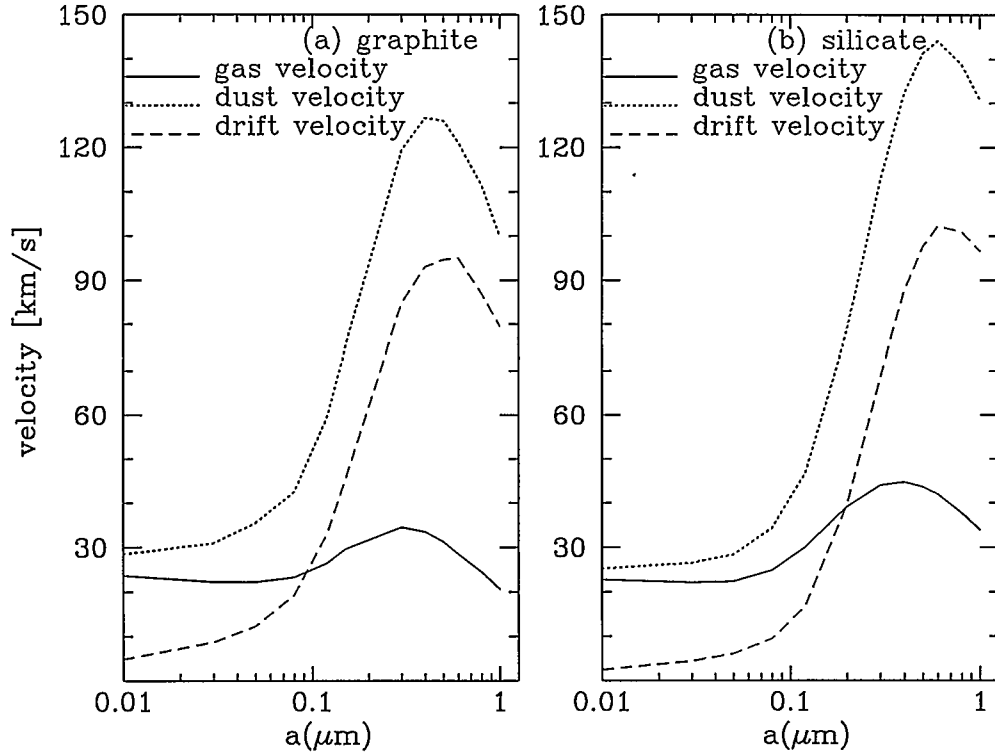


FIGURE 3.1 Terminal gas, dust and drift velocities vs grain size a for (a) carbon stars assuming graphite grains with $\dot{M} = 10^{-5} M_{\odot}/\text{yr}$, $L_{*} = 5.6 \times 10^4 L_{\odot}$, $M_{*} = 3 M_{\odot}$, $\Phi_0 = 1.5 \times 10^{-3}$, $T_{\text{cond}} = 850 \text{ K}$ and $T_{\text{eff}} = 2000 \text{ K}$ and (b) oxygen stars assuming silicate grains with the same M_{*} , \dot{M} , T_{cond} and $L_{*} = 5 \times 10^4 L_{\odot}$, $\Phi_0 = 5 \times 10^{-3}$ and $T_{\text{eff}} = 2500 \text{ K}$.

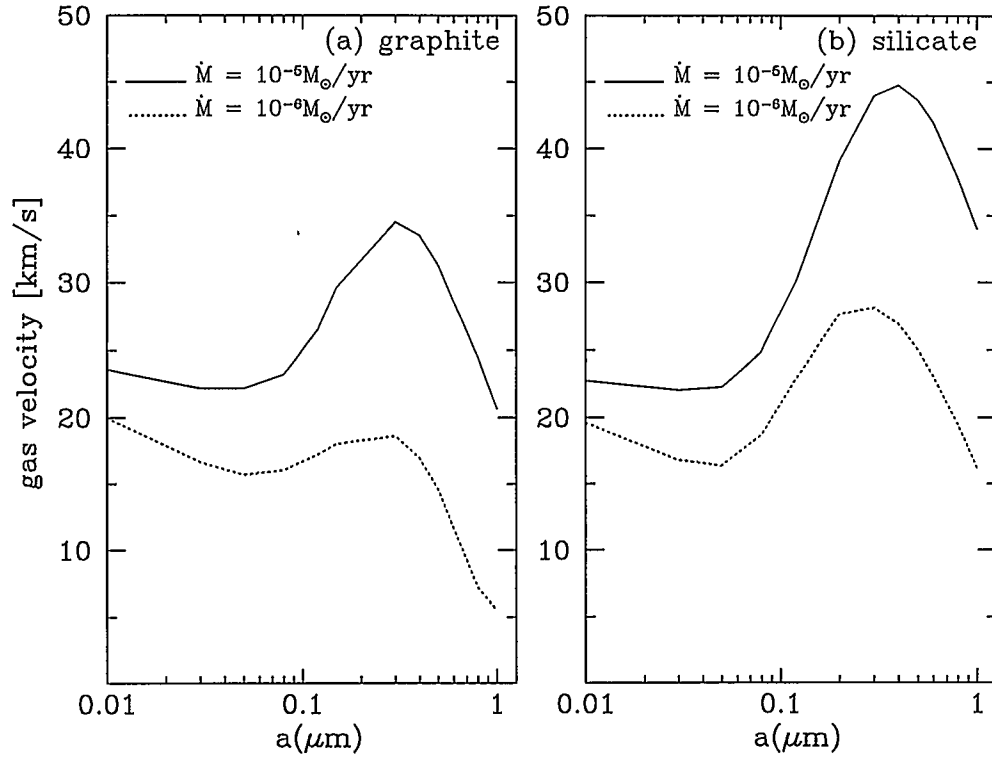


FIGURE 3.2 Terminal gas outflow velocity as function of dust size with different mass loss rate for (a) carbon stars and (b) oxygen stars. The parameters used here are the same as in Figure 3.1 except the mass loss rate as indicated inside the diagram box.

$$a_r = \frac{\pi a^2 Q_F L_*}{4 \pi r^2 m_d c}, \quad a_{dc} = -\frac{\pi a^2}{m_d} \frac{\dot{M}}{4 \pi r^2 u} (w-u) \left[\frac{8kT_g}{\pi \mu m_H} + (u-w)^2 \right]^{\frac{1}{2}},$$

the acceleration of gas are

$$a_{gc} = \frac{\pi a^2}{m_d} \frac{\Phi \dot{M}}{4 \pi r^2 u} (w-u) \left[\frac{8kT_g}{\pi \mu m_H} + (w-u)^2 \right]^{\frac{1}{2}}, \quad a_p = -\frac{1}{\rho} \frac{\partial (P+Q)}{\partial r}.$$

The common term $a_g = -GM_r/r^2$ (the gravitational deceleration) can be ignored as for different dust size it has the same effect. For very small dust size $a \leq 0.05 \mu\text{m}$, by inspecting equations (71) and (72), we can see that Q_{abs} is more important than Q_{sca} , and Q_{ext} is dominated by Q_{abs} , and $Q_{\text{ext}} \propto a$. So the radiation force acting on the dust grain a_r is constant, the drag force on dust from coupling effects a_{dc} and the force on gas from coupling effects a_{gc} are proportional to $1/a$ (for $m_d = 4/3\pi a^3 \rho_i$) and the drift velocity does not increase too much. From these behaviors of a_r , a_{dc} , and a_{gc} , we know that when the dust size increases the dust velocity increases a little and gas velocity decreases a little. This decrease of the gas velocity at small dust size is more obvious when the mass loss rate \dot{M} is small as shown in Figure 3.2, which has the same parameters as in Figure 3.1 except that the $\dot{M} = 10^{-6} M_\odot/\text{yr}$ instead of $10^{-5} M_\odot/\text{yr}$. The smaller the \dot{M} , the higher the drift velocity (see section 3.4). As dust size increases, the extinction from scattering becomes important and the radiation pressure on dust will increase (for $Q_{\text{sca}} \propto a^4$); as in the plots, the drift velocity increases a lot, so the gas velocity will increase as well for the coupling term is a second order function of $(w-u)$.

When the dust size becomes very large, the total extinction efficiency $Q_{\text{ext}} \approx 2.0$, the radiation pressure $a_r \propto 1/a$, so the dust velocity will decrease and the drift velocity will

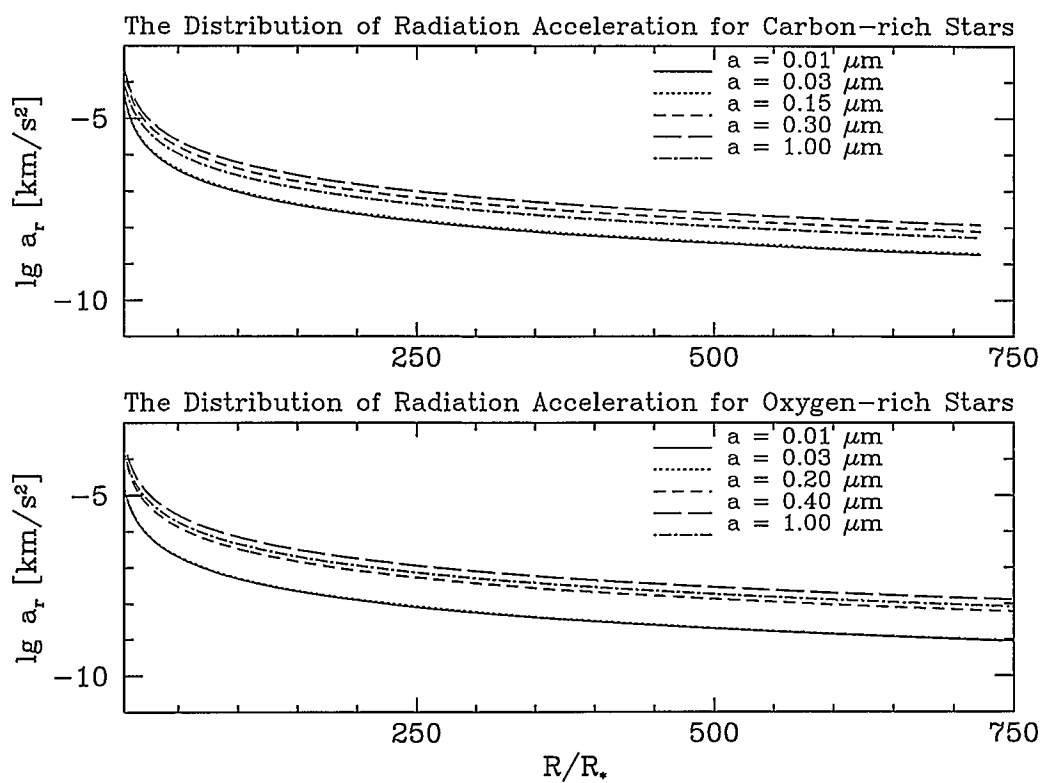


FIGURE 3.3 The distribution of radiation acceleration on dust as the functions of radius with different dust size for oxygen-rich and carbon-rich stars. The parameters used here are the same as in Figure 3.1.

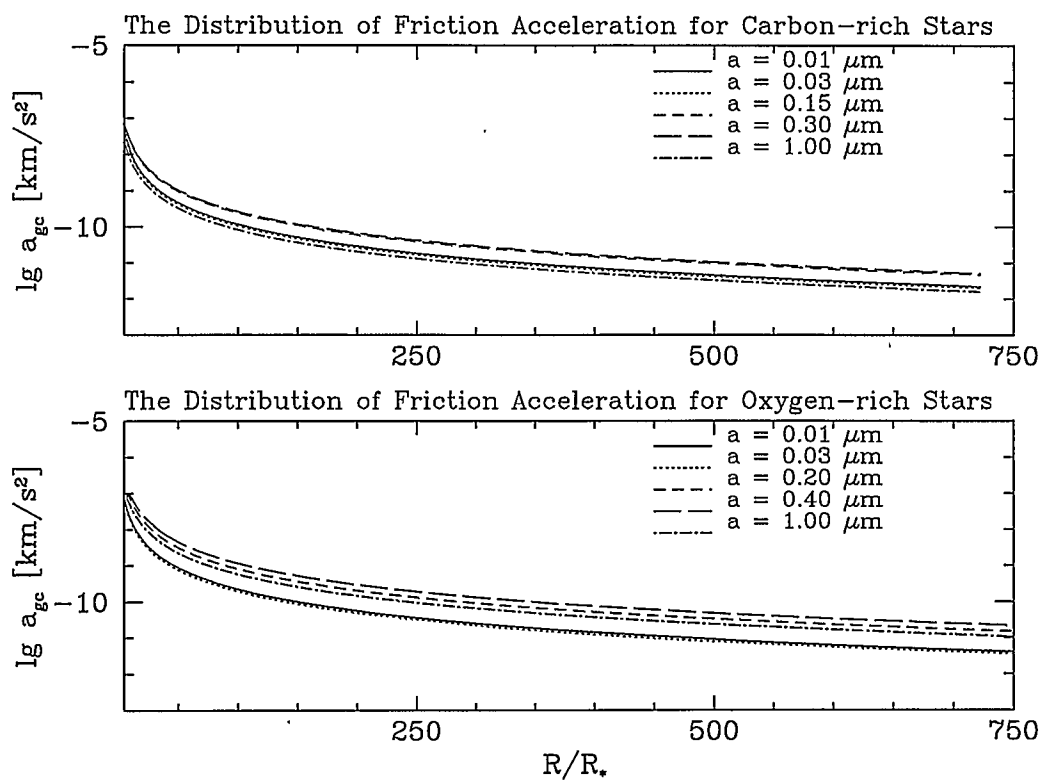


FIGURE 3.4 The distribution of coupling acceleration on gas as the functions of radius with different dust size for carbon-rich and oxygen-rich stars. The parameters used here are the same as in Figure 3.1.

decrease, so will the gas velocity.

The radiation acceleration and the coupling effects are plotted in Figures 3.3 and 3.4 as the function of radius at different dust size. The parameters used here are the same as in Figure 3.1. These plots show that a_r and a_{gc} are the largest when $a = 0.3 \mu\text{m}$ for carbon-rich stars and $a = 0.4 \mu\text{m}$ for oxygen-rich stars; and a_r is the same when a is $0.01 \mu\text{m}$ and $0.03 \mu\text{m}$.

3.4 Mass Loss Rates

As the mass loss rate is changed, the density inside the shell will be changed as indicated in equation (20) and this results in the optical depth, the spectrum distribution and the terminal velocity of the outflow changing as in Figures 3.5, 3.6a, 3.6b and 3.7. The parameters used here are $T_{\text{eff}} = 2500 \text{ K}$, $L_* = 5 \times 10^4 L_{\odot}$, $M_* = 5 M_{\odot}$, $\Phi_0 = 5 \times 10^{-3}$ for oxygen-rich stars and $T_{\text{eff}} = 2000 \text{ K}$, $L_* = 5.6 \times 10^4 L_{\odot}$, $M_* = 5 M_{\odot}$, $\Phi_0 = 1.5 \times 10^{-3}$ for carbon-rich stars and the dust grain size a is $0.05 \mu\text{m}$.

From Figure 3.5, we notice that the optical depth at $\lambda = 10 \mu\text{m}$ always increases as \dot{M} increases. This is because the dust density increases when \dot{M} increases. From Figure 3.6, we know the spectrum peak shifts from short wavelengths to long wavelengths. The feature at $\lambda = 9.7 \mu\text{m}$ is changed from emission to absorption as \dot{M} increases for oxygen-rich stars as in Figure 3.6b. This is because the more dust particles, the more UV photons are absorbed and re-emitted at infrared wavelengths. And as the number of dust particles increased, the optical depth is increased, so the feature at $\lambda = 9.7 \mu\text{m}$ will change from emission to self-absorption.

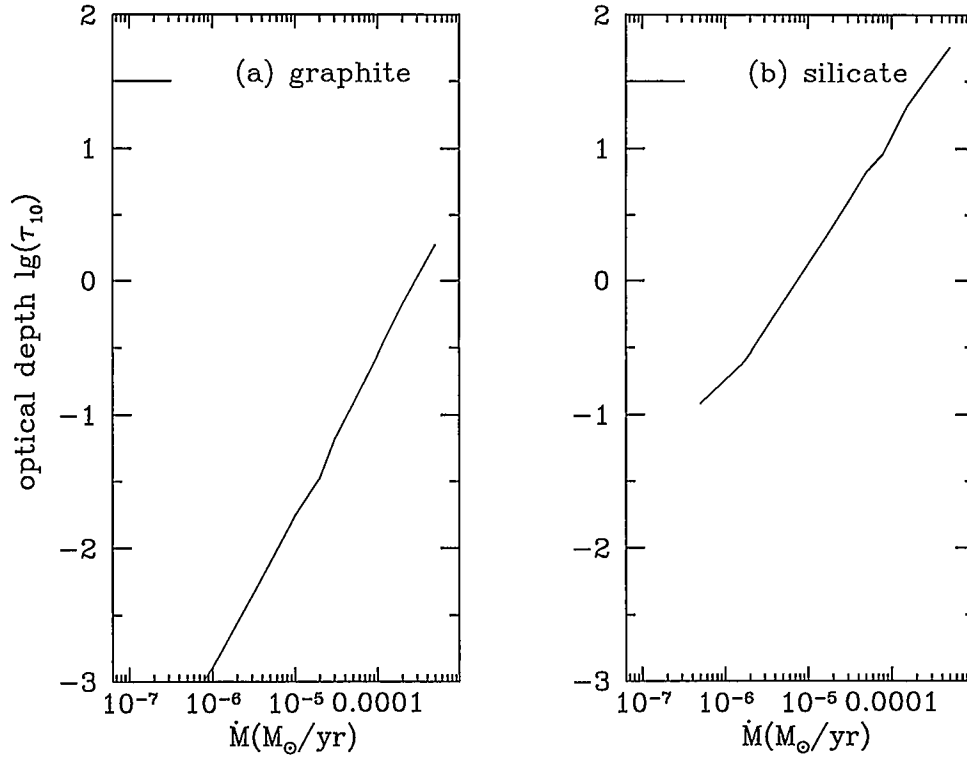


FIGURE 3.5 The optical depth at $\lambda = 10 \mu\text{m}$ as a function of mass loss rate for (a) carbon stars with graphite grains ($a = 0.05 \mu\text{m}$) when $L_* = 5.6 \times 10^4 L_{\odot}$, $M_* = 5 M_{\odot}$, $\Phi_0 = 1.5 \times 10^{-3}$, $T_{\text{cond}} = 1000 \text{ K}$ and $T_{\text{eff}} = 2000 \text{ K}$ and (b) oxygen stars with silicate grains ($a = 0.05 \mu\text{m}$) when $L_* = 5 \times 10^4 L_{\odot}$, $\Phi_0 = 5 \times 10^{-3}$, $T_{\text{eff}} = 2500 \text{ K}$ and the same M_* and T_{cond} .

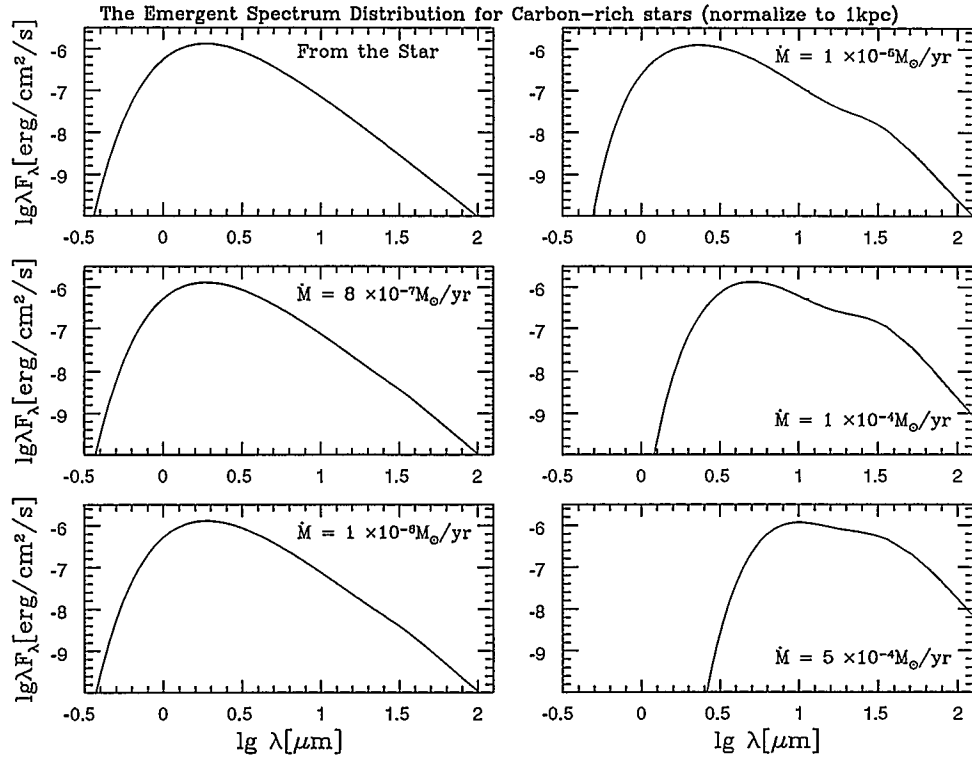


FIGURE 3.6a The emergent spectra for carbon-rich stars with graphite grains at different mass loss rates from 8×10^{-7} to $5 \times 10^{-4} M_\odot/\text{yr}$. The parameters used here are the same as in Figure 3.5.

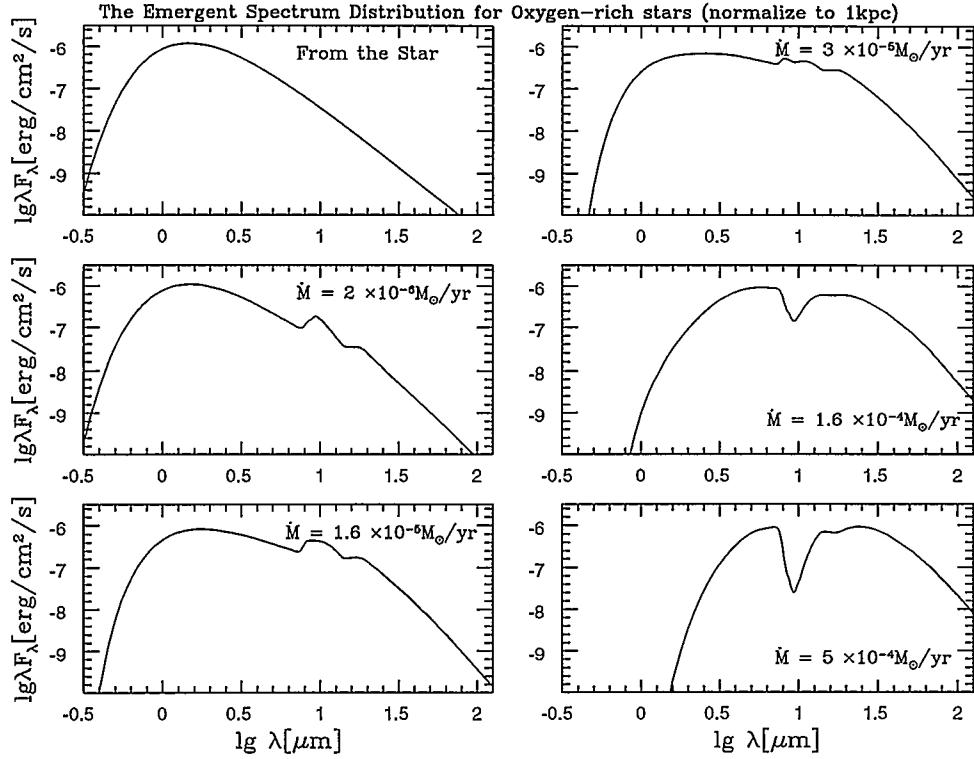


FIGURE 3.6b The emergent spectra for oxygen-rich stars with silicate grains at different mass loss rates from 2×10^{-6} to $5 \times 10^{-4} M_\odot/\text{yr}$. The parameters used here are the same as in Figure 3.5.

In Figure 3.7, it is shown that the terminal velocity increases as \dot{M} increases from several $10^{-7} M_{\odot}/\text{yr}$ to $10^{-5} M_{\odot}/\text{yr}$, and decreases as \dot{M} increases beyond $10^{-5} M_{\odot}/\text{yr}$. The dust velocity always decreases as \dot{M} increases. We can explain the velocity distributions of gas and dust by investigating the forces acting on the dust and gas once more. As shown in section 3.3, acceleration due to the radiation on dust grain in the form of acceleration a_r is proportional to the flux-mean extinction efficiency Q_F . As shown in Figure 3.6, when \dot{M} is increased, the spectrum is shifted from short wavelengths to long wavelengths, and we know from equation (70), Q_{ext} decreases as λ increases. So, when \dot{M} is increased the flux-mean extinction efficiency Q_F will decrease, this will cause the radiation pressure a_r to be decreased as shown in Figure 3.8a. As the result the dust velocity will be decreased.

The pushing force on gas due to the interaction effect from the dust, a_{gc} , as noted in section 3.3, is proportional to \dot{M} . When \dot{M} increases, the gas velocity will increase. But as \dot{M} continues to increase beyond $10^{-5} M_{\odot}/\text{yr}$, the drift velocity decreases (because the dust velocity decreases), and a_{gc} is a second order function of $(w-u)$, so the gas velocity will decrease. Figure 3.8b gives a demonstration of the behavior of a_{gc} . We conclude that it is possible to have a low gas terminal velocity at high mass loss rate for both carbon-rich and oxygen-rich stars.

The results obtained here in Figure 3.7 are different from the those of Netzer and Elitzur (1993) for oxygen-rich stars, where they found that the terminal velocity of oxygen-rich star did not decrease with \dot{M} for high mass loss rate. They explained that the radiation pressure increased with \dot{M} . This is not true as demonstrated in Figure 3.8a. The other

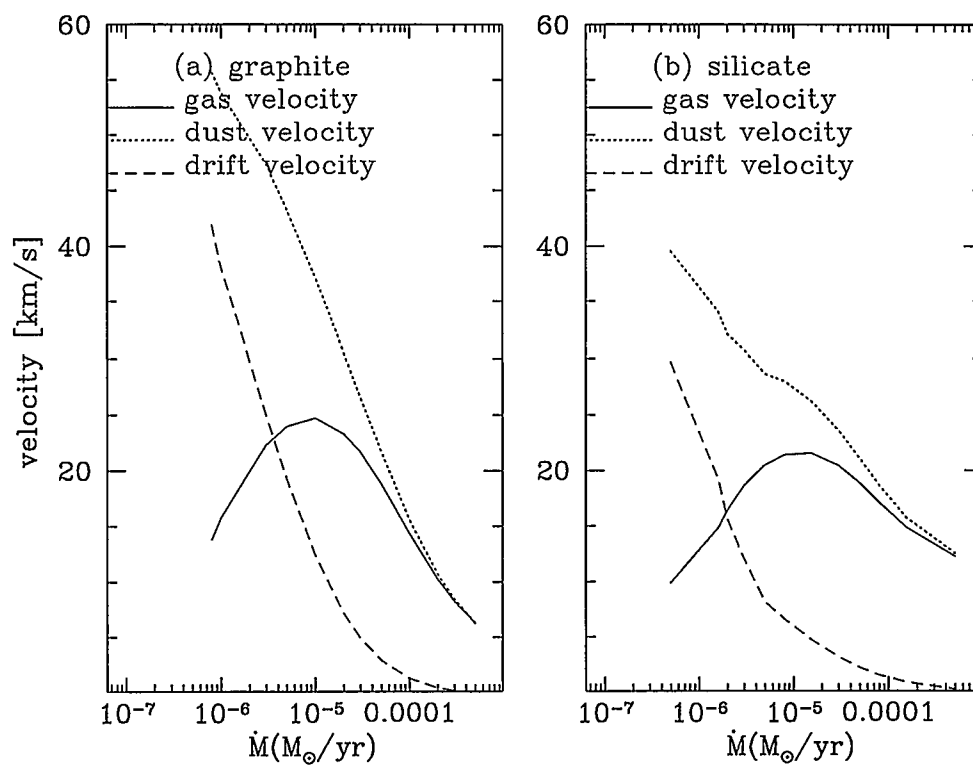


FIGURE 3.7 The terminal outflow gas, dust and drift velocities as functions of mass loss rate for (a) carbon-rich stars with graphite grains and (b) oxygen-rich stars with silicate grains. The parameters used here are the same as in Figure 3.5.

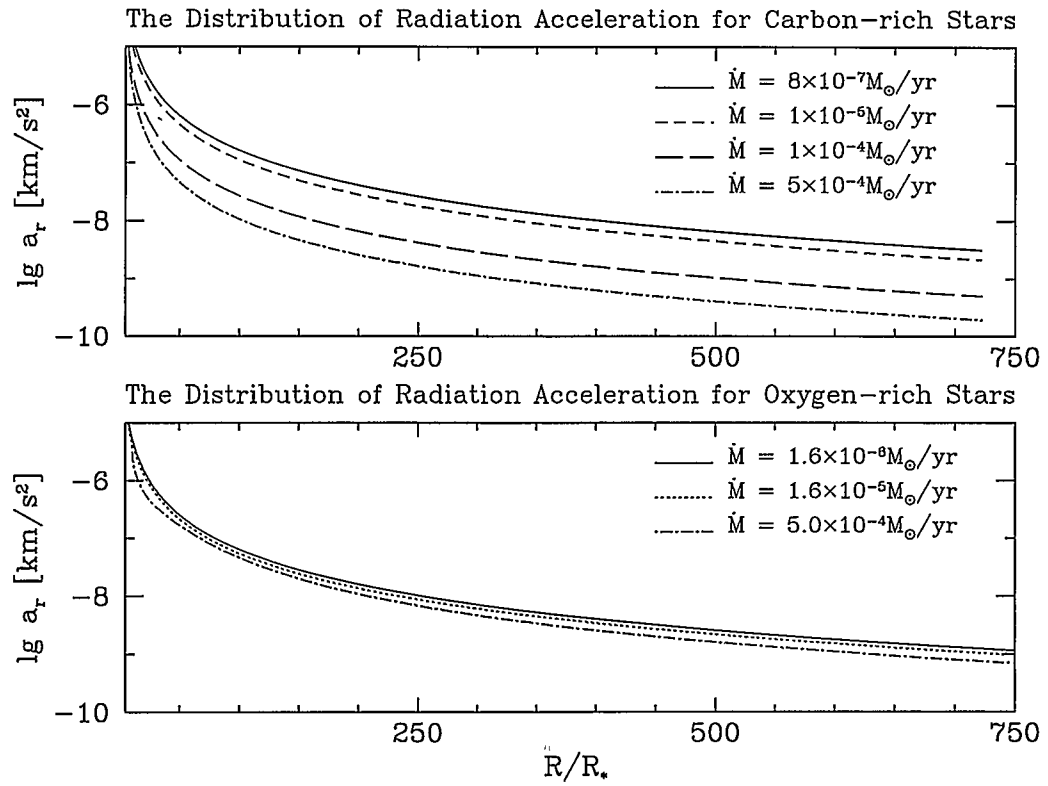


FIGURE 3.8a The distributions of radiation acceleration for different mass loss rates.

The parameters used here are the same as in Figure 3.5.

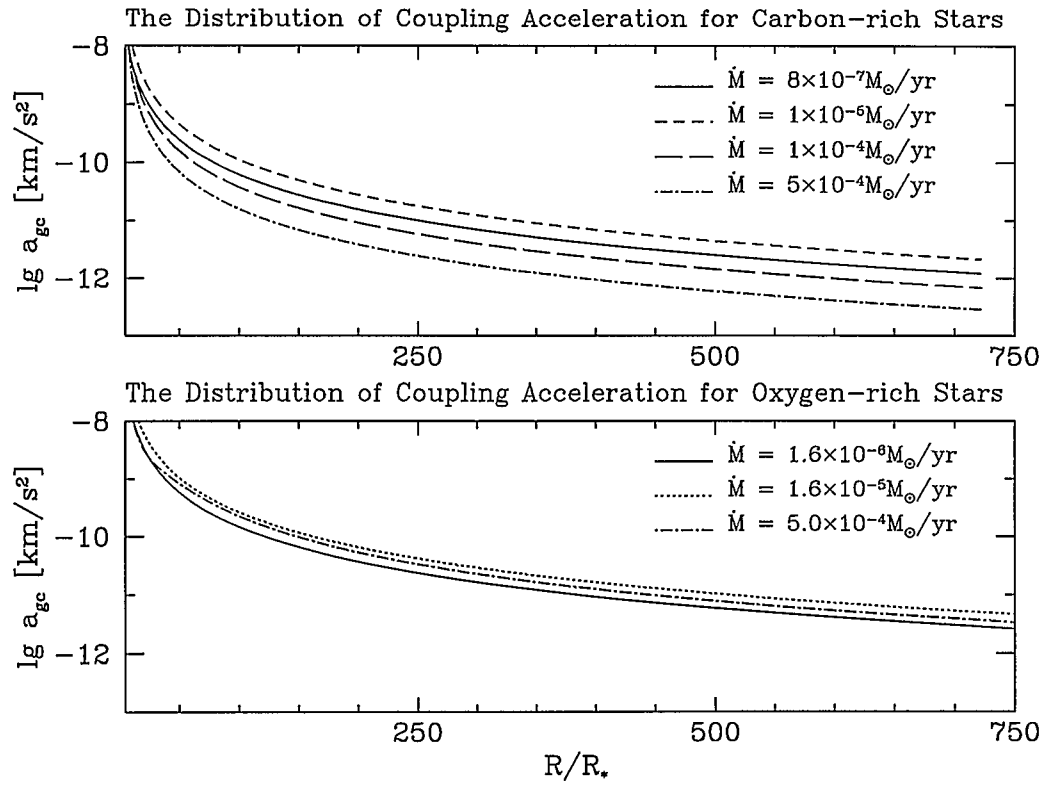


FIGURE 3.8b The distributions of coupling acceleration for different mass loss rates.

The parameters used here are the same as in Figure 3.5.

thing we want to mention here is that on the calculations of Netzer and Elitzur (1993) and Habing et al. (1994) they did not include the effect of gas pressure which is very important for the gas terminal velocity (Steffen & Szczerba et al. 1995).

Since the pushing force a_{gc} is decreasing as \dot{M} is decreasing when \dot{M} is small, as mentioned above, there must be a lower limit on the mass loss rate that can be driven by radiation pressure on dust. Similar mass loss rate limits were obtained by Kwok (1975), Netzer and Elitzur (1993). Table 3.1 lists the results of present work with $\Phi_0 = 5 \times 10^{-3}$ along with the results obtained by Kwok (1975), and Netzur and Elitzur (1993).

TABLE 3.1 The Minimum Mass Loss Rates (in the unit of M_\odot/yr)

M_* (M_\odot)	L_* (L_\odot)	T_{eff} (K)	a (μm)	\dot{M}_{min} (Kwok)	\dot{M}_{min} (N.E.*)	\dot{M}_{min} (This one)
1	10^4	2000	0.15	5.5×10^{-7}	1.5×10^{-7}	2.0×10^{-7}
5	10^5	2000	0.11	1.8×10^{-6}	4.0×10^{-7}	6.5×10^{-7}
5	10^5	3000	0.06	9.8×10^{-7}	2.0×10^{-7}	3.5×10^{-7}
25	10^6	2000	0.08	6.0×10^{-6}	1.5×10^{-6}	2.0×10^{-6}
25	10^6	3000	0.045	3.1×10^{-6}	5.0×10^{-7}	9.0×10^{-7}
25	10^6	5000	0.02	1.6×10^{-6}	1.5×10^{-7}	2.5×10^{-7}

Note: * N.E. is the abbreviation for Netzer and Elitzur.

3.5 Dust to Gas Ratios

A parameter with a very important impact on the solutions is the dust to gas ratio. There exists a considerable uncertainty in this parameter. The expression for dust to gas ratio according to Kwok (1975) can be written as

$$\Phi = \frac{\rho_d}{\rho} = \frac{Ayf}{\mu} \times \frac{u}{w}, \quad (75)$$

where A is the molecular weight of a grain, μ is the mean molecular weight of gas, f is the fraction of grain material condensed, y is the relative abundance of the grain material. If we assume grain material is totally condensed ($f = 1$), we can find the rest ($v_{\text{drift}} = 0$) dust to gas ratio

$$\Phi_0 = \frac{Ay}{\mu}. \quad (76)$$

If we can find the relative abundance of the grain material, we can find the rest dust to gas ratio.

Lambert et al. (1986) determine the CNO relative abundances for carbon stars by using the new model atmospheres to analyze high resolution infrared spectra as in Table 3.2. In the Table, the abundance $[\epsilon] = \log_{10}\epsilon - \log_{10}\epsilon_{\odot}$ and the solar values used here are: $\log_{10}\epsilon(\text{C}) = 8.67$, $\log_{10}\epsilon(\text{O}) = 8.92$, $\log_{10}\epsilon(\text{H}) = 12.0$, and the last column is the dust to gas ratio calculated according to equation (76) with $\mu = 2.3$ and $A = 12$.

From Table 3.2, we notice that the dust to gas ratio for carbon-rich stars can range from 1.4×10^{-4} to 2.1×10^{-3} .

Olosson, Erikson and Gustafsson (1987) have surveyed a sample of bright N-type stars (cool carbon stars) and estimated the dust to gas ratio to be $1/(350 \pm 200)$ by using the simple model of Sopka et al. (1985). Volk and Kwok (1992) use 0.003 as the dust to gas ratio for fitting the LRS spectrum for extreme carbon stars. Gehrz (1989) determine the dust to gas ratio for oxygen-rich stars to be roughly from 3×10^{-3} to 10^{-2} .

TABLE 3.2 Stellar Parameters From Lambert et al. (1986)

star	T_{eff}	$[^{12}\text{C}+^{13}\text{C}/\text{H}]$	$[^{16}\text{O}/\text{H}]$	Φ_0
AQ Sgr	2650	0.12	-0.14	1.4×10^{-4}
BL Ori	2960	-0.02	-0.29	2.0×10^{-4}
R Lep	2390	0.24	-0.02	1.9×10^{-4}
R Scl	2550	-0.21	-0.59	7.5×10^{-4}
RT Cap	2620	0.10	-0.19	5.2×10^{-4}
RV Cyg	2600	0.17	-0.16	1.2×10^{-3}
RY Dra	2500	-0.06	-0.38	6.1×10^{-4}
S Sct	2895	0.17	-0.11	4.6×10^{-4}
ST Cam	2800	0.08	-0.23	7.3×10^{-4}
T Lyr	2380	-0.14	-0.50	7.6×10^{-4}
TU Gem	2770	-0.03	-0.36	7.3×10^{-4}
TW Oph	2450	0.07	-0.27	1.0×10^{-3}
TX Psc	3030	-0.27	-0.10	2.1×10^{-3}

Figure 3.9 shows the plots of terminal velocity distributions for gas and dust as the function of rest dust-to-gas ratio Φ_0 , Figure 3.10a and Figure 3.10b show the emergent spectra for different dust to gas ratios. The parameters used here are $T_{\text{eff}} = 2500$ K, $L_* = 5 \times 10^4 L_{\odot}$, $M_* = 5 M_{\odot}$, $\dot{M} = 5 \times 10^{-5} M_{\odot}/\text{yr}$ for oxygen-rich stars and $T_{\text{eff}} = 2000$ K, $L_* = 5.6 \times 10^4 L_{\odot}$, $M_* = 5 M_{\odot}$, $\dot{M} = 5 \times 10^{-5} M_{\odot}/\text{yr}$ for carbon-rich stars and the dust grain size a is $0.05 \mu\text{m}$.

We find from Figure 3.9 that the dust-to-gas ratio could range from 2×10^{-4} to 5×10^{-3} for carbon-rich stars and from 2×10^{-3} to 2×10^{-2} for oxygen-rich stars for the velocities to be consistent with the observations. We also notice in Figures 3.10a and 3.10b that the

emergent spectra shift from short wavelengths to long wavelengths, and the feature at $\lambda = 10 \mu\text{m}$ in Figure 3.10b changes from emission to absorption. These occur because when Φ_0 is increased, the number of dust particles is increased, then the more UV photons are absorbed and re-emitted at long wavelengths and the optical depth is increased, bringing the feature at $\lambda = 9.7 \mu\text{m}$ from emission to self-absorption.

As we compare these spectrum distribution plots (Figures 3.10(a-b)) to those in Figures 3.6(a-b), the conclusion can be drawn that the spectra can be shifted from short wavelengths to long wavelengths for both carbon-rich and oxygen-rich stars and the feature at $9.7 \mu\text{m}$ changes from emission to self-absorption for oxygen-rich stars by increasing either the mass loss rate or the dust to gas ratio. The optical depth at $10 \mu\text{m}$ for changing from emission to self-absorption is about 4.0.

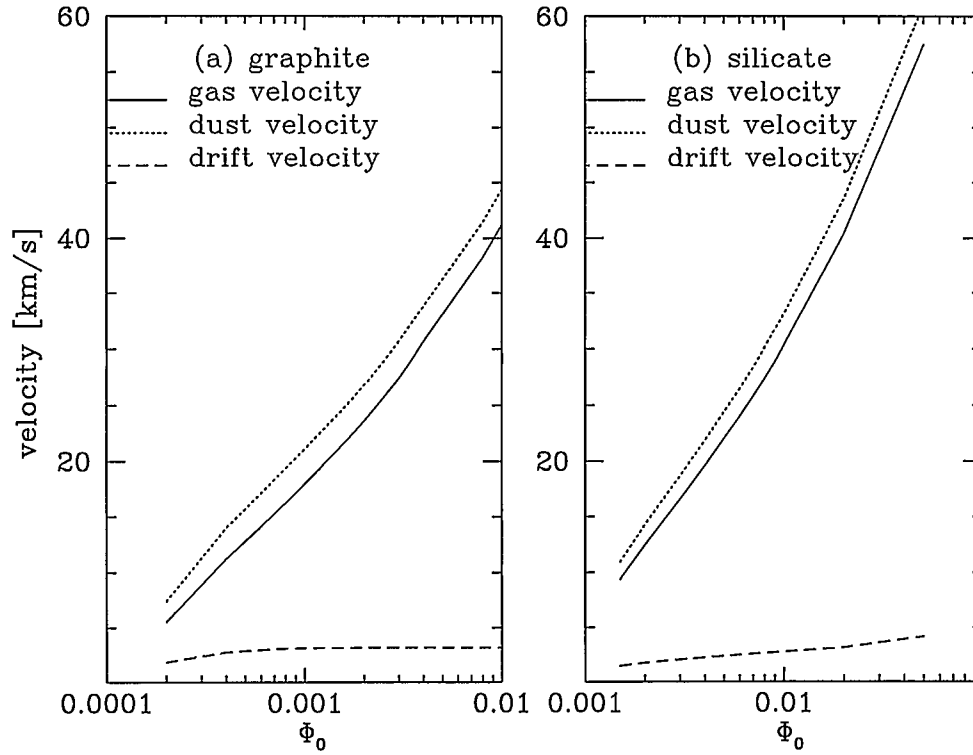


FIGURE 3.9 The terminal gas, dust and drift velocities vs dust-to-gas ratio for (a) carbon stars assuming graphite grains ($a = 0.05 \mu\text{m}$) with $\dot{M} = 5 \times 10^{-5} M_{\odot}/\text{yr}$, $L_{*} = 5.6 \times 10^4 L_{\odot}$, $M_{*} = 3 M_{\odot}$, $T_{\text{cond}} = 1000 \text{ K}$ and $T_{\text{eff}} = 2000 \text{ K}$ and (b) oxygen stars assuming silicate grains ($a = 0.05 \mu\text{m}$) with the same M_{*} , \dot{M} , T_{cond} and $L_{*} = 5 \times 10^4 L_{\odot}$, and $T_{\text{eff}} = 2500 \text{ K}$.

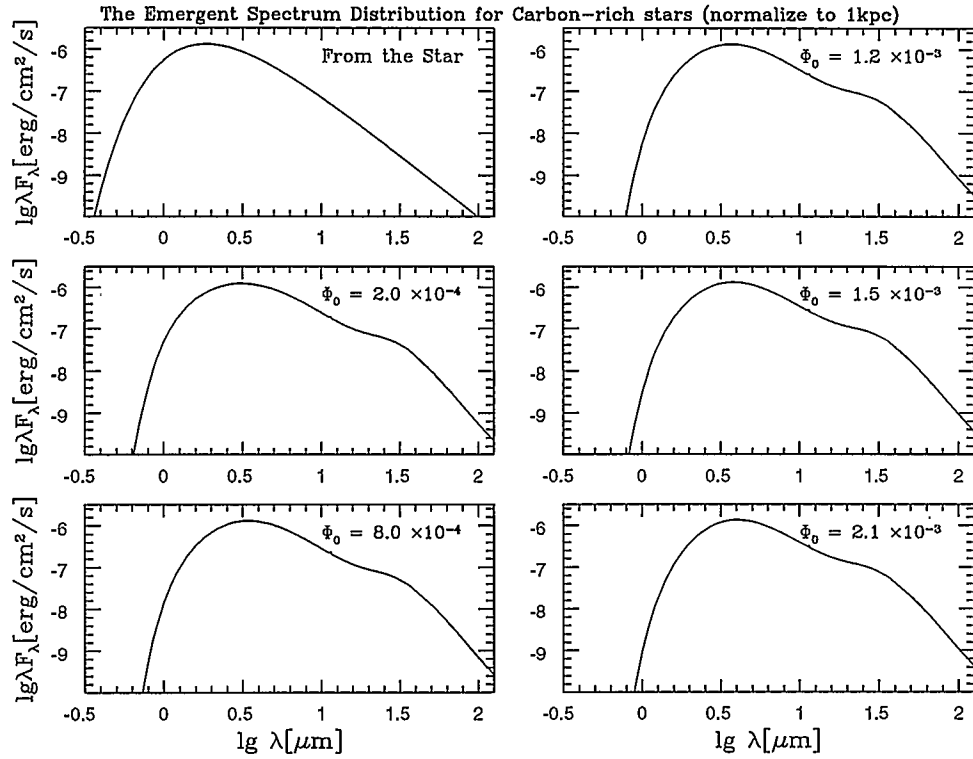


FIGURE 3.10a The emergent spectra for carbon-rich stars with graphite grains at different dust-to-gas ratios from 2×10^{-4} to 2.1×10^{-3} . The parameters used here are the same as in Figure 3.9.

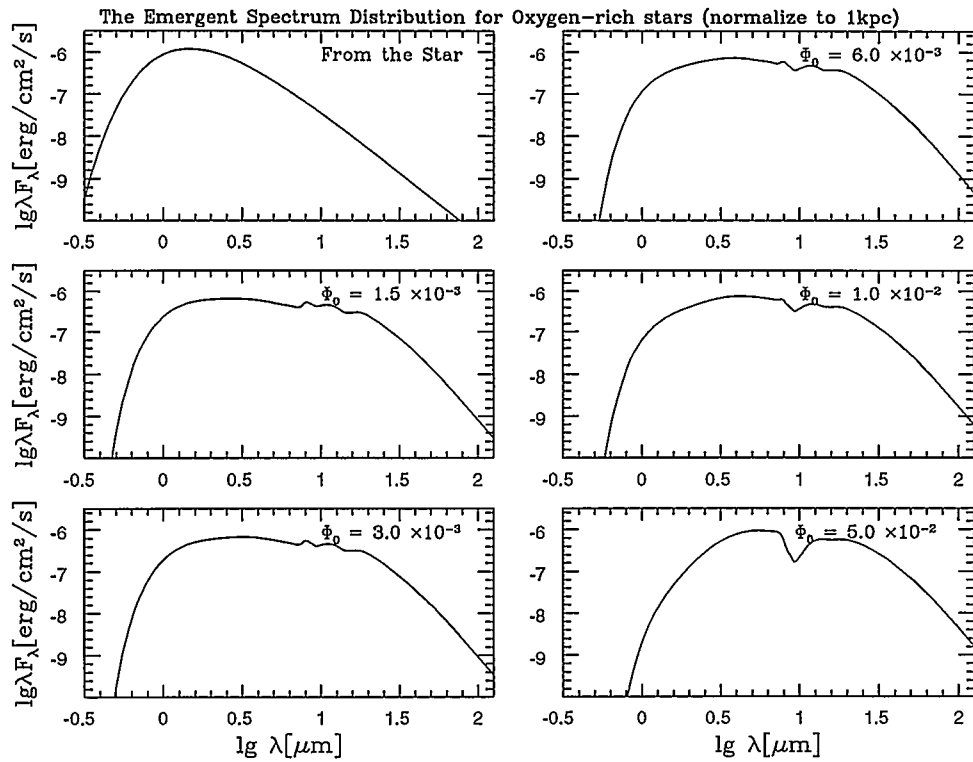


FIGURE 3.10b The emergent spectra for oxygen-rich stars with silicate grains at different dust-to-gas ratios from 1.5×10^{-3} to 5.0×10^{-2} . The parameters used here are the same as in Figure 3.9.

Chapter 4 Model Results

The calculations in chapter 3 for the comparison to the results obtained by Netzer and Elitzur (1993) simply use $L_* = 5.0 \times 10^4 L_\odot$ and $L_* = 5.6 \times 10^4 L_\odot$ as the luminosities for oxygen-rich and carbon-rich stars respectively. Both observations of M stars in external galaxies (Richer and Crabtree 1985, Pritchett et al. 1987) and the model calculations by Bryan, Volk and Kwok (1990) show that luminosity function peaks at $M_{\text{bol}} = -4.3$ (absolute bolometric magnitude, equivalent to $4.3 \times 10^3 L_\odot$) and has a long tail extending to $M_{\text{bol}} = -7.0$. Surveys of carbon stars in the Magellanic clouds show a luminosity function peaked at $M_{\text{bol}} = -4.8$ and no carbon stars seen with $M_{\text{bol}} < -6.0$ (Cohen et al. 1981; Wood, Bessel & Fox 1983; Wood 1987). If $L_* = 5.0 \times 10^4 L_\odot$ and $L_* = 5.6 \times 10^4 L_\odot$ are used for oxygen-rich and carbon-rich sample star calculations, it would be contrary to the observations. So we have to seek the luminosity and other stellar parameters which are close to the observations.

4.1 Stellar Parameters of Model Calculations

Let us define the first helium flash (thermal pulse) as the zero point in time ($t = 0$), and mass loss is assumed to begin at this point. The initial core masses [$M_c(0)$] for low-mass (1-3 M_\odot) stars have been calculated by Boothroyd and Sackmann (1988b). The corresponding values for higher mass stars (3-9 M_\odot) are given by Iben and Renzini (1983). In order to join the two regions together, we have adopted the following formulae interpolated by Bryan, Volk and Kwok (1990) in solar mass units:

$$\begin{aligned}
M_c(0) &= 0.483 + 0.021M_*(0) & 1.25 < M_*(0) < 3 \\
M_c(0) &= 0.546 + 0.087 \left[\left(\frac{M_*(0)}{3} \right)^2 - 1 \right] & 3 < M_*(0) < 9.
\end{aligned} \tag{76}$$

During the interpulse period (the period between two consecutive pulsations), the stellar luminosity can be approximated by a core mass-luminosity relationship (Paczynski 1971). The following empirical formulae are adopted based on the core mass-luminosity relationships given in Boothroyd and Sackmann (1988a):

$$\begin{aligned}
L_* &= 38480 (M_c - 0.434), & 0.434 < M_c < 0.519 \\
L_* &= 52000 (M_c - 0.456), & 0.519 < M_c < 0.775 \\
L_* &= 59250 (M_c - 0.495), & 0.775 < M_c < 0.900 \\
L_* &= 65000 (M_c - 0.543), & 0.900 < M_c < 1.41,
\end{aligned} \tag{77}$$

where the units for M_c and L_* are M_\odot and L_\odot respectively. Since mass of the core increases as the result of the nuclear burning, the rate of change in the mass of the core can be expressed in the unit of M_\odot/yr as (Bryan, Volk & Kwok 1990)

$$\dot{M}_c = (L_*/xE_H) = a(M_c - b), \tag{78}$$

where $x = 0.7$ is the hydrogen mass abundance, $E_H = 6 \times 10^{18}$ ergs is the energy released by converting 1 g of hydrogen to helium, and a and b are constants. By substituting equation (77) into equation (78), the equation (78) can be integrated to obtain the core mass with time as

$$M_c = b + (M_c(0) - b) e^{at} M_\odot/\text{yr}. \tag{79}$$

We also have adopted the following mass loss formula from Bryan, Volk and Kwok (1990)

$$\dot{M} = -1.15 \times 10^{-13} [M_*(0)^2 - 10.6M_*(0) - 10.2] L_* R_* M_*^{-1} M_\odot \text{yr}^{-1}, \quad (80)$$

where the star mass M_* ranges between $1.25 M_\odot$ and $8 M_\odot$; R_* is the radius of the star.

Then the mass of the star at time t is

$$M_*(t) = M_*(0) - \int_0^t \dot{M}(t') dt'. \quad (81)$$

Once we get the total mass, the effective temperature (T_{eff}) of the star can be obtained from Wood and Cahn (1977):

$$\lg(T_{\text{eff}}) = [101.49 - 2.5 \lg(L_*) + 0.533M_*] / 26.64. \quad (82)$$

Then the radius of the star can be obtained from

$$R_*(t) = \left[\frac{L_*(t)}{4\pi\sigma T_{\text{eff}}^4(t)} \right]^{\frac{1}{2}}, \quad (83)$$

where σ is the Stephan-Boltzmann constant.

In the following calculations, we use these formulae to estimate the mass, luminosity, effective temperature and the mass loss rate of the star. You may wonder whether the time dependent parameters can be used in the time independent steady state model calculations. The lifetime of an AGB star is about 10^6 years, much longer than the time of 3×10^3 years during which the gas moves from the inner radius to the outer radius (10^{17} cm) if the average outflow speed is assumed to be 10 km/s. So we can reasonably assume that the stellar parameters will not change much during the time of model calculations and that the results of steady state model calculations are good approximations.

4.2 Sample Calculations of AGB Stars

After investigating the stellar parameters (section 4.1) and their effects (chapter 3), we are ready to carry on the sample calculations of the star by using our model.

By using the stellar parameters based on the above formulae from (76) through (83), the calculations have been performed for the circumstellar envelopes of sample stars. Stars which are used to compare with the models are listed in Table 4.1 and Table 4.2 (Netzer & Elitzur 1993) for oxygen-rich and carbon-rich stars respectively. R in Tables 4.1 and 4.2 is the abbreviation for the word "reference".

TABLE 4.1 Oxygen Star Mass-Loss Rates and Terminal Velocities From Observations

Star	\dot{M} (M_{\odot}/yr)	v_e (km/s)	R	Star	\dot{M} (M_{\odot}/yr)	v_e (km/s)	R
IRC+40004	2.7×10^{-5}	24.2	1	CRL 278	4.2×10^{-7}	7.6	2
IRC+10011	1.4×10^{-5}	23.0	1	T Cas	5.6×10^{-8}	5.2	2
IRC-30023	1.4×10^{-6}	11.6	2	CIT 4	6.4×10^{-6}	12.2	3
IRC+30021	8.0×10^{-6}	13.0	3	R Hor	2.1×10^{-7}	6.6	4
IRAS18467-4802	3.8×10^{-6}	11.0	4	V Eri	4.2×10^{-7}	13.0	2
IRAS21554+6204	2.1×10^{-5}	12.6	2	R Aur	1.0×10^{-6}	10.9	1
IRAS22272+5435	6.3×10^{-5}	11.6	3	V Cam	8.0×10^{-7}	12.2	6
IRS+60427	5.8×10^{-6}	19.0	4	GX Mon	1.9×10^{-5}	18.7	2
IRC+40483	8.2×10^{-6}	18.0	1	VY CMa	2.2×10^{-5}	35.9	2
IRC-10529	1.5×10^{-5}	15.8	1	Y Lyn	3.0×10^{-7}	5.4	5
IRAS20028+3910	1.1×10^{-5}	10.5	2	RS Cnc	6.3×10^{-7}	5.3	1
CRL 6815S	5.0×10^{-5}	25.1	10	EP Aqr	5.7×10^{-7}	8.6	2
RT Cep	4.5×10^{-6}	18.5	11	TW Peg	4.0×10^{-7}	9.5	2
CRL 2999	5.5×10^{-5}	17.6	10	SV Peg	1.0×10^{-6}	11.0	10
R Cas	8.6×10^{-7}	12.3	1	V PsA	6.9×10^{-7}	21.0	4

TABLE 4.1 Continued

IRC+10420	3.0×10^{-4}	51.7	1	R LMi	3.2×10^{-7}	6.0	9
IRC+30404	1.1×10^{-5}	15.0	4	IW Hya	5.2×10^{-6}	14.0	2
IRC+50137	6.5×10^{-6}	14.7	1	R Leo	9.2×10^{-7}	6.5	9
IRC+60154	1.1×10^{-5}	19.9	2	R Crt	6.9×10^{-7}	11.0	2
IRC+70066	1.1×10^{-5}	21.1	1	BK Vir	1.4×10^{-7}	4.7	6
IRC+60169	6.3×10^{-6}	16.9	1	RT Vir	1.6×10^{-6}	8.4	10
IRAS07134+1005	1.8×10^{-5}	10.0	3	SW Vir	3.2×10^{-7}	9.4	11
IRC-30163E	2.2×10^{-7}	8.0	2	R Hya	6.9×10^{-8}	7.5	5
TX Cam	3.0×10^{-6}	16.9	5	W Hya	1.1×10^{-7}	9.7	5
CRL 2477	9.2×10^{-5}	22.4	6	RX Boo	9.2×10^{-7}	7.8	9
IRC+4019	2.1×10^{-5}	19.8	7	WX Ser	1.4×10^{-6}	11.5	7
IRC20101	9.4×10^{-6}	20.0	8	X Her	1.1×10^{-6}	8.8	2
IRAS09371+1212	2.1×10^{-6}	25.0	8	CRL 1822	2.9×10^{-5}	14.2	4
NGC 6302	1.1×10^{-4}	22.5	6	30g Her	1.9×10^{-7}	7.5	2
161796	1.5×10^{-5}	11.5	8	MW Her	6.5×10^{-5}	23.3	3
IRC+10365	6.3×10^{-6}	16.7	1	CRL 5397	7.9×10^{-6}	20.5	10
IRC+10374	5.2×10^{-6}	18.5	3	89 Her	8.0×10^{-7}	4.4	8
1943 Sag	1.9×10^{-7}	8.0	4	VX Sag	1.3×10^{-5}	30.0	4
CRL 2343	1.6×10^{-4}	33.0	8	RS Cra	7.0×10^{-6}	20.7	10
CRL 2362	4.6×10^{-5}	22.0	10	R Aql	1.0×10^{-7}	10.1	5
IRC 30398	7.7×10^{-6}	13.2	10	VY 2-2	2.4×10^{-6}	12.1	1
3880 Sag	1.5×10^{-5}	22.2	10	M1-92	3.1×10^{-5}	25.5	7
NML Tau	4.5×10^{-6}	22.0	1	GY Aql	6.2×10^{-6}	11.5	5
IRC+80040	1.5×10^{-6}	12.0	11	RR Aql	2.9×10^{-7}	7.4	2
CRL 2646	2.8×10^{-6}	15.4	6	T Cep	8.6×10^{-8}	5.0	6
IRAS16105-4205	1.5×10^{-5}	14.0	10	UU Peg	7.4×10^{-7}	13.5	6
RU Cyg	1.1×10^{-6}	14.2	6	μ Cep	3.4×10^{-7}	10.0	12

TABLE 4.2 Carbon Star Mass-Loss Rates and Terminal Velocities From Observations

Star	\dot{M} (M_{\odot}/yr)	v_e (km/s)	R	Star	\dot{M} (M_{\odot}/yr)	v_e (km/s)	R
IRAS00210+6221	3.2×10^{-6}	13.0	13	Z Psc	6.1×10^{-8}	3.5	14
IRC+60041	1.3×10^{-6}	23.3	6	CRL 190	6.8×10^{-5}	19.7	2
IRAS02152+2822	2.3×10^{-6}	8.9	6	R Scl	4.2×10^{-6}	17.6	15
IRC+60144	1.1×10^{-5}	20.4	1	R For	1.0×10^{-6}	20.0	15
IRC+50096	5.5×10^{-6}	16.8	1	CRL 341	1.7×10^{-5}	14.2	3
IRAS04530+4427	4.0×10^{-6}	20.8	16	TW Hor	8.0×10^{-8}	5.3	15
IRAS05104+2055	1.1×10^{-5}	25.2	16	CRL 482	1.7×10^{-5}	16.0	1
IRAS05136+4712	5.7×10^{-6}	14.7	16	U Cam	1.6×10^{-6}	22.0	3
NGC 2346	1.0×10^{-5}	19.0	7	CRL 5102	4.9×10^{-6}	13.3	2
CRL 1058	1.1×10^{-5}	23.8	2	CRL 618	7.7×10^{-5}	21.5	1
IRAS07217-1246	2.4×10^{-6}	24.9	16	ST Cam	1.8×10^{-7}	10.0	14
IRC-20131	8.7×10^{-6}	25.5	6	R Lep	4.5×10^{-7}	9.8	2
IRAS07582-1933	4.6×10^{-6}	14.6	16	W Ori	1.2×10^{-7}	10.9	17
IRAS08045-1524	1.4×10^{-6}	13.7	16	S Aur	1.4×10^{-6}	16.5	3
IRAS08074-3615	2.1×10^{-5}	17.3	10	CRL 809	1.7×10^{-5}	30.0	7
CRL 1235	2.4×10^{-5}	20.7	2	W Pic	1.1×10^{-7}	7.0	15
IRAS11308-1020	2.5×10^{-6}	11.0	16	Y Tau	4.1×10^{-7}	10.7	15
IRAS15194-5115	6.9×10^{-6}	23.3	4	CRL 865	2.3×10^{-5}	15.3	1
S Sct	7.6×10^{-7}	19.9	15	IRC+40485	3.4×10^{-6}	14.9	1
IRC+10401	1.5×10^{-5}	17.4	3	S Cep	2.4×10^{-6}	22.4	2
V Aql	1.6×10^{-7}	8.2	14	V460 Cyg	3.4×10^{-7}	11.4	14
V1942 Sag	1.7×10^{-7}	10.0	15	RV Cyg	5.2×10^{-7}	14.7	14
IRC-10502	4.4×10^{-6}	22.5	2	PQ Cep	2.0×10^{-6}	21.7	3
UX Dra	1.5×10^{-7}	6.9	14	CRL 2901	1.7×10^{-5}	34.2	3
AQ Sag	1.8×10^{-7}	6.0	4	CRL 2985	2.3×10^{-6}	19.2	6

TABLE 4.2 Continued

CPD-568032	1.6×10^{-6}	17.0	4	TU Gem	5.2×10^{-7}	11.4	14
IRAS17217-3916	1.4×10^{-6}	8.8	16	CRL 933	2.3×10^{-6}	25.8	6
IRAS17376-3021	4.9×10^{-6}	10.3	16	CRL 935	3.6×10^{-6}	12.9	3
IRAS17581-1744	4.4×10^{-6}	16.1	16	CRL 954	5.8×10^{-6}	21.4	3
IRAS18248-0839	1.9×10^{-6}	16.1	16	UU Aur	4.5×10^{-7}	11.5	2
IRAS18269-1257	7.6×10^{-6}	23.5	16	CRL 971	6.3×10^{-6}	9.0	2
IRAS18424+0346	5.1×10^{-7}	20.0	18	CL Mon	2.5×10^{-6}	27.0	6
IRAS19068+0544	1.6×10^{-5}	20.5	16	W CMa	2.7×10^{-7}	11.7	15
IRAS19346+1209	1.7×10^{-5}	12.0	18	R Vol	1.7×10^{-6}	19.3	15
IRAS19454+2920	1.4×10^{-5}	14.0	8	CRL 5250	1.7×10^{-5}	16.1	2
IRAS19475+3119	2.3×10^{-5}	17.0	8	X Cnc	2.2×10^{-7}	12.0	14
IRAS19477+2401	1.7×10^{-6}	12.5	13	CRL 5254	6.4×10^{-5}	12.8	2
IRAS20435+3825	1.4×10^{-6}	20.6	16	IRC+10216	5.5×10^{-5}	15.2	1
IRAS20532+5554	2.9×10^{-6}	11.4	16	Y Hya	2.3×10^{-7}	10.2	15
IRAS21003+4801	6.9×10^{-6}	14.8	6	X Vel	1.7×10^{-7}	8.6	15
IRAS21147+5110	1.1×10^{-4}	11.5	18	CIT 6	2.3×10^{-6}	16.9	1
IRAS21223+5114	1.3×10^{-5}	20.6	16	IRC-10236	4.7×10^{-6}	10.9	1
IRAS21282+5050	1.4×10^{-5}	18.0	19	U Ant	8.7×10^{-7}	21.2	15
IRAS21373+4540	1.1×10^{-6}	14.7	16	U Hya	4.9×10^{-7}	10.7	2
IRAS21449+4950	2.9×10^{-6}	14.6	16	VY UMa	1.1×10^{-7}	8.4	14
IRAS21489+5301	1.5×10^{-5}	22.3	2	V Hya	4.5×10^{-5}	24.0	6
IRAS22303+5950	5.4×10^{-6}	18.3	16	Y CVn	7.1×10^{-8}	6.3	2
IRAS23268+6854	1.2×10^{-6}	8.0	13	RU Vir	9.5×10^{-6}	16.9	1
IRAS23279+5336	1.1×10^{-6}	8.8	16	RY Dra	3.3×10^{-7}	13.0	17
IRAS23321+6545	5.2×10^{-5}	15.0	4	CRL 4211	2.3×10^{-6}	20.5	4
IRC+40540	2.4×10^{-5}	14.7	1	X TrA	1.4×10^{-7}	9.2	15
CRL 1922	9.5×10^{-6}	16.6	3	V CrB	2.7×10^{-7}	6.5	3

TABLE 4.2 Continued

V463 Sco	8.4×10^{-6}	25.6	6	CRL 2417	3.4×10^{-7}	24.4	2
IRC+20326	2.3×10^{-5}	17.5	1	163075	3.7×10^{-6}	11.0	8
T Dra	1.3×10^{-6}	14.0	1	CRL 2494	8.0×10^{-5}	20.0	2
FX Ser	8.6×10^{-6}	27.0	6	RT Cap	1.0×10^{-7}	9.1	15
CRL 2135	1.3×10^{-5}	23.0	7	V Cyg	2.7×10^{-6}	14.0	17
CRL 2154	1.1×10^{-5}	27.0	3	CRL 2686	5.8×10^{-6}	23.5	2
CRL 2155	1.7×10^{-5}	15.1	1	CRL 2688	1.6×10^{-4}	19.7	1
T Lyr	1.1×10^{-7}	12.2	17	RV Aqr	2.2×10^{-6}	16.1	15
CRL 2199	1.3×10^{-5}	8.0	1	V1549 Cyg	4.6×10^{-6}	11.4	6
IRC+20370	9.3×10^{-6}	15.6	10	NGC 7027	1.1×10^{-4}	17.9	1
IRC+00365	1.5×10^{-5}	34.5	3	T Ind	8.0×10^{-8}	5.5	15
CRL 2259	1.5×10^{-5}	21.8	3	Y Pav	1.8×10^{-7}	9.4	15

References on the Tables: (1) Knapp & Morrice (1985); (2) Zuckerman & Dyck (1986a); (3) Zuckerman et al. (1986); (4) Knapp et al. (1989); (5) Wannier & Sahai (1986); (6) Zuckerman & Dyck (1989); (7) Knapp (1986); (8) Likkell et al. (1987); (9) Knapp et al. (1982); (10) Zuckerman & Dyck (1986b); (11) Knapp (1991); (12) Leborgne & Mauron (1989); (13) Arquilla, Leahy & Kwok (1986); (14) Olofsson et al. (1987); (15) Olofsson et al. (1988); (16) Rieu et al. (1987); (17) Jura et al. (1988); (18) Leahy, Kwok & Arquilla (1987); (19) Likkell et al. (1988).

It is generally believed that the formation of carbon-rich stars is due to helium shell flashes during the AGB stage of evolution cause carbon to be produced and dredged up to the surface. This occurs when the convective envelope in the outer hydrogen shell reaches into the region between the C-O core and the hydrogen shell (Iben 1981; Boothroyd & Sackmann 1988c and Bryan, Volk & Kwok 1990). Once the abundance

ratio of $[C/O] > 1$ the star changes from oxygen-rich to carbon-rich. But when and how this change happens are not considered here; if you are interested please refer to Iben (1981), Boothroyd & Sackmann (1988c), Chan and Kwok (1990), Bryan, Volk & Kwok (1990), and Kwok & Chan (1993). In our model calculations, we calculate stars with the same initial mass $M_*(0)$ at different time t (therefore with different star masses) for oxygen-rich stars and the same star mass with different initial masses for carbon-rich stars. Figure 4.1 shows the terminal gas outflow velocity versus mass loss rate for carbon-rich and oxygen-rich stars.

Figure 4.1 shows that the model results are consistent with the observations. It also shows that the velocity increases when \dot{M} is less than $10^{-5} M_{\odot}/\text{yr}$ and decreases when \dot{M} is higher than $10^{-5} M_{\odot}/\text{yr}$. These are consistent with the results from section 3.4 although the luminosity and temperature of the star is changing here along with \dot{M} according to the semi-empirical formulae (76) through (83). This means that it is possible to have low outflow velocity at very late times during the AGB phase.

Figures 4.2(a-e) show the gas velocity profiles for both carbon-rich and oxygen-rich stars for different parameters which are listed in Table 4.3.

Figures 4.2 show us that the velocity profiles are changing very rapidly out to 50 stellar radii and changing very little beyond 100 stellar radii. These mean that the density profiles are very different from the inverse square power law ($\rho \propto r^{-2}$) for the first 50 stellar radii and very similar to the inverse square power law after 100 stellar radii according to the equation (20).

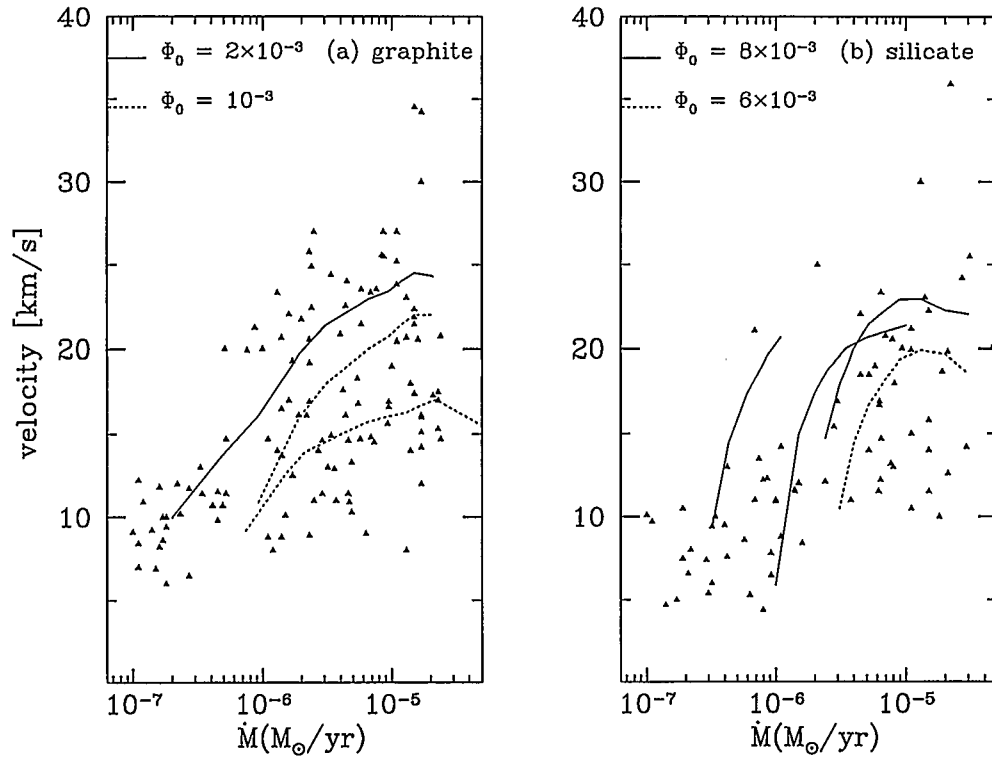


FIGURE 4.1 The terminal gas outflow velocity versus mass loss rate: (a) carbon stars; (b) oxygen stars. The parameters for model calculations are listed in Tables 4.3(a-e). The filled triangles are from observations which are listed in Table 4.1 and Table 4.2.

TABLE 4.3a The Parameters for Carbon-rich Stars ($M_* = 2.5 M_\odot$)

M_0 (M_\odot)	T_{eff} (K)	L_* (L_\odot)	\dot{M} (M_\odot/yr)	$\Phi_0 = 0.002$		$\Phi_0 = 0.001$		panel on Figures
				τ_{10}	u (km/s)	τ_{10}	u (km/s)	
3.0	3190	6177	9.3×10^{-7}	.004	16.1	.004	10.9	(a)
3.5	3094	8556	1.9×10^{-6}	.008	19.6	.007	15.9	(b)
4.5	2964	13549	4.8×10^{-6}	.017	22.3	.014	19.2	(c)
5.0	2913	16368	6.7×10^{-6}	.022	22.9	.018	20.0	(d)
6.0	2813	23707	1.2×10^{-5}	.033	24.0	.028	21.4	(e)
7.0	2727	32966	2.1×10^{-5}	.051	24.3	.043	22.0	(f)

TABLE 4.3b The Parameters for Carbon-rich Stars ($M_* = 1.5 M_\odot$)

M_0 (M_\odot)	T_{eff} (K)	L_* (L_\odot)	\dot{M} (M_\odot/yr)	Φ_0	τ_{10}	u (km/s)	panel on Figures
2.0	3089	5351	7.4×10^{-7}	0.001	.003	9.2	(a)
3.5	2926	9545	4.1×10^{-6}	0.001	.012	15.0	(b)
4.5	2822	14040	9.2×10^{-6}	0.001	.024	16.0	(c)
5.0	2775	16773	1.3×10^{-5}	0.001	.033	16.3	(d)
6.0	2690	23873	2.2×10^{-5}	0.001	.047	17.0	(e)
6.5	2581	28000	5.0×10^{-5}	0.001	.110	15.5	(f)

TABLE 4.3c The Parameters for Oxygen-rich Stars ($M_0 = 1.5 M_\odot$)

M_* (M_\odot)	T_{eff} (K)	L_* (L_\odot)	\dot{M} (M_\odot/yr)	Φ_0	τ_{10}	u (km/s)	panel on Figures
1.30	3112	4435	3.2×10^{-7}	0.008	.36	9.33	(a)
1.16	3062	5000	4.3×10^{-7}	0.008	.37	14.4	(b)
1.00	3010	5520	6.0×10^{-7}	0.008	.40	17.4	(c)

Table 4.3c continued

0.82	2961	6000	8.6×10^{-7}	0.008	.53	19.6	(d)
0.70	2935	6230	1.1×10^{-6}	0.008	.55	20.6	(e)

TABLE 4.3d The Parameters for Oxygen-rich Stars ($M_0=3.0 M_\odot$)

M_* (M_\odot)	T_{eff} (K)	L_* (L_\odot)	\dot{M} (M_\odot/yr)	Φ_0	τ_0	u (km/s)	panel on Figures
2.4	3173	6330	1.0×10^{-6}	0.008	1.3	5.9	(a)
1.7	3022	7470	2.0×10^{-6}	0.008	1.2	17.5	(b)
1.5	2982	7700	2.5×10^{-6}	0.008	1.4	18.8	(c)
1.1	2928	7935	3.5×10^{-6}	0.008	1.8	20.0	(d)
0.9	2886	8055	5.0×10^{-6}	0.008	2.5	20.6	(e)
0.6	2820	10000	1.0×10^{-5}	0.008	4.3	21.3	(f)

TABLE 4.3e The Parameters for Oxygen-rich Stars ($M_0=5 M_\odot$)

M_* (M_\odot)	T_{eff} (K)	L_* (L_\odot)	\dot{M} (M_\odot/yr)	$\Phi_0 = 8 \times 10^{-3}$		$\Phi_0 = 6 \times 10^{-3}$		panel on Figures
				τ_{10}	u (km/s)	τ_{10}	u (km/s)	
4.0	3153	14800	3.1×10^{-6}	1.2	17.9	1.3	10.5	(a)
3.5	3064	15514	4.0×10^{-6}	1.4	20.0	1.4	14.4	(b)
2.5	2913	16368	7.0×10^{-6}	1.7	21.4	1.6	16.7	(c)
2.0	2844	16632	9.0×10^{-6}	2.8	22.9	2.5	19.4	(d)
1.5	2775	16773	1.3×10^{-5}	4.0	22.9	3.5	19.9	(e)
1.1	2723	16806	2.0×10^{-5}	6.1	22.3	5.3	19.7	(f)

Figures 4.3(a-c) show the model spectra at different radii for both carbon-rich and oxygen-rich stars. These show us that the spectra shift to long wavelengths as the observation point moves away from the central star. This is because the further the

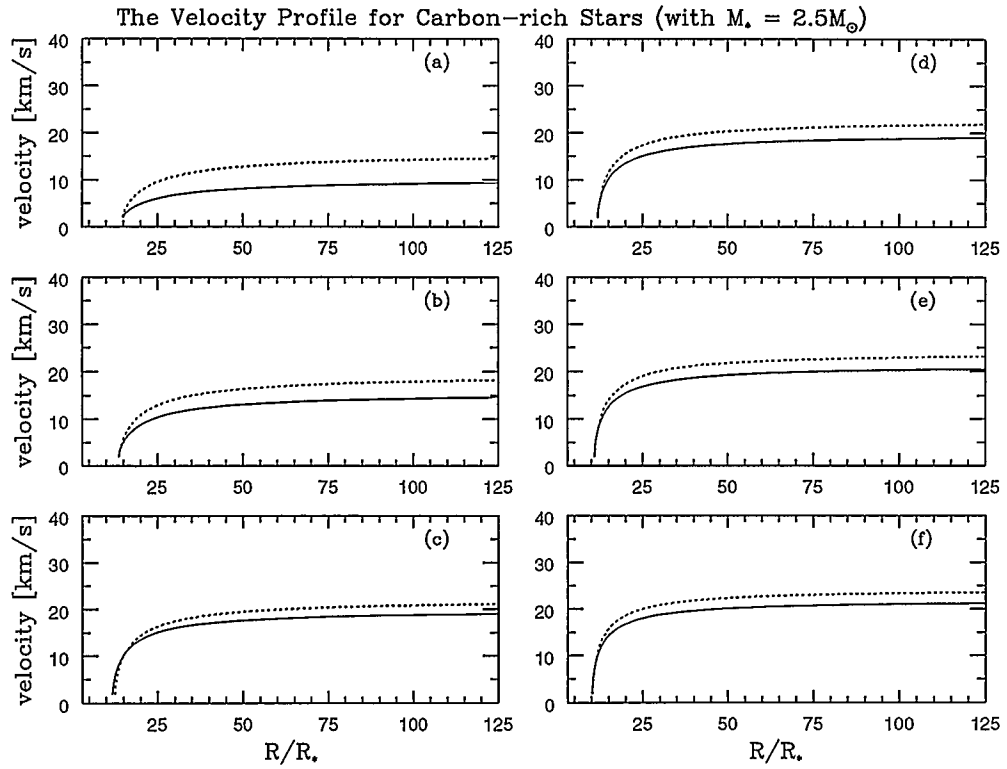


FIGURE 4.2a The velocity profiles for carbon-rich stars with the solid lines for $\Phi_0 = 0.001$ and the dotted lines for $\Phi_0 = 0.002$. The parameters used here are listed in Table 4.3a.

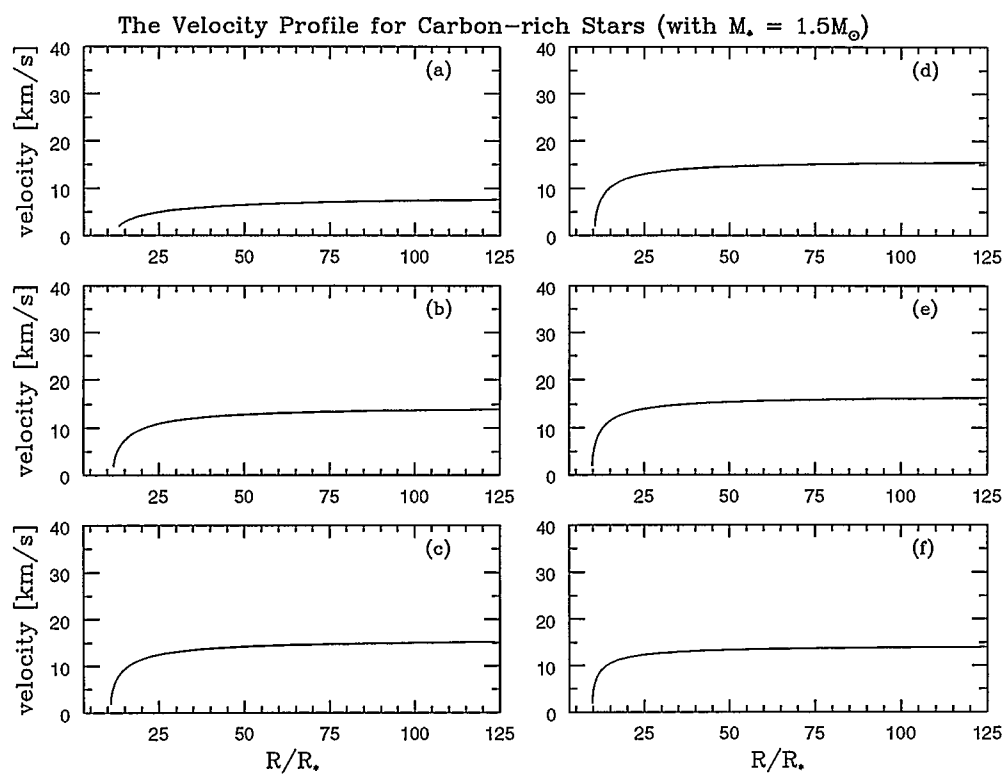


FIGURE 4.2b The velocity profiles for carbon-rich stars. The parameters used here are listed in Table 4.3b.

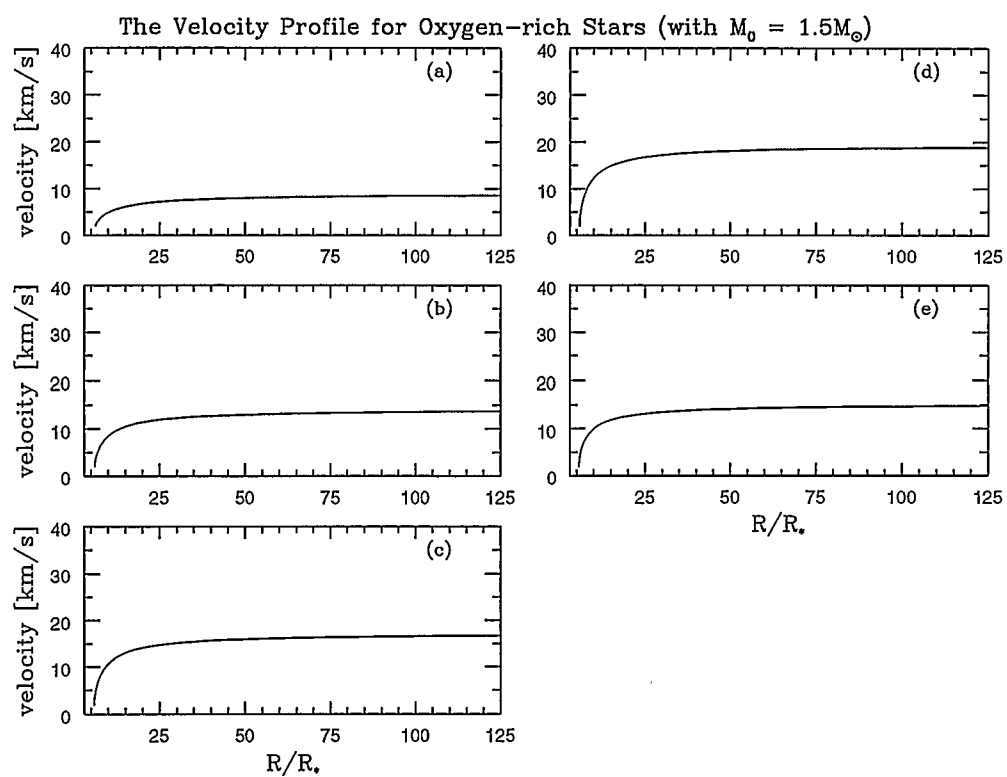


FIGURE 4.2c The velocity profiles for oxygen-rich stars. The parameters used here are listed in Table 4.3c.

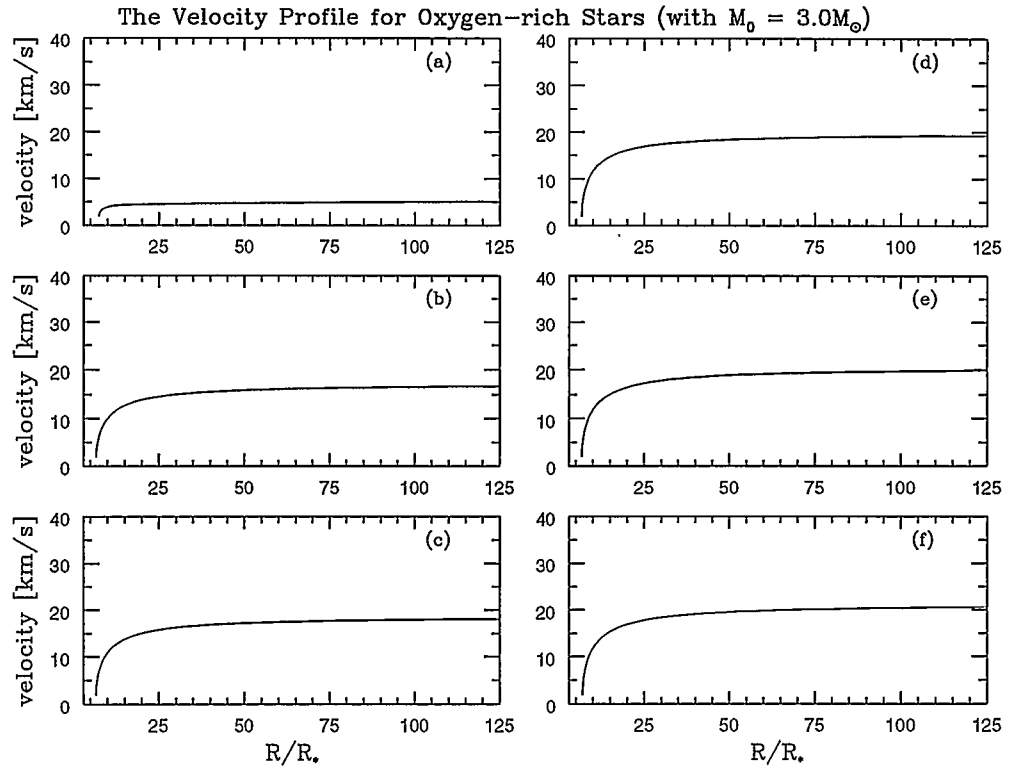


FIGURE 4.2d The velocity profiles for oxygen-rich stars. The parameters used here are listed in Table 4.3d.

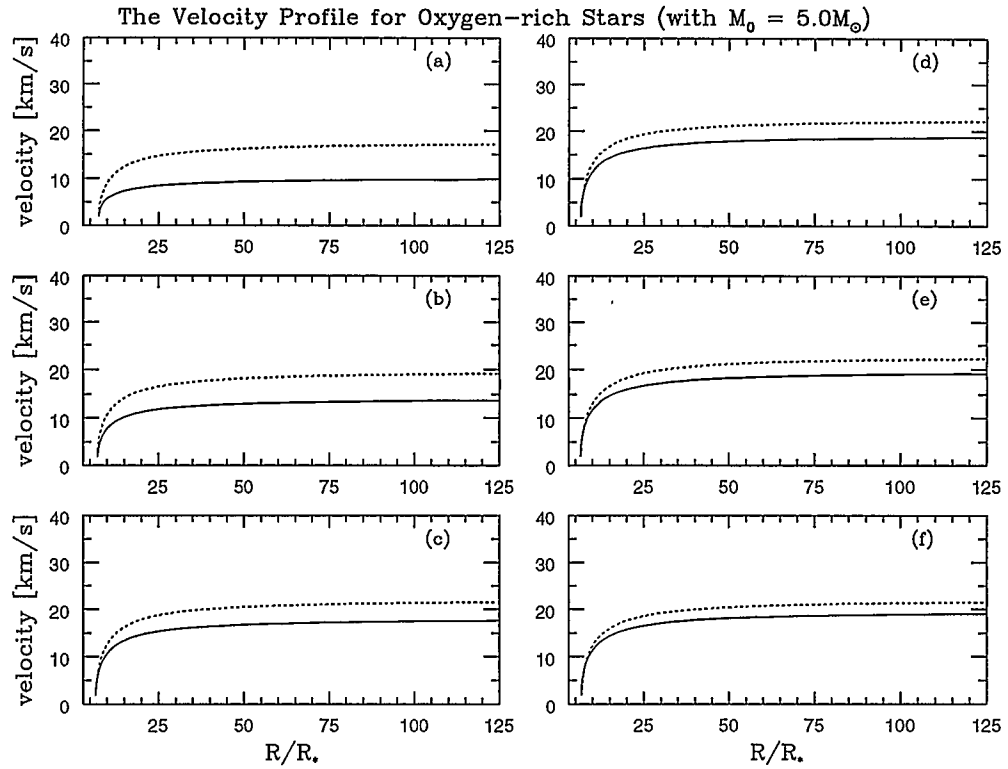


FIGURE 4.2e The velocity profiles for oxygen-rich stars with the solid lines for $\Phi_0 = 0.006$ and the dotted lines for $\Phi_0 = 0.008$. The parameters used here are listed in Table 4.3e.

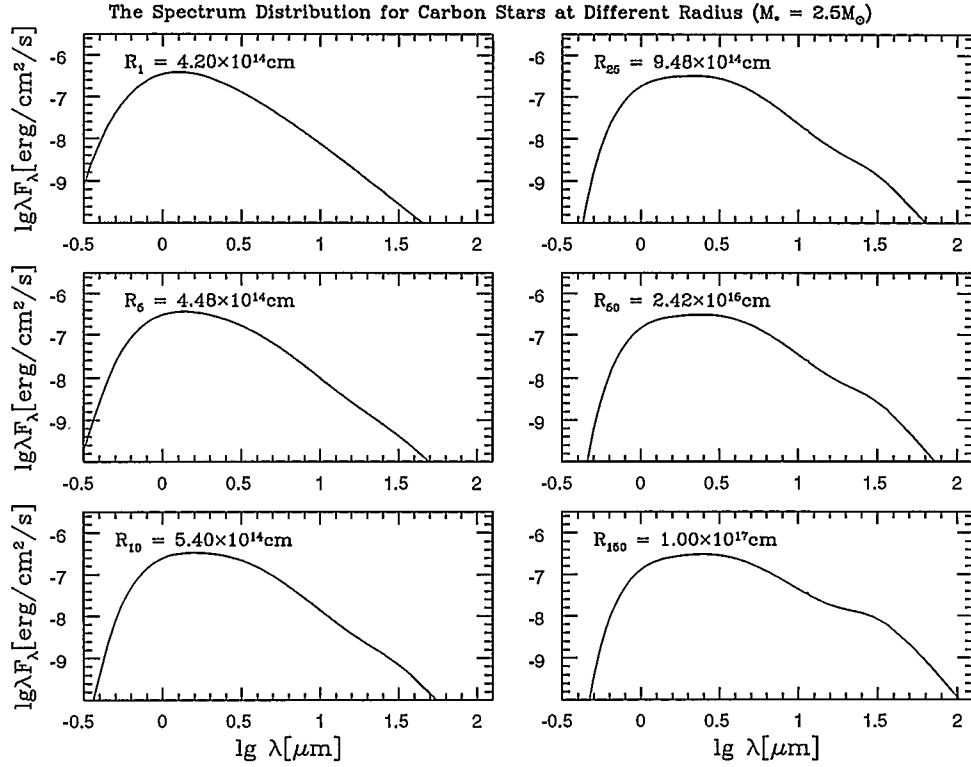


FIGURE 4.3a The model spectra at different radii for a carbon star. The parameters used here are listed on the fifth row in Table 4.3a with $\Phi_0 = 0.002$.

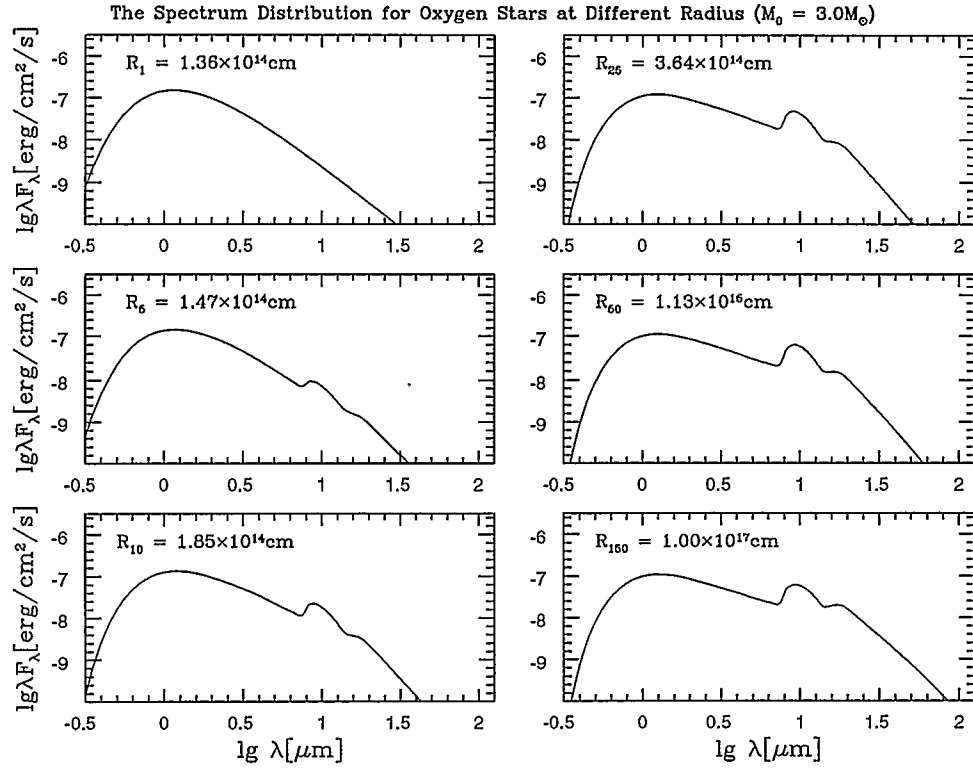


FIGURE 4.3b The model spectra at different radius for an oxygen star. The parameters used here are listed on the second row in Table 4.3d.

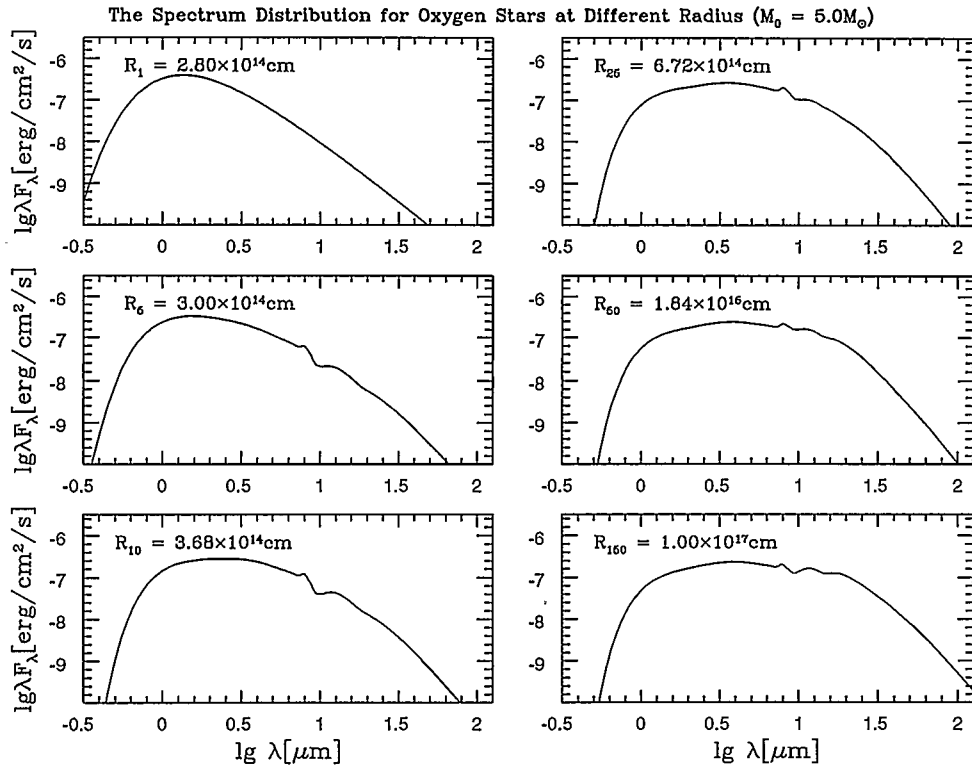


FIGURE 4.3c The model spectra at different radii for an oxygen star. The parameters used here are listed on the last row in Table 4.3e with $\Phi_0 = 0.008$.

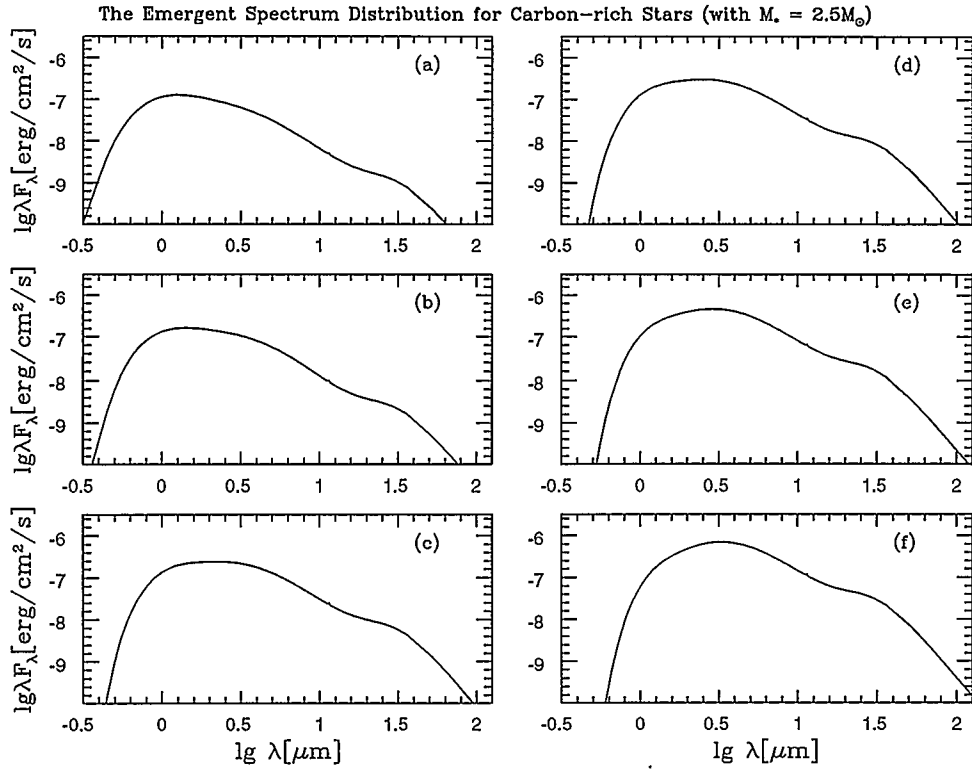


FIGURE 4.4a The emergent spectrum distributions for carbon stars. The parameters used here are listed in Table 4.3a with $\Phi_0 = 0.002$.

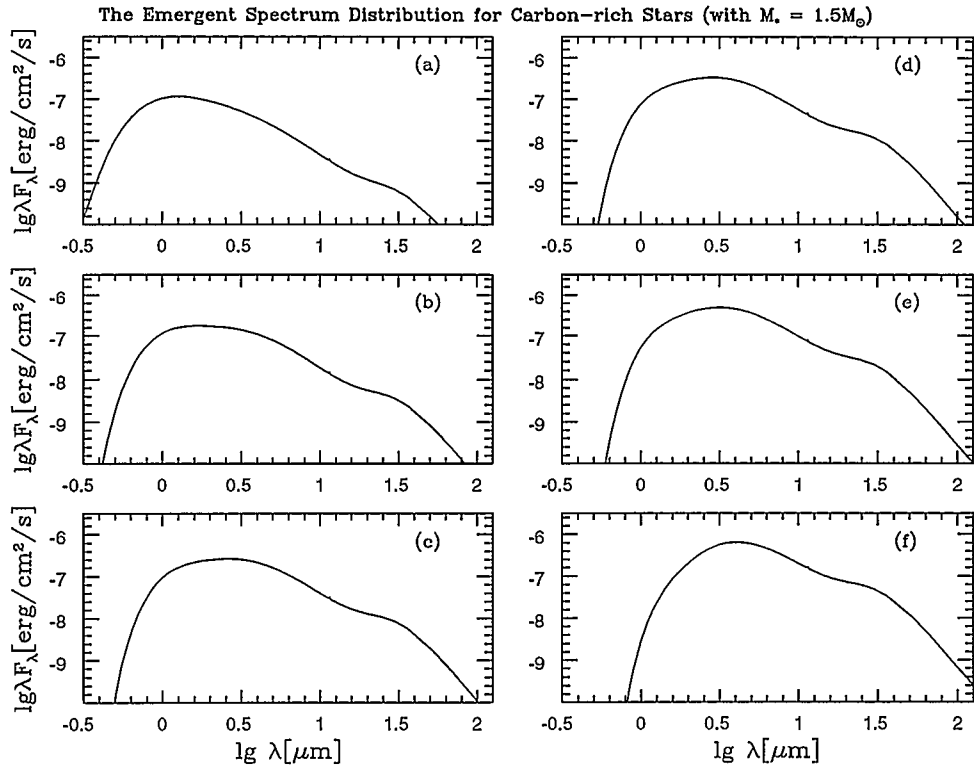


FIGURE 4.4b The emergent spectrum distributions for carbon stars. The parameters used here are listed in Table 4.3b.

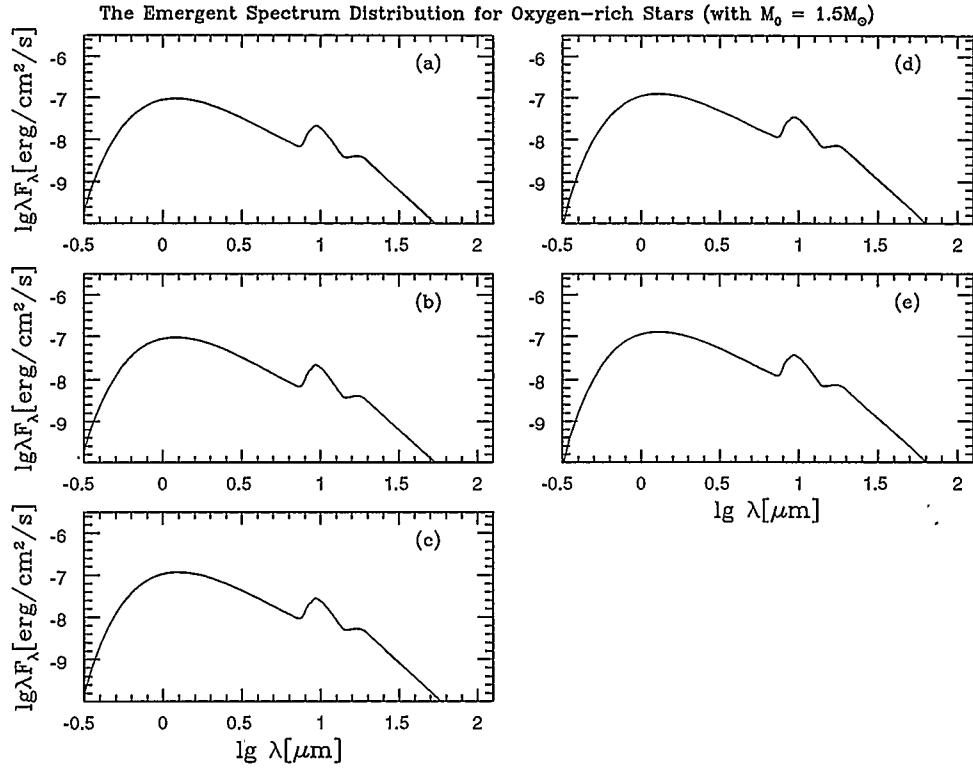


FIGURE 4.4c The emergent spectrum distributions for oxygen stars. The parameters used here are listed in Table 4.3c.

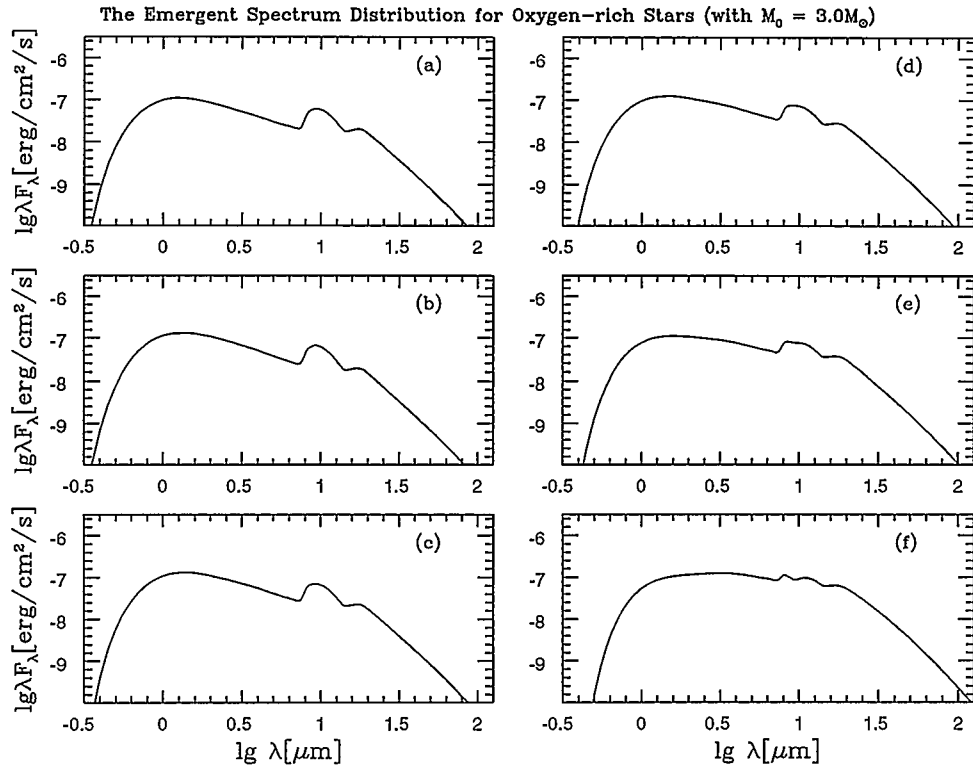


FIGURE 4.4d The emergent spectrum distributions for oxygen stars. The parameters used here are listed in Table 4.3d.

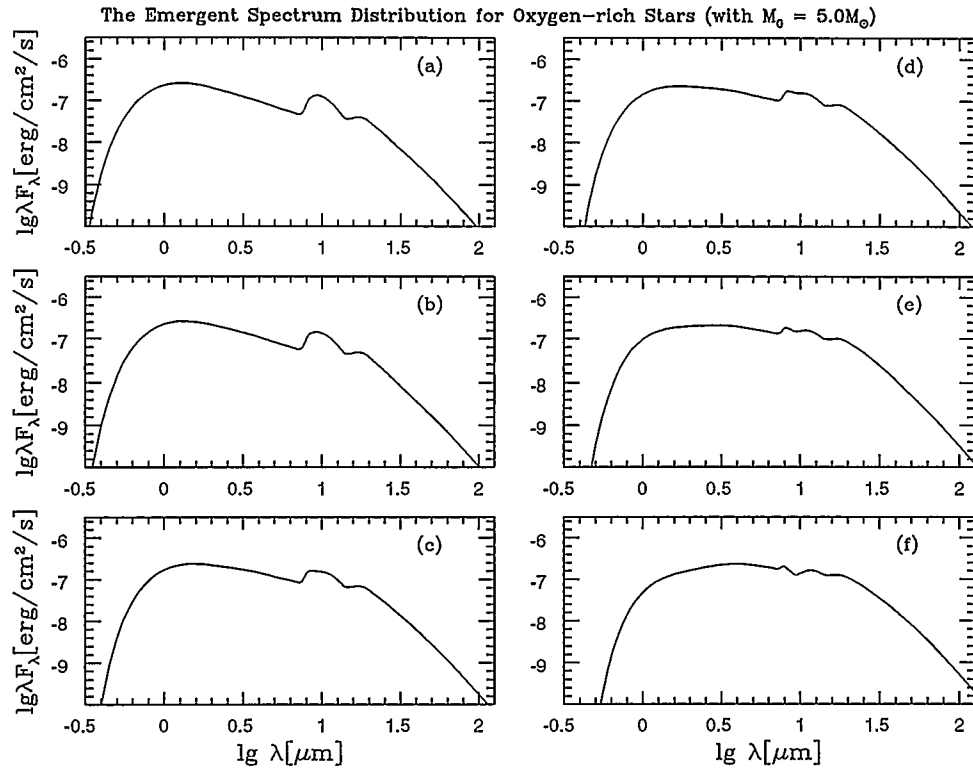


FIGURE 4.4e The emergent spectrum distributions for oxygen stars. The parameters used here are listed in Table 4.3e with $\Phi_0 = 0.008$.

distance from the star, the more the dust materials are involved and the lower the temperature inside the shell is. Figures 4.3 also show that the shape of the spectrum distribution changes rapidly for the first 50 grid points along the radial direction and changes little after the 50th grid point especially when the mass loss rate is not very high ($\leq 10^{-5} M_{\odot}/\text{yr}$).

Figures 4.4(a-e) show the emergent spectra for both carbon-rich and oxygen-rich stars; the parameters used here are listed in Table 4.3. They show us that the spectra shift from short wavelengths to long wavelengths. Since the models for the same initial mass at different time for oxygen-rich stars, Figures 4.4(c-e) show the spectral evolution for oxygen-rich stars: the spectra shift from short to long wavelengths and the silicate feature at $9.7 \mu\text{m}$ changes from emission to self absorption as time goes on.

4.3 Fitting of Spectral Energy Distributions

4.3.1 IRAS Data

The Infrared Astronomical Satellite (IRAS) was launched in 1983, with the purpose of carrying out a survey of the sky in the middle to far-infrared wavelength range from space. Over the 10 month lifetime of the satellite, IRAS surveyed 96% of the sky using medium band infrared photometry at wavelengths of 12, 25, 60 and $100 \mu\text{m}$. Over 245,000 point sources were identified in the course of the survey. At the same time a low-resolution spectrometer ($\lambda/\Delta\lambda = 40$) covering the wavelength range from 7.7 to $23 \mu\text{m}$ was in operation, providing the spectra of the brighter point sources (Volk & Kwok

1988). The satellite is described by Pauw (1983) while details of the data processing and the characteristics of various catalogs produced from the data are given in the IRAS Explanatory Supplement (1985). A total of 5425 spectra were obtained by IRAS to form the Catalog of Low Resolution Spectra (LRSC 1986). Out of the 5425 spectra, 2113 show the 10 μm silicate dust feature. This group of objects include both emission and absorption feature sources, indicating a wide range of dust optical depths in the sample. Although some of these objects are associated with early-type stars embedded in interstellar dust, HII regions, and sources in the star formation regions, most of them are expected to be intermediate-mass AGB stars. We select three sources from this catalog: AFGL3068 (carbon-rich star), α Ceti (oxygen-rich with 9.7 μm emission feature) and OH25.6+0.6 (oxygen-rich with 9.7 μm absorption feature). Near-infrared data for these stars comes from NASA Catalog of Infrared Observations (1993).

4.3.2 Colour Corrections

In the IRAS source catalog, the flux densities have been quoted from the effective wavelengths and an input energy distribution which is constant in the flux per logarithmic frequency interval (essentially the flux per octave); i.e., the flux density with frequency ν goes as $f_\nu \propto \nu$ while the flux density with wavelength λ goes as $f_\lambda \propto \lambda^{-1}$. If the input energy distribution is not constant in flux per octave, a correction called colour correction must be applied to the quoted flux density. This correction depends on the shape of intrinsic energy distribution and on the details of the wavelength response of the system (IRAS Explanatory Supplement 1985).

The flux F measured by a detector is given by

$$\begin{aligned}
 F &= f_{\nu_0} [actual] \int (f_{\nu}/f_{\nu_0}) [actual] R_{\nu} d\nu \\
 &= f_{\nu_0} [quoted] \int (f_{\nu}/f_{\nu_0}) [quoted] R_{\nu} d\nu \quad . \quad (84) \\
 &= \frac{f_{\nu_0} [quoted]}{K} \int (f_{\nu}/f_{\nu_0}) [actual] R_{\nu} d\nu
 \end{aligned}$$

In these equations, ν_0 is the effective frequency of 25, 12, 5, and 3×10^{12} Hz corresponding to the effective wavelengths of 12, 25, 60 and 100 μm , f_{ν} is either the actual or quoted flux density of the source, (f_{ν}/f_{ν_0}) is the flux density normalized to the effective frequency of the band and R_{ν} is the relative system response listed in the Table II.C.5 in the IRAS Explanatory Supplement (1985). The above equations show that the true flux density at ν_0 is given by

$$f_{\nu_0} [actual] = f_{\nu_0} [quoted] / K , \quad (85)$$

with the correction factor K :

$$K = \frac{\int (f_{\nu}/f_{\nu_0}) [actual] R_{\nu} d\nu}{\int (f_{\nu}/f_{\nu_0}) [quoted] R_{\nu} d\nu} , \quad (86)$$

and they are listed in Table 4.4 (IRAS Explanatory Supplement 1985).

Table 4.4 shows that the correction factor K is a function of temperature and wavelength. In order to get the colour temperature, the least-square fit to the four photometric band fluxes has been performed by using the Planck function (Volk 1986).

The quantity to be minimized is

TABLE 4.4 Colour Correction Factors K

T (K)	K (12 μ m)	K (25 μ m)	K (60 μ m)	K (100 μ m)
10000	1.45	1.41	1.32	1.09
5000	1.43	1.40	1.32	1.09
4000	1.42	1.40	1.31	1.09
3000	1.41	1.39	1.31	1.09
2000	1.38	1.38	1.31	1.09
1000	1.27	1.34	1.29	1.09
800	1.22	1.32	1.28	1.08
600	1.15	1.29	1.27	1.08
500	1.09	1.26	1.26	1.08
400	1.01	1.22	1.24	1.08
300	0.92	1.15	1.21	1.08
200	0.91	1.15	1.21	1.07
280	0.90	1.14	1.20	1.07
270	0.89	1.13	1.20	1.07
260	0.88	1.12	1.19	1.07
250	0.87	1.11	1.19	1.07
240	0.86	1.09	1.18	1.07
230	0.85	1.08	1.18	1.07
220	0.85	1.07	1.17	1.07
210	0.84	1.06	1.16	1.07
200	0.83	1.04	1.16	1.06
190	0.83	1.02	1.15	1.06
180	0.83	1.01	1.14	1.06
170	0.83	0.99	1.13	1.06
160	0.84	0.97	1.12	1.06

$$\chi = \sum_{i=1}^4 [\lg(\lambda_i F_{\lambda_i}) - \lg(\lambda_i B_{\lambda_i}(T_c))]^2 , \quad (87)$$

where $B_{\lambda}(T)$ is the Planck function:

$$B_{\lambda}(T_c) = A\lambda^{-5} [e^{hc/\lambda kT_c} - 1]^{-1} . \quad (88)$$

The parameters to be found are A and colour temperature T_c . Taking the partial derivatives of χ^2 with respect to A and T_c , and setting them equal to zero allows you to find A and T_c . Once T_c is found, the colour correction factors K can be found by using the linear interpolation according to Table 4.4. Table 4.5 is the T_c and K at $\lambda = 12, 25, 60, 100 \mu\text{m}$ for the three selected sources. The calibration factors for Low Resolution Spectrum are adopted from Volk and Cohen (1989).

TABLE 4.5 The Colour Temperature and The Correction Factors for Sample Stars

Star Name	T_c (K)	$K(12\mu\text{m})$	$K(25\mu\text{m})$	$K(60\mu\text{m})$	$K(100\mu\text{m})$
AFGL3068	326	0.943	1.168	1.218	1.075
o Ceti	752	1.203	1.313	1.278	1.080
OH25.6+0.6	257	0.877	1.117	1.190	1.070

4.3.3 Model Results for AFGL3068

The first observation of star AFGL3068 was made by AFCRL sky survey (Low et al. 1976). The near- and middle infrared spectrum was first observed by Lebofsky and Rieke (1977) using the 1.5 m telescope at The University of Arizona's Catalina Station and confirmed AFGL3068 to be an extremely evolved carbon-star for it has no evidence of

the SiC feature which is prominent in most known carbon stars. Volk and Kwok (1992) have used a radiative transfer model with two dust materials (graphite + SiC) to get a good fit to the LRS spectrum and IRAS data. Here we use graphite with the radius $a = 0.05 \mu\text{m}$ as the dust material and the distance $D = 1 \text{ kpc}$ in the model calculation. The other parameters used are listed in Table 4.6. Figures 4.5(a-b) show the spectrum fitting for AFGL3068 along with the spectra at different radii. It shows that the model result successfully approximates the observations from $5.0 \mu\text{m}$ to $23 \mu\text{m}$ including M band, LRS spectra and $12 \mu\text{m}$ IRAS flux, but does not fit the near infrared observations.

TABLE 4.6 Model and Derived Parameters

Star Name	M_* (M_\odot)	T_{eff} (K)	L_* (L_\odot)	\dot{M} (M_\odot/yr)	Φ_0	τ_{10}	u (km/s)
AFGL3068	1.0	2000	9000	1.0×10^{-4}	.0038	1.8	10.3
o Ceti	2.0	3000	20000	3.5×10^{-6}	.0035	0.63	15.2
OH25.6+0.6	2.0	2600	30000	2.4×10^{-4}	.0024	27.8	13.9

4.3.4 Model Results for o Ceti

Ever since Fabricius (1605) discovered brightness variations of o Ceti (IRAS02168-0312), much attention has been devoted to this star. With an average maximum brightness $V_{\text{max}} = 3.5$, a typical amplitude $\Delta V = 6.5$, an average period $P = 331.9$ days and a spectral type varying approximately between M5IIIe and M9IIIe (Quirrenbach et al. 1992), this star has the $9.7 \mu\text{m}$ silicate emission feature. The latest near-infrared JHKLM photometry was obtained by Fouque et al. (1992) using the ESO 1 m telescope equipped with its

standard infrared photometer. Since the LRS of α Ceti (IRAS 02168-0312) has the silicate emission feature, silicate with the radius $a = 0.05 \mu\text{m}$ is used as the dust particle in the model calculations. The distance inferred from the model calculation is 330 pc. The parameters used here are listed in Table 4.6. Figures 4.6(a-b) show the spectrum fitting for α Ceti along with the spectra at different radii. The plots show us that the model has successfully fitted the data from the observations from $7.9 \mu\text{m}$ to $60 \mu\text{m}$. But the flux on near infrared is lower than the observations. This may be because an M6III star emission is not a blackbody radiation which is used in the model calculations and that also the gas component should have some contribution in the near infrared continuum.

4.3.5 Model Results for OH25.6+0.6

The first spectrophotometry observation for star OH25.6+0.6 from $2 \mu\text{m}$ to $14 \mu\text{m}$ was made during the AFCRL Infrared Sky Survey (Walker & Price 1975), in which is identified the characteristic $9.7 \mu\text{m}$ silicate absorption feature presumably for an M type star (Merrill & Stein 1976). The latest near infrared photometry observations for JHKL' bands were made by Xiong, Chen and Gao (1994) by using 1.26 m infrared telescope in Xing Long station, Beijing, China. Silicate dust with the radius $a = 0.05 \mu\text{m}$ is used as the dust material and the distance from the star is 1.6 kpc in the model calculation and the other parameters used in the model calculation are listed in Table 4.6. Figures 4.7(a-b) show the spectrum fitting for OH25.6+0.6 and with the spectra at different radii. The fitting is good around the $10 \mu\text{m}$ absorption feature. But the absorption feature around $18 \mu\text{m}$ is not so strong as the observation indicates. The weakness of the $18 \mu\text{m}$ feature in

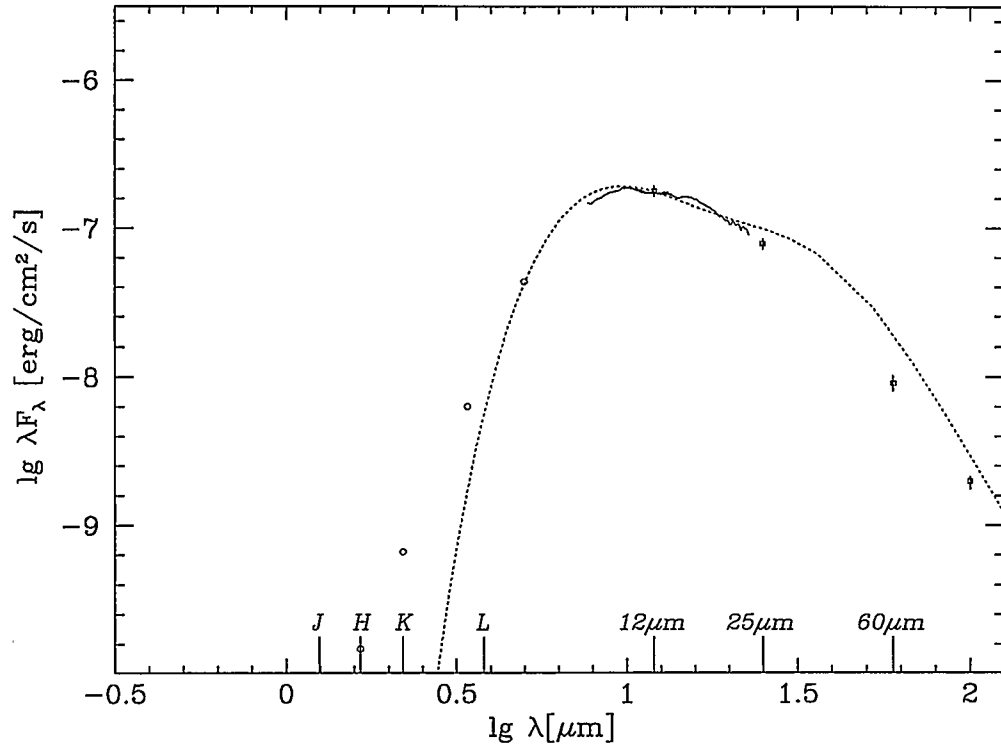


FIGURE 4.5a The spectrum fitting for AFGL3068 with the parameters listed in Table 4.6. The dotted line is from model calculations and the solid lines are from IRAS LRS spectra; the open squares are the IRAS fluxes and the open circles are from near infrared observations; the small straight lines are the error bars from the observations.

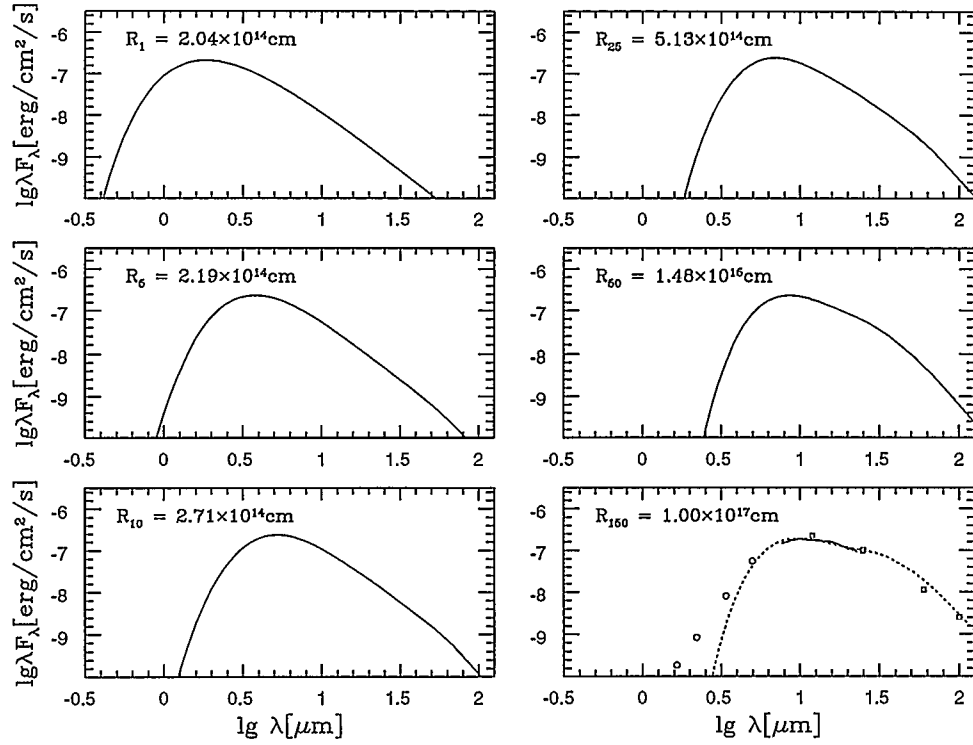


FIGURE 4.5b The spectral distributions at different radii for AFGL3068 with the spectrum fitting at the outer radius.

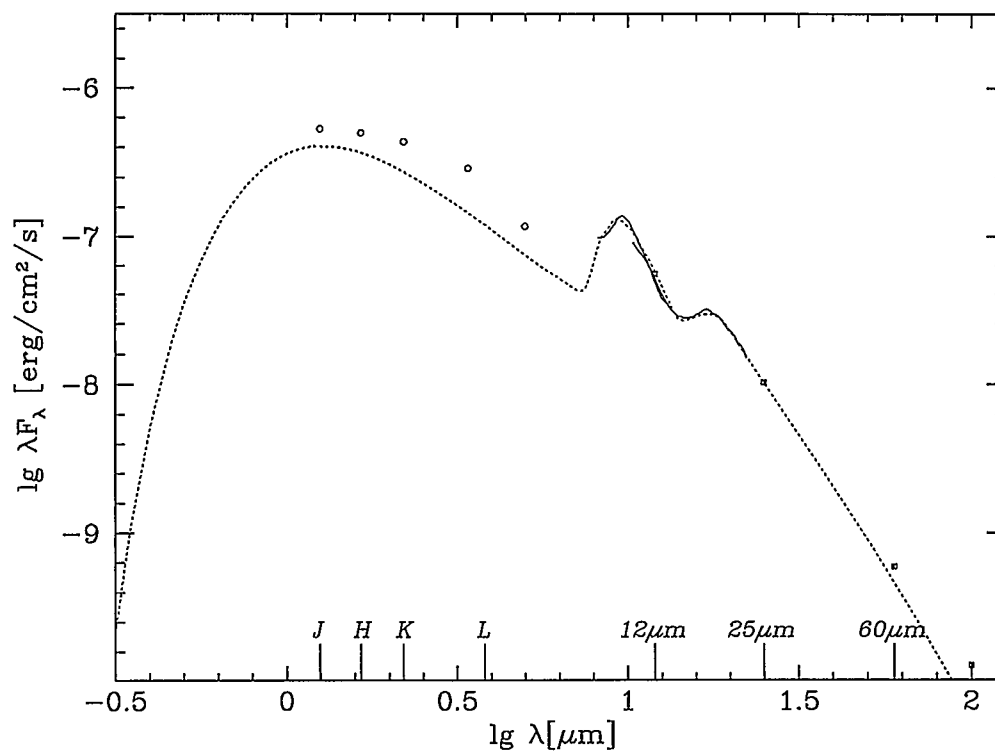


FIGURE 4.6a The spectrum fitting for o Ceti with the parameters listed in Table 4.6.

The meanings of the symbols are the same as in Figure 4.5a

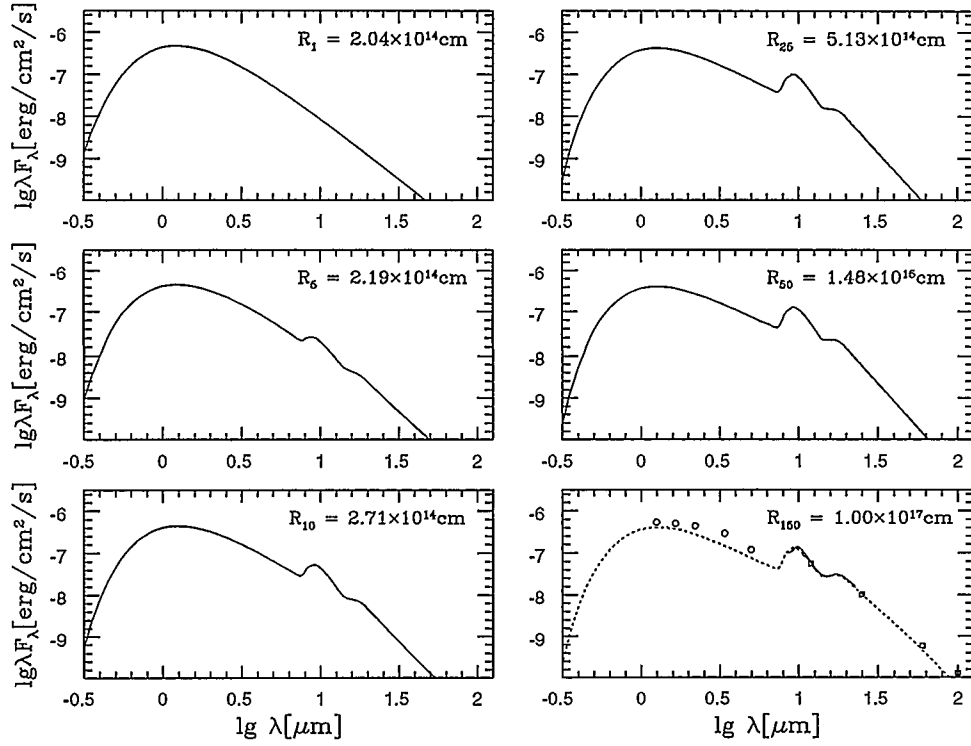


FIGURE 4.6b The spectral distributions at different radii for o Ceti with the spectrum fitting at the outer radius.

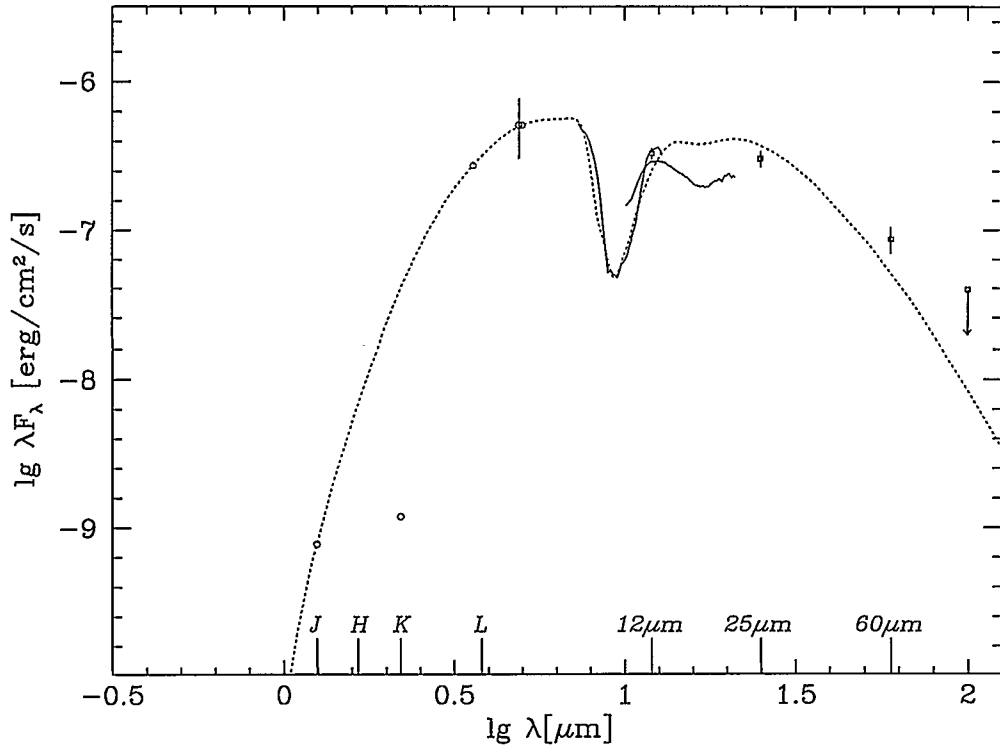


FIGURE 4.7a The spectrum fitting for OH25.6+0.6 with the parameters listed in Table 4.6. The meanings of the symbols are the same as in Figure 4.5a; the arrow at 100 μm means that the quality of the observation is bad and the upper limit is selected; the fluxes at 4.9 μm and 5.0 μm are come from their average value, the error bar at 5.0 μm gives the difference between the fluxes at 4.9 μm and 5.0 μm and the average flux.

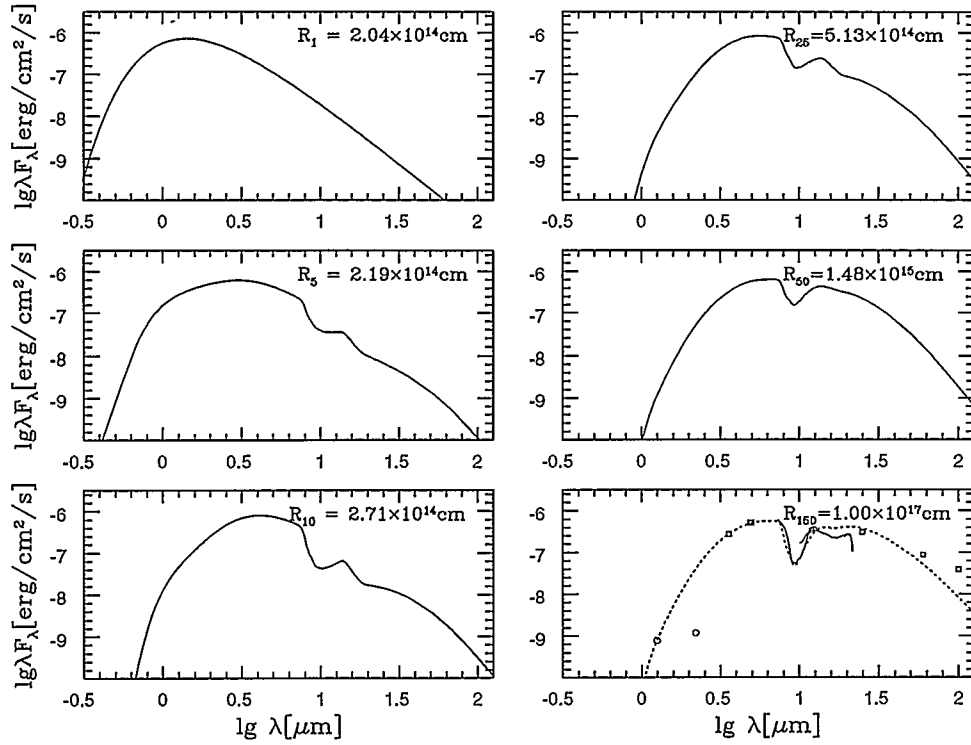


FIGURE 4.7b The spectral distributions at different radii for OH25.6+0.6 with the spectrum fitting at the outer radius.

the model can be understood since the 18 μm feature is in transition from emission to absorption when the optical depth at 10 μm is about 3-40 (Volk & Kwok 1988). It requires a larger amount of cool dust for the 18 μm feature to go into self-absorption. It can be seen from IRAS fluxes that the observations are much flatter than the model calculations at long wavelengths. Another possibility could be that the cool interstellar silicate dust materials contribute to the 18 μm absorption feature while the model does not take this into consideration. The model cannot fit the observational flux for K-band. The reason is not very clear, but the fact that the CO molecule absorption (for $\dot{M} = 2.4 \times 10^{-4} M_{\odot}/\text{yr}$) around this wavelength (2 μm) should be one factor to be blamed.

Figure 4.8 shows the density and velocity profiles for these three sample stars. For star AFGL 3068, the density profile is not much different from the inverse square power law ($\rho \propto r^{-2}$) beyond 25 stellar radii, but for stars o Ceti and OH25.6+0.6, the density profiles are different from the inverse square power law for the velocities increase with the radius out to 125 stellar radii.

From the fittings of these three stars, the near infrared continuum fluxes from the models for stars AFGL 3068 and o Ceti are lower than those from observations. This is perhaps because in our model only one kind of dust particle is considered on the radiation transfer, the gas and other kinds of dust particles should also have some contributions to the near infrared continuum.

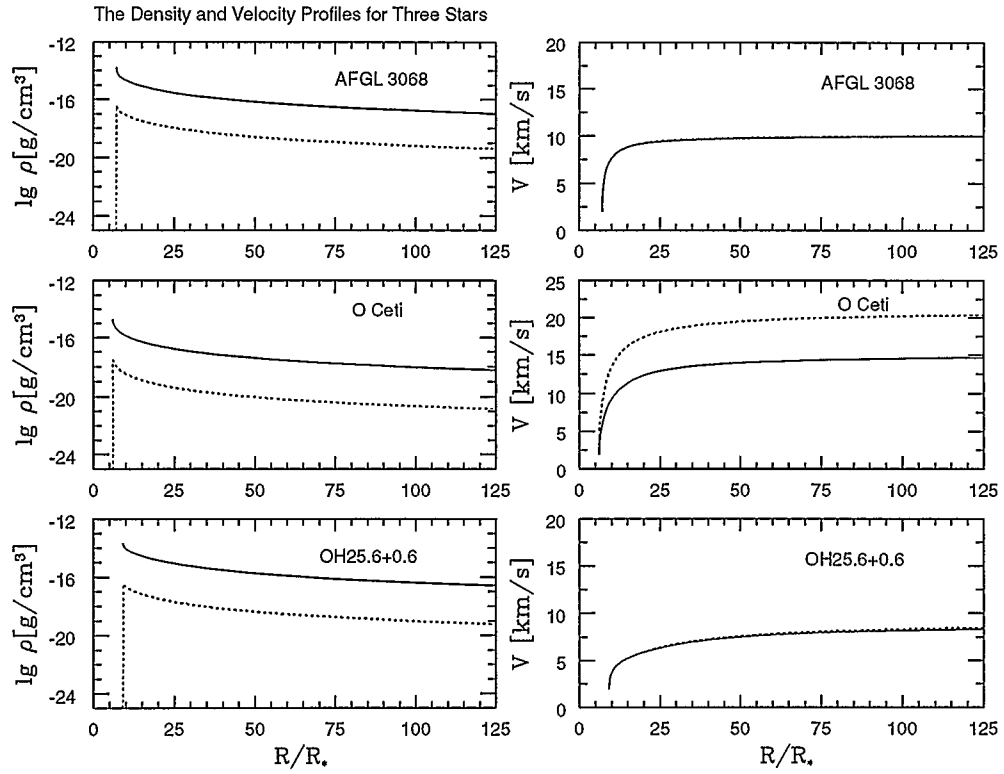


FIGURE 4.8 The density and velocity profiles for the three sample stars. The dotted lines are for the dust particles and the solid lines are for the gas materials.

Chapter 5 Summary and Conclusions

Results from Infrared Astronomical Satellite (IRAS) have shown that many evolved stars are surrounded and obscured by dust ejected in the form of stellar wind. It has been generally accepted that these winds are driven by radiation pressure on dust, however, no self-consistent theory on the hydrodynamics of such winds has yet been developed. Since the star is shielded from the view of dust in the outer parts by dust close to the star, the hydrodynamics equations have to be solved simultaneously with the equation of radiation transfer. In this thesis, we have developed the one -- dimensional numerical code for the hydrodynamics coupled with the fully radiative transfer solutions, and applied it to the envelopes of evolved stars -- AGB stars. Here is the brief summary.

The model for the stellar wind of an AGB star is based on the idea that the radiation pressure from the central star drives the dust outward, in the mean time, the interaction between the dust and the gas pulls the gas materials outwards. The momentum gained from the radiations is fully transferred to the momentum of material movement. In the model, we treat the stellar wind as a two component fluid since the dust moves out faster than does the gas, the detailed frequency dependent radiative transfer solution is pursued along with the fully hydrodynamic solutions. The details about the model and the numerical method are given in chapter 2.

We use this model to investigate the effects of some free parameters, such as the effects of dust grain size, the effects of mass loss rate and the lowest mass loss rate which can be driven by the radiation pressure and compared it to the results of Kwok (1975) and

Netzur & Elitzer (1993), and the effects of dust to gas ratio as demonstrated in chapter 3. The conclusions drawn here are that the spectral distributions and the terminal outflow velocities of AGB stars are affected greatly by the mass loss rate and dust to gas ratio. We have also found that the different dust size will result in different terminal velocity of outflow materials. We also investigate the rangers of dust condensation temperature and dust optical properties in details in chapter 3 as well.

The second area of work described in this thesis is modelling the terminal velocities of the stellar outflows. The goal here is to obtain better information about the stellar wind and the spectrum evolutions on AGB stars. To achieve this goal the empirical or semi-empirical formulae about the luminosities, effective temperatures and mass loss rates have been adopted and the observation data have been used, which are described in details in sections 4.1 and 4.2. The adopted formulae and the model calculations resulted in a reasonable agreement with the observations.

The third area of work done on this thesis is to model the infrared spectra of three AGB stars by fitting the model spectrum distribution to the IRAS data. The models are very successfully fitting the LRS spectra for both carbon-rich star, AFGL3068, and for the oxygen-rich star, o Ceti, which has emission feature at 10 μm . The model for the oxygen rich star, OH25.6+0.6, which has 10 μm absorption feature, successfully simulates the 10 μm feature, but provided a weaker silicate dust absorption feature around 18 μm than the observations.

One problem is that on the fitting of star AFGL 3068, we obtain too high fluxes on the long wavelengths compared to the IRAS fluxes at 25, 60, and 100 μm . Perhaps the

graphite opacity at long wavelength should be modified. The other problem is that the models can not fit the near infrared observations well. This maybe due to the emission of gas materials, which are not considered in the model.

The models presented in this thesis are qualitatively successful. In order to produce better quantitative results and provide the evolution of the stellar wind the time-dependent hydrodynamic model coupled with detailed radiative transfer solution should be used instead of steady--state calculations. More work needs to be done, such as to sort out the various parameters which are present in the models, the interstellar dust extinction effect and the emission of the gas material on the infrared continuum should be included on the model to produce the best possible match to the IRAS data. The other area we should improve is that we should use the numerical solutions from the stellar atmosphere radiative transfer models instead of blackbody radiation assumption as the stellar emission. This is very important for the low mass loss rate.

Bibliography

- Adams, F. C. & Shu, F. H., 1985, APJ, 296, 655.
- Adams, F. C. & Shu, F. H., 1986, APJ, 308, 836.
- Appenzeller, L. & Tschamnuter, W., 1974, A&A, 30, 423.
- Arquilla, R., Leahy, D. A. & Kwok, S., 1986, MNRAS, 220, 125.
- Beck, H. K. B. et al., 1992, A&A, 265, 626.
- Blöcker, T., 1993, PH. D. Thesis, University Kiel.
- Blöcker, T., 1995a, A&A, 297, 727.
- Blöcker, T., 1995b, A&A, 299, 755.
- Bodenheimer, P., 1972, Rep. Prog. Phys., 32, 1.
- Bohren, G. F. & Huffman, D. R., 1983, in Absorption and Scattering of Light By Small Particles, A Wiley-Interscience Publication, John Wiley & Sons, 83.
- Boothroyd, A. I. & Sackmann, I. J., 1988a, APJ, 328, 641.
- 1988c, APJ, 328, 671.
- Bowen, G. H., 1988, APJ, 329, 299.
- Bower, P. F. & Johnston, K. J., 1990, APJ, 354, 676.
- Bryan, G. L., Volk, K. & Kwok, S., 1990, APJ, 365, 301.
- Chan, S. J. & Kwok, S., 1990, A&A, 237, 354.
- Chapman, J. M. & Cohen, R. J., 1986, MNRAS, 220, 513.
- Cohen, J. G. et al., 1981, APJ, 249, 481.
- Cohen, M. & Tielens, A. G. G. M. et al., 1989, APJ, Lett. 344, L13.

- Draine, B. T. & Lee, H. M., 1984, APJ, 285, 89.
- Elitzur, M. et al., 1976, APJ, 205, 384.
- Fabircius, D., 1605, Kurtzer and Gründlicher Bericht, Hamburg.
- Fouque, P. et al., 1992, A&A Supplement Series 93, 151.
- Friedmann, C., 1969, Physica, 41, 139.
- Gail, H. P. & Sedlmayr, E., 1986, A&A, 166, 225.
- Gail, H. P. & Sedlmayr, E., 1987, in Physical Processes in Interstellar Clouds, eds. G. Morfill and M. Scholer, (Reidel, Dordrecht), 275.
- Gauge, A., Gail, H. P. & Sedlmayr, E., 1990, A&A, 235, 345.
- Gehrz, R. D., 1989, in IAU Symposium No. 135; Interstellar Dust, eds. Allamandola, L. T. & Tielens, A. G. G. M., 445.
- Gilman, R. C., 1969, APJ, 155, L185.
- Gilman, R. C., 1972, APJ, 178, 423.
- Gilra, D. P., 1972, The Scientific Results from the Orbiting Astronomical Observatory (OAO-2), ed. A. D. Code (NASA SP-301)
- Goldreich, P. & Scoville, N., 1976, APJ, 205, 144.
- Habing, H. J., Tignon, J. & Tielens, A. G. G. M., 1994, A&A, 286, 523.
- Hackwell, J. A., 1972, A&A, 21, 239.
- Henry, L. G. et al., 1964, APJ, 139, 306.
- Hummer, D. H. & Rybick, G. B., 1971, MNRAS, 152, 1.
- Iben, I., 1981, APJ, 246, 278.
- Iben, I. Jr. & Renzini, A., 1983, ARA&A, 21, 271.

- IRAS Catalogs and Atlases, Explanatory Supplement. 1985, eds. C.A. Beichman, G. Neugebauer, H. J. Habing, P. E. Clegg, and T. J. Chester (Washington D. C.: US Government Printing Office).
- IRAS Catalogs and Atlases, Catalog of Low Resolution Spectra. 1986, A&A Suppl., 65, (LRSC).
- Jura, M., 1986, APJ, 303, 327.
- Jura, M. et al., 1988, A&A, 201, 80.
- Jura, M., 1990, in From Miras to Planetary Nebulae: Which Path for Stellar Evolution? eds. Mennessier, M. O. & Omont, O., (Yvette Cedex: Editions Frontiers), 67.
- Knapp, G. R., 1986, APJ, 311, 731.
- Knapp, G. R. et al., 1982, APJ, 252, 616.
- Knapp, G. R. et al., 1989, APJ, 336, 822.
- Knapp, G. R. & Morris, M., 1985, APJ, 292, 640.
- Kwok, S., 1975, APJ, 198, 583.
- Kwok, S., 1976, 1976, J. Roy. Astron. Soc. Canada, 70, 49.
- Kwok, S., 1983, in Planetary Nebulae, IAU Symp., 103, ed. D. R. Flower, Reidel, Dordrecht, 293.
- Kwok, S., 1985, APJ, 290, 568.
- Kwok, S., 1987, Physics Reports, 156(3), 111.
- Kwok, S., 1990, MNRAS, 224, 179.
- Kwok, S., 1993, A.R.A&A., 31, 63.
- Kwok, S. & Chan, S. J., 1993, APJ, 106, 2140.

- Lambert, D. L. et al., 1986, APJ Suppl., 62, 373.
- Larson, R. B., 1969, MNRAS, 145, 271.
- Larson, R. B., 1972, MNRAS, 157, 121.
- Leahy, D. A., Kwok, S. & Arquilla, R. A., 1987, APJ, 320, 285.
- Lebofsky, M. J. & Rieke, G. H., 1977, APJ, 82, 646.
- Le Borgne, J. F. & Mauron, N., 1989, A&A, 210, 198.
- Leung, C. M., 1975, APJ, 199, 340.
- Likkel, L. & Forveille, T. et al., 1988, A&A, 198, L1.
- Likkel, L. & Omont, A. et al., 1987, A&A, 183, L13.
- Loar, A. & Draine, B. T., 1993, APJ, 402, 441.
- Low, F. J. & Kurtz, R. F. et al., 1976, APJ, Lett 206, L153.
- Merril, K. M., 1977, in IAU Colloquium 42; The Interaction of Variable Stars With Their Environment, ed. R. Kippenhahn, J. Rahe and W. Strohmeier, 446.
- Merri, K. M. & Stein, W. A., 1976, Publications of the Astronomical Society of the Pacific, 88, 874.
- Mezger, P. G., 1983, in Birth and Infancy of Stars, ed. Robert Lucas, Alain Omont and Raymond Stora, 31.
- NASA Catalog of Infrared Observations, 1993, eds. D. Y. Gezari, M. Schmitz, P. S. Pitts & J. M. Mead.
- Netzer, N. & Elitzur, M., 1993, APJ, 410, 701.
- Neugebauer, G. & Leighton, R. B., 1969, Two-Micro Sky Survey, NASA SP-3047.
- Olofsson, H., Eriksson, K., & Gustafsson, B., 1987, A&A, 183, L13.

- 1988, A&A, 196, L1.
- Paczynski, B., 1971, Acta Astr., 31, 417.
- Papular, E., & Pegourie, B., 1983, A&A, 128, 335.
- Pritchett, C.J., Richer, H. B., et al., 1987 APJ, 323, 79.
- Pottach, S. R., 1984, Planetary Nebulae, (Dordrecht Reidel), 215.
- Quirrenbach, A. et al., 1992, A&A, 259, L19.
- Richer, H. B. & Crabtree, D. R. 1985, APJ, 289, L13.
- Rieu, N. Q. et al., 1987, A&A, 180, 117.
- Rowan-Robinson, M., 1980, APJs, 44, 403.
- Rowan-Robinson, M. & Harris, S., 1982, MNRAS, 200, 197.
- Rowan-Robinson, M. & Harris, S., 1983, MNRAS, 202, 767.
- Salpeter, E. E., 1974, APJ, 193, 585.
- Salpeter, E. E., 1977, ARA&A, 15,267.
- Schwarzschild, M. & Harm, R., 1965, APJ, 142, 855.
- Schönberner, D. et al., 1994, Evolution From the AGB Through the Planetary Nebula Stage in Asymmetrical Planetary Nebulae, Annals. of Israel Physical Society, eds. Harpaz, H. & Soher, N., Vol 11, 81.
- Schutte, W. A. & Tielens, A. G. G. M., 1989, APJ, 343, 369.
- Snow, T. P., Buss, R. H. et al., 1987, APJ, 321, 921.
- Sopka, R. J., Hilderbmel, R. et al., 1985, APJ, 294, 242.
- Steffen, M. & Szczerba, R. et al., 1995, Self-consistent Models and Synthetic Spectra of Circumstellar Dust Shells, in Liege International Astrophysical Colloquium, 165

- Tielens, A. G. G. M., 1983, APJ, 271, 702.
- Tielens, A. G. G. M., 1989, in From Miras to Planetary Nebulae: Which Path for Stellar Evolution? eds. M. N. Mennessier & A. Omont, (Editions Frontiers), 186.
- Vassiliadis, E. & Wood, P. R., 1993, APJ, 413, 641.
- Volk, K., 1986, PH.D. Thesis, The Dept. of Phys., The Univ. of Calgary.
- Volk, K. & Kwok, S., 1987, APJ, 315, 654.
- Volk, K. & Kwok, S., 1988, APJ, 331, 435.
- Volk, K. & Kwok, S., 1992, APJ, 391, 285.
- Wainscoat, R. J., Cohen, M., & Volk, K. et al. 1992, APJ Suppl. Series, 83, 111.
- Walker, P. G. & Price, S. D., 1975, Nature, 253, 101.
- Wannier, P. G. & Sahai, R., 1986, APJ, 311, 335.
- Weidemann, V., 1990, A. R. A&A, 28, 103.
- Weidemann, V., 1993, in Mass Loss on the AGB and Beyond, ed. H. E. Schwarz, 55.
- Weidemann, V. & Koester, D., 1983, A&A, 121, 77.
- Weigert, A., 1966, Z. APJ, 64, 395.
- Weymann, R. J., 1962a, *ibid.*, 136, 476.
- Wood, P. R., Bessell, M. S. & Fox, M. W., 1983, APJ, 272, 99.
- Wood, P. R. & Cahn, J. H., 1977, APJ, 211, 499.
- Wood, P. R. & Zarro, D. M., 1981, APJ, 397, 552.
- Woolf, N. J. & Ney, E. P., 1969, APJ lett. 155, L181
- Xiong, G. Z., Chen, P. S. & Gao, H., 1994, A&A Suppl. Series, 108, 661.
- Yorke, H. W., 1979, A&A, 80, 308.

Yorke, H. W., 1980, A&A, 85, 215.

Yorke, H. W., 1980, A&A, 86, 286.

Yorke, H. W. & Krügel, E., 1977, A&A, 54, 183.

Zhang, C. Y. & Kwok, S., 1993, APJ Suppl. Series, 88, 137

Zuckerman, B. et al., 1986, APJ, 304, 401.

Zuckerman, B. & Dyck, H. M., 1986a, APJ, 304, 394.

----- 1986b, APJ, 311, 345.

----- 1989, A&A, 209, 119.